UNIVERSITÀ
DEGLI STUDI
DI PADOVA

Sede Amministrativa: Università degli Studi di Padova

Dipartimento di Scienze Chimiche

SCUOLA DI DOTTORATO DI RICERCA IN SCIENZA ED INGEGNERIA DEI MATERIALI

CICLO XXVII

OPTO-THERMAL PROPERTIES OF PLASMONIC METAL NANOSTRUCTURES IN SOLUTION AND IN POLYMER MATRIX FOR OPTICAL LIMITING PROTECTION AGAINST CW LASER

Direttore della Scuola : Ch.mo Prof. Gaetano Granozzi

Supervisore : Ch.mo Prof. Renato Bozio

Dottoranda : Frare Maria Chiara

CONTENTS

Abstract (English)

The development of nanotechnology has provided a variety of noble metal nanostructures with unique optical properties that are useful for different application fields. Metal nanoparticles present strongly enhanced optical properties associated with localized surface plasmon resonance (LSPR): here, the effect on the optical properties of metal nanostructures is investigated by different techniques. The large AuNPs absorption cross section coupled with fast nonradiative decay rate and low radiative decay efficiency make them perfect converter of light into heat: the high temperatures reached can be used for photothermal terapy, light conversion in thermal and photovoltaic devices, but our interest has been focused on optical limiting application against cw laser.

The study of the thermal conversion of incoming light could be useful for the protection of the human eye from accidental or intentional damage. A good protection device should be a "smart material" able to activate the protection at high energy with a large dynamic range and in a wide wavelength interval. The last property is especially required in the case of military use, for protection against laser pointing devices or blinding weapons of unpredictable emission wavelength. In this case, passive filters, commonly used for specific wavelengths, are useless because of their selectivity and lack of tuning properties. The irradiation of an optical limiting material with a focused cw laser beam induces energy absorption rapidly converted into a local heating and a temperature gradient corresponding to a refractivity index variation across the sample. In this way, even a flat sample acts as a focusing or defocusing lens and spreads the laser beam.

We have studied different aspects of the phenomenon, as described below, to achieve the application in a solid state device with a broadband range of activity and a fast response time.

In the first experimental part of this thesis different nanostructures have been synthesized, starting from gold nanoparticles, nanoshells and nanorods with different aspect ratio, in order to obtain plasmonic resonances in a wide range of the visible spectrum. Nanostructures has been then manipulated for the functionalization with a thiolated-fulleropyrrolidine (FULP-SH) to combine the thermal relaxation process with a faster one. A useful material for protection

devices should preferably be in the solid state, so a thorough study has been centered on polycarbonate (PC) as matrix because of its good optical qualities. Film production and nanoparticles embedding require a specific study of the functionalization and transfer of nanostructures synthesized in aqueous solvent.

We characterized the morphology and their linear optical properties with conventional techniques: transmission electron microscopy (TEM) gives information about the dimension of nanostructures to implement the synthesis, UV-Vis spectroscopy correlates structures with extinction properties and surface enhanced Raman spectroscopy (SERS) of the nanosystems defines the correct functionalization with organic molecules.

In the second part of the project we studied and tried to improve the nonlinear optical response of these promising systems in order to obtain different characteristics.

Using z-scan technique we define the nature of the defocusing mechanism, confirming the self-defocusing behavior and giving nonlinear efficiency parameters to compare different systems. Optical power limiting measurements give direct information on the protection ability of these systems. Thanks to the easy functionalization of nanostructures we figured out promising properties for a solid state protection device.

First we have studied the optical limiting properties of gold nanoparticle solutions identifying a thermal response as the main mechanism. We have then compared these results with those obtained by coupling gold nanoparticles with a thiolated-fulleropyrrolidine. In this way we wanted to combine the thermal process with a faster one, to permit a stronger reduction of transmittance and a better limiting efficiency. Such a strategy has been proved to be effective for improving OL through a quite different mechanism that is activated in a much shorter time. Optical limiting measurements have been conducted on gold nanoparticles embedded in polycarbonate with good results that have been compared to the colloidal solutions. The study of a different matrix for optical limiting studies has been attempt: silk fibroin. This matrix has been selected because of the easier nanoparticles embedding. Furthermore it can be applied for instance in controlled release of drugs, thanks to the biocompatibility and gradual solubility of silk matrix. Preliminary studies discourage the use of this system for optical limiting but different application could be considered. The fibroin-nanoparticles solution can be easily transform to obtain a porous structure: the idea is to employ this matrix as a sensor for liquid

samples with SERS characterization, taking advantage of the high porosity and the presence of plasmonic structures.

In the last part we tried to compare thermal properties revealed by our systems through cw laser excitation to nonlinear optical properties classically expressed by pulsed laser excitation. Optical limiting related to photoacoustic measurements allow us to discriminate the contribution of the absorption and to choose the best system with higher linear transmittance and lower threshold for nonlinear behavior

Abstract (Italiano)

Lo sviluppo delle nanotecnologie ha fornito una varietà di nanostrutture metalliche con proprietà ottiche uniche utili per diverse applicazioni. Le nanoparticelle metalliche presentano una forte amplificazione delle proprietà ottiche associate al plasmone di risonanza superficiali (LSPR): in questo lavoro abbiamo studiato le proprietà ottiche di nanoparticelle d'oro (AuNPs) con diverse tecniche. La grande *cross section* di assorbimento delle AuNPs accoppiata con la rapido decadimento non radiativo e la scarsa efficienza di decadimento rendono efficace la conversione di luce in calore: le alte temperature raggiunte possono essere utilizzate per terapia fototermica, conversione luminosa in dispositivi fotovoltaici, ma il nostro interesse si è focalizzato sull'applicazione nella limitazione ottica contro laser in continuo (cw).

Lo studio della conversione termica della luce incidente può essere utilizzato per la realizzazione di dispositivi per la protezione dell'occhio contro danni accidentali o intenzionali. Un buon dispositivo di protezione dovrebbe essere un *materiale intelligente* in grado di attivarsi sopra una certa soglia di intensità, con un ampio intervallo di attività e a diverse lunghezze d'onda. Quest'ultima proprietà è di particolare interesse in ambito militare per la protezione contro dispositivi laser di puntamento o armi accecanti di lunghezze d'onda non note a priori. In questo caso sono i filtri passivi per specifiche lunghezze d'onda attualmente utilizzati risultano inefficaci data la loro alta selettività e scarsa versatilità.

L'irraggiamento di un limitatore ottico con un raggio laser cw focalizzato induce un assorbimento dell'energia che viene rapidamente convertito in un riscaldamento locale e la formazione di un gradiente di temperatura che corrisponde ad una variazione di indice di rifrazione attraverso il campione. In questo modo anche un campione piatto agisce come una lente focalizzante o defocalizzante e diffonde la luce.

Abbiamo studiato diversi aspetti del fenomeno, come descritto in seguito, per ottenere un dispositivo a stato solido con un ampio intervallo di attività e una risposta rapida.

Nella prima parte sperimentale di questa tesi sono state sintetizzate diverse nanostrutture, a partire da nanoparticelle d'oro, *nanoshells* e *nanorods* con *aspect ratio* differenti, al fine di ottenere risonanze plasmoniche in un ampio intervallo dello spettro visibile. Le nanostrutture

sono state in seguito funzionalizzate con molecole di fulleropirrolidina tiolata (FULP-SH) per combinare il processo di rilassamento termico con uno più rapido.

Un limitatore ottico per un dispositivo di protezione deve essere preferibilmente solido, e quindi lo studio delle proprietà ottiche è stato effettuato anche in matrice, in particolare in polycarbonato (PC), scelto per le sue ottime qualità ottiche. La produzione dei film e l'inglobamento delle nanoparticelle ha richiesto degli studi sulla funzionalizzazione e la stabilizzazione delle nanostrutture sintetizzate in solvente acquoso.

Abbiamo caratterizzato la morfologia e le proprietà ottiche lineari con tecniche convenzionali: microscopia a trasmissione elettronica (TEM), che fornisce informazioni sulle dimensioni e la forma delle nanostrutture al fine di implementarne la sintesi, spettroscopia UV-Visibile che correla le strutture con le proprietà di estinzione, e la spettroscopia Raman che ha verificato l'effettiva funzionalizzazione dei sistemi con le molecole organiche.

Nella seconda parte del progetto abbiamo studiato le risposte ottiche non lineari di questi promettenti sistemi per poterne modulare le proprietà.

Attraverso la tecnica Z-scan siamo stati in grado di definire la natura del meccanismo di defocalizzazione e di ottenere i parametri non lineari che ci hanno permesso di confrontare i nostri risultati con quelli attualmente presenti in letteratura. Misure di limitazione ottica hanno dato informazioni sull'efficacia di protezione dei nostri sistemi. Grazie alla semplicità di funzionalizzazione delle nanoparticelle abbiamo individuato delle nuove e promettenti proprietà per un dispositivo di protezione a stato solido.

In primo luogo abbiamo studiato le proprietà di limitazione ottica di nanoparticelle in soluzione per identificare la tipologia di funzionamento. In seguito i risultati sono stati confrontati con quelli ottenuti con nanoparticelle funzionalizzate con FULP-SH. In questo modo abbiamo tentato di associare al processo di rilassamento termico un meccanismo più rapido, in modo da ridurre maggiormente la trasmittanza e migliorare l'efficienza di limitazione. Abbiamo quindi verificato l'efficacia della strategia utilizzata evidenziando un miglioramento della limitazione ottica in un tempo inferiore.

Le misure di limitazione ottica eseguite su nanoparticelle in matrice di PC hanno dato ottimi risultati, paragonabili a quelli ottenuti in soluzione. Un primo di studio di matrici differenti si è concentrato sulla fibroina della seta, scelta per la semplicità di inglobamento delle

nanoparticelle. Inoltre questo sistema AuNPs-fibroina potrebbe trovare sbocco anche in diverse applicazioni: grazie alla biocompatibilità della matrice ed alla sua solubilità graduale in acqua potrebbe essere usato per il rilascio controllato di farmaci. Studi preliminari scoraggerebbero l'utilizzo di questo sistema nella limitazione ottica ma possono essere comunque considerate altre applicazioni. Le nanoparticelle in fibroina possono infatti essere facilmente trasformate in strutture porose: un'idea potrebbe essere quella di utilizzarle come sensori per campioni in soluzione con caratterizzazione Raman amplificata (SERS), combinando l'alta porosità e la presenza di strutture plasmoniche.

Nell'ultima parte abbiamo confrontato le proprietà termiche dei nostri sistemi attraverso studi di fotoacustica che ci hanno permesso di discriminare il contributo assorbitivo dall'estinzione totale e di scegliere il sistema migliore con alta trasmittanza lineare e basse soglie di attivazione nonlineari.

.

Chapter 1

1 INTRODUCTION

1.1 Nanotechnology

In the last years, we witnessed the massive advance of nanomaterials in material science. Since nanotechnology was introduced by Nobel laureate Richard P. Feynman in 1959 lecture "*There's Plenty of Room at the Bottom*"[1], many revolutionary developments have been made in manipulating matter at the nanoscale, i.e. at the level of molecules and atoms, giving birth to this new research field of objects of dimensions less than 100 nm. With these dimensions, the ratio between surface and inner atoms becomes significant and changes the original properties of the bulk system.

Among this variety of nanosystems, metal nanostructures have revealed interesting properties, dependent on their size and shape[2–10], the distance between them[11–13] and the environment[14–23]. The particular success of noble metal nanoparticles is due to the presence of the surface plasmon resonance[7,24] (SPR), a coherent oscillation of conduction electrons on the surface of the nanostructure. This phenomenon results in interesting absorption and scattering properties in the visible region and can be exploited for many applications[10,25,26]. The main characteristic is the great surface plasmon absorption, with a 10^5 larger extinction cross section than ordinary chromophores. To date, nanotechnologies apply to several fields as photovoltaic[27–33], catalysis[34–36], optical limiting[37–40], medicine[41–44] and sensing[45–47].

More tunable SPR properties can be obtained with rod-like structures, increasing their aspect ratio, and core-shell gold nanoparticles, varying the thickness of the shell; thus also the near infrared region (NIR) can be reached. Considering the high transparency of biological tissues

to these wavelength radiations, these systems can allow the application of SPR in biomedicine[48–58]. Moreover, nanostructures present fast and highly efficient energy conversion and dissipation, readily used for the heating of the local environment: the achievement of high temperatures contributes to the cell destruction by photothermal therapy and can be exploited in thermal and photovoltaic devices. Our interest has been focused in optical limiting application against cw laser.

1.2 Aim of the thesis

Among the applications of these versatile metal nanostructures we have been interested in the last one: optical limiting. In this work we tried to obtain a solid state device to protect the human eye against unpredictable cw laser radiation, with a broadband range of activity, that presents a fast response time. We study these different properties as described below.

Until now filters have been used for this scope, but active materials, able to be transparent at low input powers and become opaque at higher ones, represent a class of useful material. We have chosen gold nanostructures as active media, because of their tunable optical properties that allow us to select a desirable wavelength. Moreover, colloidal nanoparticles work typically by dissipating the absorbed energy through environment heating, with the generation of a temperature gradient corresponding to a refractivity index variation across the sample. In this way, even a flat sample acts as a focusing or defocusing lens and spreads the laser beam.

A part of the PhD has been dedicated to find out an efficient synthesis, stabilization and transfer route of metal nanostructures. Many studies have been conducted on different structures: in particular nonlinear properties, i.e. nonlinear absorption and refraction coefficients, have been determined with z-scan, optical limiting and thermal response. An in-depth analysis has been made on the possible origin of metal nanoparticles response to cw excitation through a comparison between different theories and experiments. The main interest has been the determination of the processes involved in the limiting action, with the attempt at improving the properties of nanoparticles through the functionalization with organic molecules. These studies of gold nanostructures in colloidal solution and embedded in a solid matrix required investigation of the stabilization, concentration and solvent transfer. An analysis of the

characteristics of the device has been conducted, in order to define the linear transmittance and the maximum permissible exposure (MPE) required to obtain a low output fluence and so prevent retina injuries.

1.3 Thesis overview

The thesis is divided in 3 main Chapters: the first one concerns a theoretical description of the properties and phenomena generated by plasmon nanostructures, the second is focused on their synthesis and optical and morphological characterization, and the third is the description of nonlinear measurements and final characteristics of the solid state devices.

In Chapter 2 a brief description of the theory of plasmon resonance in metal surfaces is introduced: Mie theory and its extension to spheroidal and core-shell nanoparticles is introduced. Nonlinear optics with some examples on metal nanostructures is described, as well as thermal refraction processes due to cw laser irradiation. Finally, an overview of optical limiting mechanisms of different structures irradiated with pulsed and cw laser is presented.

In Chapter 3 the syntheses of gold nanospheres, nanorods and gold silica core-shells have been described and a strategy to transfer them into different solvents and matrices have been developed. The morphological characterization of these nanostructures has been conducted thorough Dynamic Light Scattering and Transmission Electron Microscopy techniques. Linear measurements on both colloidal solution and polymer matrix have been performed through UV-Vis absorption spectroscopy, and nanoparticles functionalization has been verified with Raman Spectroscopy.

In Chapter 4 and Chapter 5 the nonlinear optical properties of gold nanostructures are described. Optical power limiting, Z-scan and temporal response techniques are used to characterize nonlinear absorption of colloidal solutions and films, together with photoacoustic measurements. The comparison of photoacoustic and optical limiting measurements allows us

to determine the thermal contribution to the limiting process. Preliminary theoretical results with two different simulations have been compared with experimental ones.

In Chapter 6 we have discussed the results presented before, comparing different nanostructures both in solution and in film. Moreover, we compared the final performance of our system with the requirements of an ideal eye protection device.

Finally, conclusions with a brief overview of the results will be given in Chapter 7.

Chapter 2

2 SURFACE PLASMONS IN METAL NANOSTRUCTURES

In this Chapter the physical origin of the surface plasmon absorption in metallic nanostructures and the nonlinear properties induced after interaction with a laser radiation will be described, focusing on the specific application in optical limiting.

The phenomenon of collective oscillation of the conduction electrons of a metal at the interface with a dielectric is called Surface Plasmon Resonance (SPR). It was first described by Gustav Mie in his paper on the scattering of light by small spherical particles using Maxwell's electromagnetic theory[59]. It occurs when an electromagnetic radiation of a well-defined wavelength interacts with the metallic system: the free electrons in the conduction band will oscillate with respect to the fixed positive ions (Figure 2.2: Surface plasmon on a metal nanoparticles in a) absence and b) presence of an external electromagnetic field.Figure 2.2). When the exciting field is resonant with the electron oscillation frequency, a strong electromagnetic field develops near the nanostructure surface. This field can be exploited to enhance some linear and nonlinear properties of molecules adsorbed or bound to the metallic surface.

.

To better understand this phenomenon, we have to introduce the dielectric function of a metal, which is related to the plasmon frequency that characterizes the electrons oscillation:

$$\varepsilon_D(\omega) = 1 - \frac{\omega_p^2}{\omega^2 + i\gamma\omega} \tag{2.1}$$

where γ is the characteristic collision rate responsible for damping of electron oscillations and ω_p is the plasma frequency of the free electron system defined as:

$$\omega_p = \sqrt{\frac{ne^2}{\varepsilon_0 m}} \tag{2.2}$$

where e is the elementary charge, ε_0 is the permittivity of free space and m is the electron mass. The excitation of the bulk plasmon polariton is not allowed as shown in Figure 2.1 because the dispersion curve of the incident light (black straight line) does not intersect the dispersion curve of the bulk plasmon polariton (black curve).

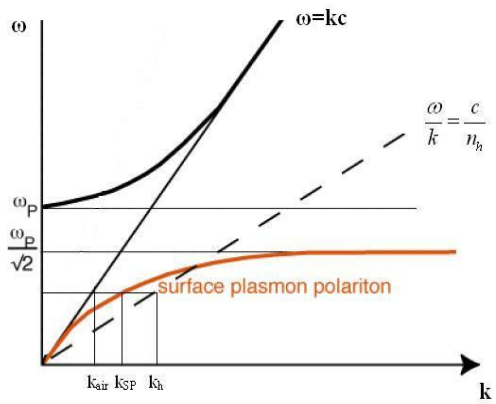

Figure 2.1: Dispersion relation curves of an electromagnetic mode of the incident radiation in vacuum (black line), for the bulk plasmon polariton (black curve) and for surface plasmon polaritons (red curve).

Only the introduction of boundary conditions, i.e. the presence of an interface, determines the matching between the dispersion relation of the plasma frequency and the electromagnetic radiation, generating the so called Propagating Surface Plasmon Polaritons.

2.1 Mie and Gans theories for spherical-spheroidal nanoparticles

Mie in 1908 developed a complete theory of the scattering and absorption of electromagnetic radiation by a sphere, in order to understand the colours of colloidal gold particles in solution[60]. The very small dimensions of nanoparticles (1-100 nm) do not require anymore the boundary conditions needed for the bulk system to match the plasmon frequency of the metal with the one of the radiation. For small isolated metal particles (20 nm size), an external field can

penetrate into the volume and shift the conduction electrons with respect to the ion lattice (Figure 2.2).

The coherently shifted electrons together with the restoring field represent an oscillator: if excited at resonance, the amplitude of the induced electromagnetic field can exceed the exciting fields by a factor on the order of 10.

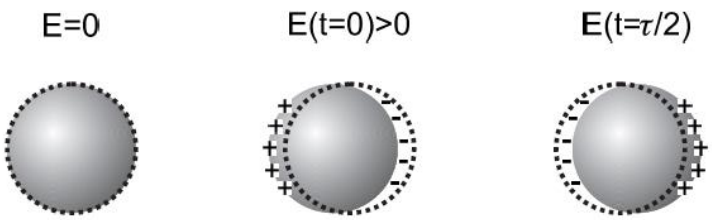

Figure 2.2: Surface plasmon on a metal nanoparticles in a) absence and b) presence of an external electromagnetic field.

The bright color shown by metallic nanoparticles such as gold and silver, is due to excitation of the collective oscillation mode by electromagnetic radiation in the visible range.

The solution of the electrodynamic calculation obtained solving exactly the Maxwell's equations with the use of appropriate boundary conditions, leads to a series of multipole oscillations of the extinction cross section[7] and to the following expression for the absorption cross section σ_{abs} as the difference between the extinction σ_{ext} and scattering σ_{sca} ones:

$$\sigma_{abs} = \sigma_{ext} - \sigma_{sca} \tag{2.3}$$

$$\sigma_{ext} = \frac{2\pi}{|k^2|}\sum_{L=1}^{\infty}(2L+1)Re(a_L + b_L) \tag{2.4}$$

$$\sigma_{sca} = \frac{2\pi}{|k^2|}\sum_{L=1}^{\infty}(2L+1)(|a_L|^2 + |b_L|^2) \tag{2.5}$$

$$a_L = \frac{m\psi_L(mx)\psi'_L - \psi'_L(mx)\psi_L}{m\psi_L(mx)\eta'_L - \psi'_L(mx)\eta_L} \tag{2.6}$$

$$b_L = \frac{\psi_L(mx)\psi'_L - m\psi'_L(mx)\psi_L}{\psi_L(mx)\eta'_L - m\psi'_L(mx)\eta_L} \tag{2.7}$$

where $m=n/n_m$ (n complex refractive index of the particles, n_m real refractive index of the medium), k is the wave vector (with r particle radius) and ψ_L and η_L are Ricatti-Bessel functions with L index of summation over spherical harmonics.

If the particle size is much smaller than the wavelength of the incident radiation ($2r \ll \lambda$) we can introduce the dipole approximation. The Mie theory reduces to the following expression:

$$\sigma_{ext}(\omega) = 9\frac{\omega}{c}\varepsilon_m^{3/2}V\frac{\varepsilon_2(\omega)}{[\varepsilon_1(\omega)+2\varepsilon_m]^2+\varepsilon_2(\omega)^2} \tag{2.8}$$

where V is the volume of the particle, ω is the angular frequency of exciting radiation, c is the speed of light and ε_m and $\varepsilon(\omega) = \varepsilon_1(\omega) + i\varepsilon_2(\omega)$ are, respectively, the dielectric function of the medium and of the bulk metal. The former is independent on frequency if the medium is not absorbing and the resonance condition is satisfied when $\varepsilon(\omega) = -2\varepsilon_m$.

In the dipole approximation, the Mie theory also predicts an increase of the electric field at the surface of the nanoparticle and we can describe the local electromagnetic field as the sum of the incident field E_0 and of the polarization induced by the surface plasmon excitation for spherical particles:

$$E_{loc} = E_0 + E \tag{2.9}$$

$$E_{loc} = E_0 - 2\left(\frac{\varepsilon_m-\varepsilon}{\varepsilon-2\varepsilon_m}\right)E_0 = \frac{3\varepsilon}{\varepsilon+2\varepsilon_m}E_0 \tag{2.10}$$

Extending problems with spherical symmetry to spheroidal particles (Gans theory), we can treat elongated nanoparticles in dipolar approximation regime (e.g. nanorods) and the extinction cross section is defined as[7]:

$$\sigma_{ext}(\omega) = \frac{2\pi}{3\lambda}\varepsilon_d^{3/2}V\sum_j\frac{(1/P_j^2)\varepsilon_2}{\{\varepsilon_1+[(1-P_j)/P_j]\varepsilon_d\}^2+{\varepsilon_2}^2} \tag{2.11}$$

Where $j = A, B, C$ are the three axes of the spheroid, with A>B

$$P_A = \frac{1-e^2}{e^2}\left[\frac{1}{2e}\ln\left(\frac{1+e}{1-e}\right) - 1\right] \tag{2.12}$$

$$P_B = P_C = \frac{1-P_A}{2} \tag{2.13}$$

$$e = \left[1-\left(\frac{B}{A}\right)^2\right]^{1/2};\ \frac{B}{A} = \frac{1}{R} \tag{2.14}$$

where R represents the ratio between the two dimensions of the nanostructure (R=A/B). In Figure 2.3 are shown the two oscillation modes along the two main axes, one transverse (B) and the other longitudinal (A) that lead to the presence of two bands in the extinction spectrum.

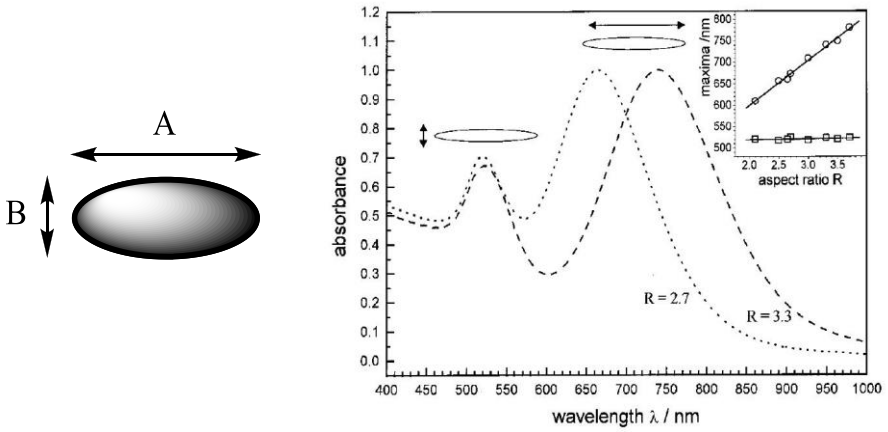

Figure 2.3**:** Extinction spectra of nanorod with different R values[7].

In this description is shown the shift of the longitudinal peak obtained by varying R: it is possible to tune the resonance peak from the visible and to the infrared region. Later it will be shown how this shift of the absorption peak can be exploited for very different application.

2.2 Nonlinear optics of metal nanoparticles

The presence of this strong absorption in metal nanoparticles generates an enhancement of several non linear phenomena, widely used in very different applications. Their description starts from the interaction between a material with electromagnetic radiation that causes a variation of the polarization, written as:

$$P = \chi(1)\,E + \chi(2)\,E^2 + \chi(3)\,E^3 + \ldots \qquad (2.15)$$

where P is the polarizability, χ the susceptibility and E is the electromagnetic field. Nonlinear phenomena will depend on different orders of the susceptibility.

The optical processes can be distinguished in parametric, or active, and non-parametric, or passive ones. While parametric processes involve virtual states, non-parametric ones are

characterized by a transfer of population from the ground to the excited state. The susceptibility (χ) odd orders express these passive processes: linear absorption is described by the first order of the imaginary part while nonlinear absorption depends on higher odd orders.

More common phenomena of the second order are second harmonic generation and sum-frequency generation, while example of third order phenomena are multi-photon absorption and optical Kerr effect. This last process has been largely used in optoelectronics to change the refractive index of the medium. When an intense light source crosses the medium, its refractive index is given by:

$$n = n_0 + n_2 I \tag{2.16}$$

where n_0 is the linear refractive index, n_2 the nonlinear index and I is the intensity of the incoming radiation. The nonlinear coefficient can be presented as function of susceptibility:

$$n_2 = \frac{12\pi^2}{{n_0}^2 c}\chi^{(3)} \tag{2.17}$$

This coefficient can be positive (self-focusing process) or negative (defocusing process). These kind of processes will be revealed using Z-scan analysis described in Chapter 4.

Among the multi-photon absorption, Two Photon Absorption (TPA), Saturable Absorption (SA) and Reverse Saturable Absorption (RSA) represent the more common processes involved in optical limiting mechanism, described below. These phenomena are optically revealed in a reduction (saturable) or increase (reverse saturable) of absorption.

Two photon absorption (TPA) involves a transition from the ground state of a system to a higher-lying state by the simultaneous absorption of two photons from an incident radiation field. After the interaction with the first photon and before the coherent state decays, a second photon is employed to excite the system to a real excited state (Figure 2.4).

The variation of the incident intensity with the optical path is given by:

$$\frac{\partial I}{\partial z} = -\alpha I - \beta I^2 \tag{2.18}$$

$$\beta = \frac{3\pi}{\varepsilon c n_0 \lambda} Im\left[\chi^{(3)}\right] \tag{2.19}$$

with α and β the one- and two-photon absorption coefficient respectively.

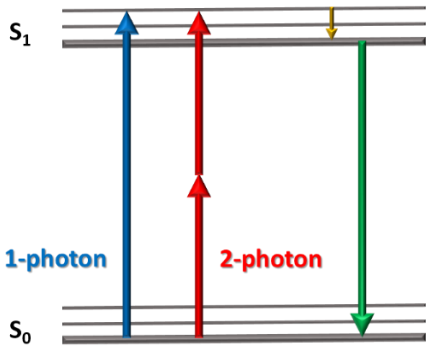

Figure 2.4: Scheme of one- (blu arrow) and two-photon (red arrows) absorption mechanisms.

Contrary to TPA, in the SA mechanism we have a decrease in the absorption coefficient at high incident intensities, with the material that becomes more transparent. In the case of RSA, instead, we have a two-step sequential absorption: a photon is excited from the ground state to an excited one and then can be photoexcited to another excited state (Figure 2.5). The probability of this process depends on the number of molecules in the first excited state.

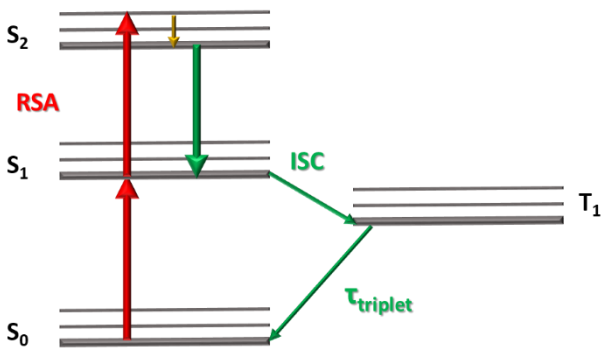

Figure 2.5: Scheme of reverse saturable absorption mechanism (red arrows).

Among the materials studied for application in optical limiting devices there are organic dyes solutions or doped solids[61–63] and metallic nanostructures[64,65]. A very recent study published on Nature Materials[66] shows a dyad system with a large RSA under weak continuous incoherent light. Authors exploit an accumulation by photosensitization of long-lived room-temperature triplet excitons in acceptors with a large triplet–triplet absorption coefficient that allows a

nonlinear increase in absorbance also under low-power irradiation conditions. The evident recent attention in the low power optical limiting mechanism in materials and in phenomena previously studied with pulsed laser, highlights the possibility to use optical protection devices also for cw lasers, which are increasingly exploited in the common use.

2.3 Thermal properties generated by cw laser irradiation

The thermo-optic process is one of the de-excitation channels of a molecule (or a particle) after an interaction with an electromagnetic radiation. It becomes the main mechanism if the interaction involves a cw source. The interaction can generate a strong beam deflection which can be caused by different effects: i) a thermal effect caused by a thermally induced refractive index gradient (dn/dT), and ii) a concentration induced effect, where the deflection is caused by a concentration induced refractive index gradient (dn/dC).
In the case of dyes embedded in solid matrices the more common effect is the first one, because the high temperature induces a density variation, causing the refractive index changes. In liquid samples the two effects could overlap and contributions will depend on the diffusivity power of the medium.

The thermal lens (TL) effect or thermal blooming was discovered by Gordon and co-workers[67] only a few years after the invention of the continuous wave (cw) laser. The TL effect may be described as a change in the optical path of the sample induced by absorption of a laser beam. The heat increases the temperature in the centre of the beam profile and creates a refractive index gradient.
Most liquids expand upon heating, which lowers the refractive index (n), changing the optical path along the sample. The resulting thermo-optical element has the shape of a negative lens that causes the laser beam to diverge. This type of limiting action can be understood with the simplified model shown in Figure 2.6

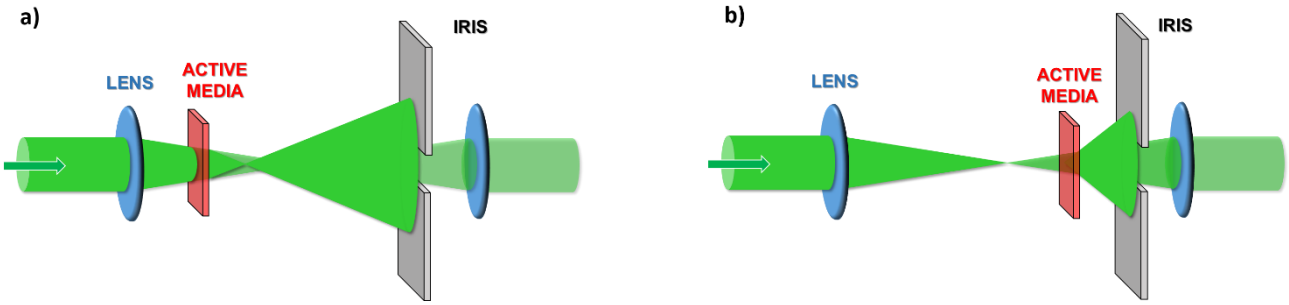

Figure 2.6: Typical optical configuration for a) self focusing and b) self defocusing active media

In addition, in the simplest case, the change in index due to the incident beam is linearly dependent on the incident excitation intensity or fluence. Hence, the radial dependence of the intensity gives rise to a radially dependent parabolic refractive index change near the beam axis. That is,

$$\Delta n = \frac{\Delta n_0 e^{-2r^2}}{\omega_0^2} \approx \Delta n_0 \left(1 - \frac{2r^2}{a\omega_0^2}\right) \tag{2.20}$$

where Δn, is the on axis index change, r is the radial distance, ω_0 is the electric field radius associated with the beam in the medium, and a is a correction term to the Taylor expansion for higher order terms. For the thin nonlinear medium of thickness L, the parabolic approximation yields a thin spherical lens with a focal length of:

$$f = \frac{a\omega_0^2}{4\Delta n L} \tag{2.21}$$

Equation (2.21) clearly demonstrates that the effective focal length of the lens decreases as the strength of the nonlinearity (Δn) increases. If the nonlinearity of the medium is negative, then the resulting focal length is negative and self-defocusing occurs. On the other hand, if the nonlinearity is positive, the effective focal length of the induced lens is positive and self-focusing occurs.

A large body of experimental work is based on the application of nonlinear refraction for optical limiting; perhaps, the first such demonstration was reported by Leite et al.[68] who used thermal lensing in a cell of nitrobenzene.

Exploiting this phenomenon, the photothermal technique has been developed, able to investigate the optical properties of materials, which cannot be studied with traditional

spectrophotometry. With this technique, the energy absorbed by the material as a result of its interaction with the incident radiation, is measured directly and the heat produced by nonradiative decay of excited species acts to modify the optical properties of the sample. In the case of metal nanoparticles the very localized and very rapid photothermal heating can be achieved to produce new effects.

In the last two years a particular interest has been given to thermal properties of these metal nanosystems for different applications, generated by a cw laser irradiation. In optical limiting (as analyzed in Chapter 4) with the spread of an incoming radiation[14].
Applications in 3-D optical storage[69]are permitted for the high absorption cross section and fast electron-phonon thermalization of metal nanostructures. The use for energy conversion or sensitizer for optical storage media is comparable to phtalocyanine dyes and GeSbTe (GST): photothermal energy conversion induce a phase change or decomposition of recording mask. Gold nanoparticles are being studied also as light localizer in solar cell devices[70]: this phenomenon is due to a collective effect mediated by multiple light scattering from the dispersed nanoparticles that both scatter and absorb light. They are able to concentrate light energy into mesoscale volumes near the illuminated surface of the liquid and create intense localized heating and efficient vaporization of the surrounding liquid.
Other applications of these systems in recent studies are light modulation[71], Plasmonic heating litography[72], Photothermal Probing[73] and thermoplasmonic[74]. Until now only preliminary studies have been performed, but this new interest in thermal responses of plasmonic structures persuades us to future applicability of these systems. More common research are represented by photothermal therapy, but several recent studies confirm the renovate interest in this field[54,55,75,76].

2.4 Optical limiting

The optical limiting effect is an increase of opacity of a material after the interaction with an incident light with intensity over a certain threshold (Figure 2.7). This kind of limitation effect

can be achieved with all the nonlinear phenomena described in the paragraphs above as TPA, RSA, Kerr effect, scattering, etc.

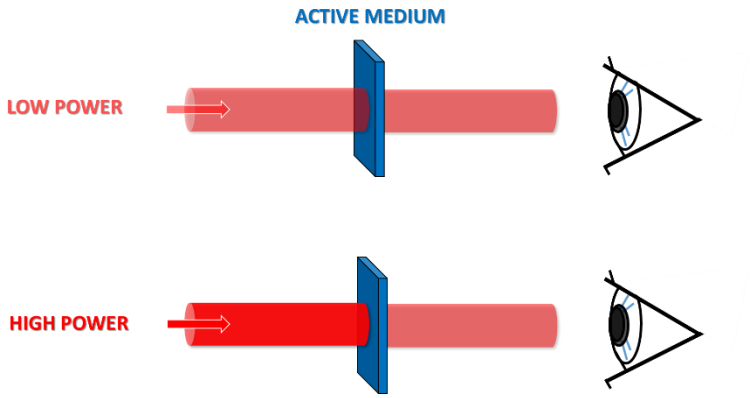

Figure 2.7: Scheme of the OL mechanism.

This required "control of light by light" is exploited for the protection of sensors, in particular the human eye, against laser radiations: in particular a good protection device should be a "smart material" able to activate the protection at high energy with a large dynamic range and in a wide wavelength spectrum. The last property is especially required in the case of military use, for protection against laser pointing devices or blinding weapons of unpredictable emission wavelength.

Active materials, useful for optical limiting, should possess high solubility in suitable solvents and solid matrices, fast response and good linear transparency. Generally, with short pulses (in the nano and picosecond range), fullerenes, metal phtalocyanines and metal porphyrins[63,77–82] are considered, where processes involved are mainly TPA and RSA.

Recently, attention has turned to optical limiting processes generated by cw laser[39,83–86]. When an optical material is irradiated with a focused cw laser beam, the absorbed energy may induce a local heating and a temperature gradient corresponding to a refractivity index variation across the sample. In this way, even a flat sample acts as a focusing or defocusing lens and spreads the laser beam. An exception to these studies is represented by the optical limiting mechanism of carbon black suspensions against pulsed laser[87]: authors ascribe the nonlinear scattering to a rapid heating of carbon particles and their subsequent vaporization and ionization, which lead

to the formation of rapidly expanding microplasmas. This thermal response has been pointed out in the recent years as the main reason of optical limiting results with gold nanospheres. These studies show the importance of different parameters as particle size[2,6–8,88–92], balancing the scattering and the absorption contribution, and the shape [93–97], changing the strong visible plasmon absorption of gold nanospheres into the near-infrared with rod-like particles. The mechanisms proposed for the optical limiting properties of gold nanoparticles include nonlinear scattering. Literature of very recent years[94,98,99,99–101], including patents, suggests that a concerted effort to study gold nanoparticles as a function of size, shape, and in the presence of interesting chromophores, is needed.

2.4.1 Requirements for the realization of a power limiter device

Sensor protection is defined as anything that can be used to protect optical systems and human eyes from debilitating laser effects. The optimal design of an optical limiting device requires some knowledge of the sensor and optical arrangement leading to the sensor, as well as the nature of the most likely threat. It is necessary to determine the limiting thresholds, the sensor bandwidth, the dynamic range, as well as the sensitivity and the field of view, minimizing the losses of performance under normal operating conditions.

Different phenomena can be achieved to limit incoming light into the sensor or eye: blocking, scattering, diffraction or absorption of incoming laser light. The goal device should be sensor protection that would provide the least amount of impact on a view capability while removing the risk of incapacitation due to a laser threat. The simplest configuration for optical limiting is realized by simply placing a nonlinear absorber or scatterer in front of the sensor.
The main sensor protection used was predominantly neutral density filters but they present a very low transmittance (10-20%) and colour distortion, reducing their efficiency, or shutter systems, that respond in 10 μs, not sufficient to prevent damage from pulsed laser. In both the cw and pulsed cases, however, the optical system is effective if the activation is extremely fast. What scientist are trying to do in the recent years is to obtain a device that can rapidly tune off unpredicted wavelengths through an active interaction with the laser radiation. Over the last

decade, innovative techniques have been developed: passive devices, those that are activated by the incoming radiation itself, are seen as the best approach to counter the frequency agile, short pulse threat.

The effectiveness of the device over the entire operating wavelengths (broadband operation) is one of the most important requirements. Every sensor protection device or material integrated into new sensor system design must have a minimal impact on the operating performance of the sensor. The dynamic range is the ratio between the input energy at which the device fails and the input energy, at which it begins to protect. The ratio of transmitted energy to maximum incident energy, in terms of orders of magnitude, is referred to as optical density (OD):

$$OD = -log_{10}\left(\frac{E_T}{E_{max}}\right) \tag{2.22}$$

where E_T is the Transmitted Energy and E_{max} the Maximum Incident Energy Before Device Failure.

In general, for systems involving the human eye, an OD of 4 is chosen as the desirable maximum protection[102]. In some cases, system failure results in damaging the sensor protection device which limits even more radiation to enter the eye. This is the case of a solid host which results irreversibly damaged when the thermal heating becomes too large. The most widely studied optical limiters rely on either liquid or solid nonlinear media. Liquid limiters are often very desirable because they are extremely resilient. The energy from high intensities is typically dissipated by solvent heating and bubbling which, for sufficiently long pulses, adds extra reversible protection through scattering. The thermal dissipation can be a limit in a solid material, because of irreversible degradation of the matrix, but this process is fail-safe for the sensor.

Additional design requirements that must be taken into consideration are the environmental stability of the material or device and its toxicity. The major part of the studies concerning smart materials have been conducted in solution, with faster responses but usually in organic volatile solvents. For a personnel protection, a goggle-type optical limiting device is highly desirable. Sandwiching a thin nonlinear medium between a pair of lenslet arrays, it will be possible to reimage the light to the eye. Thus, if the lenslets are sufficiently small, they will act as pixels

and eventual material damage will be localized in a small spot. Moreover the lenses will provide the focalization required for the activation of the optical limiting process.
Sandwiching a thin liquid film of nonlinear medium between a pair of lenslet arrays can be dangerous in the event of brake, especially when toxic solvents are involved. For this reason, a liquid limiter for goggle protection is not desirable and have been replaced in favour of solid state devices.

The ANSI Z-136.1[103] exposure limits for visible light (400 to 700) nm for times between 18 x 10^{-6} to 10 seconds can be obtained from the relation, using a 300 ms exposure time (t):

$$MPE = 1.8 \times t^{\frac{3}{4}} = 0.7296 \left[\frac{mJ}{cm^2}\right] \tag{2.23}$$

Where the maximum exposure limit (MPE) is given in terms of an energy flux (or fluence) as if the energy were evenly distributed across the incident beam. For laser safety calculations, a 7 mm, aberration-free pupil is assumed: a worst-case assumption.
The MPE defined in this way can be recast in terms of maximum transmitted energy that a protection device should guarantee in 300 ms, that is the blinking time:

$$E = MPE \times (pupil\ area) = 0.7296 \times 0.3848 = 0.28\ mJ \tag{2.24}$$

In Chapter 5 and Chapter 6 we will compare and discuss the results obtained with our systems with these pursued thresholds

Chapter 3

3 SYNTHESIS AND CHARACTERIZATION OF METAL NANOSTRUCTURES

In this chapter, we describe different syntheses and functionalization of gold nanostructures. The chemical reduction method has been chosen because it presents several advantages with respect to other physical methods, mainly for the variety of solvent that can be used and for the high control of size and shape of the structures that can be obtained. We prepared nanostructures with various shapes that present different linear and nonlinear optical properties.

Gold spherical nanoparticles (NPs) present a plasmon resonance that is not widely tunable, but we used them as a starting model for their easy synthesis and quite simply functionalization. Nanoparticles with a tunable plasmon band in the visible and near infrared regions, such as nanorods (NRs) and nanoshells (NSs) have been prepared in order to obtain large nonlinear optical responses under irradiation with a strong electromagnetic field in resonance conditions.

3.1 Synthesis of nanostructures: growth and stabilization mechanism

The colloidal method is based on a thermodynamic approach that consists in the nucleation of small particles and their subsequent growth. The mechanism of nuclei formation in dilute solutions is usually described according to the nucleation theory of fluctuation. This requires the formation of a supersaturated solution of metallic gold atoms, some of which coalesce into a nucleus when the statistical fluctuation of their concentration reaches values sufficiently large to allow the formation of a stable particle.

This mechanism occurs spontaneously when the Gibbs free energy of the system is negative:

$$\Delta G = \Delta G_V + \Delta G_S < 0 \tag{3.1}$$

$$\Delta G_V \propto -\frac{4\pi}{3} R^3 k_B T ln\left(\frac{C}{C_0}\right) \tag{3.2}$$

$$\Delta G_S \propto 4\pi R^2 \gamma_{S-L} \tag{3.3}$$

ΔG_V is the Gibbs volume free energy related to the particle volume and it is negative because energy is released into the liquid in solid transformation. ΔG_S is the surface Gibbs free energy: in this case the value is positive because energy is used in the formation of the liquid-solid interface. C and C_0 are the concentrations of precursor before the nucleation and at equilibrium, respectively. The ratio between these quantities is called oversaturation and is the driving force for the nucleation process; γ_{S-L} is the surface free energy of the liquid-solid interface.

Differentiating Equations 3.4 with respect to the radius, we obtain the critical radius and the critical energy that a nucleus must have to grow and reduce the free energy:

$$R_C \propto \frac{\gamma_{S-L}}{k_B T ln\left(\frac{C}{C_0}\right)} \text{ and } \Delta G \propto \frac{{\gamma_{S-L}}^3}{\left[k_B T ln\left(\frac{C}{C_0}\right)\right]^2} \tag{3.4}$$

By increasing the change of Gibbs volume free energy ΔG_V and reducing the surface free energy of the new phase $\gamma_{S\text{-}L}$ one can reduce the critical size R_C and the free energy ΔG. Equations. 3.4 are inversely proportional to the supersaturation: the higher the supersaturation, the lower the energy barrier to overcome in order to form clusters.

In Figure 3.1 a scheme of the concentration of precursor as a function of time is shown: when the solute concentration, during nucleation, decreases to the minimum nucleation concentration, nucleation stops and growth begins.

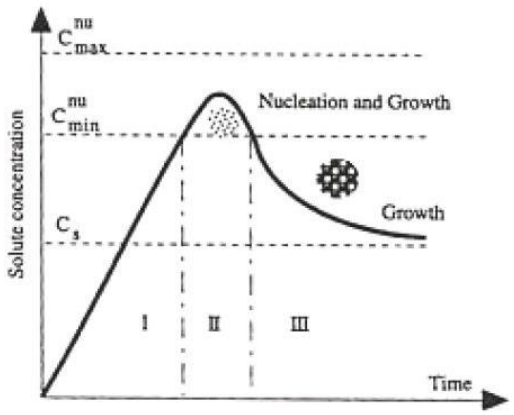

Figure 3.1: Solute concentration as a function of time: nucleation and growth processes[104]

The growth process can be controlled by the diffusion of the solute to the nuclei and the adsorption and incorporation of the solute into the nuclei. The limiting step will determine the dimensional distribution of the nanoparticles in solution. If the growth process is under diffusion control, the slow stage is reaching the surface of a particle and the distribution will be monodisperse. If the diffusion is fast and the adsorption is the limiting process, the slow stage of reaction is in absorbing species and this may lead either to a growth layer by layer or to a polynuclear growth.

Also, the surface energy has to be taken into account because in a crystalline solid like gold, different crystal facets possess different surface energy and not exactly spherical nanostructures are synthesized. For example, nanorods synthesis exploits the selective attachment of CTAB to some gold crystalline facets to orient the growth along one single axis[105,106]. Anisotropic growth is commonly realized through a faster development along a certain orientation, faster than other directions. A significant role in the final morphology depends also on defects and impurities at the growth surface.

Another important aspect is the stabilization of the nanoparticles because the aggregation process in solution through Van der Waals forces is a thermodynamically favoured mechanism. The stabilization of the colloidal solution for keeping the nanoparticles monodispersed can be achieved with two different approaches: electrostatic and steric. The theory of electrostatic stabilization of colloidal nanoparticles[107] (DLVO), developed in the early 1940, states that the stability of the colloidal solution is given by the sum of attractive Van der Waals forces and

repulsive ones given by the double electrostatic layer on the nanoparticles surface. The combination of opposite forces gives rise to an energy barrier which avoids particle coalescence. This scheme is depicted in Figure 3.2.

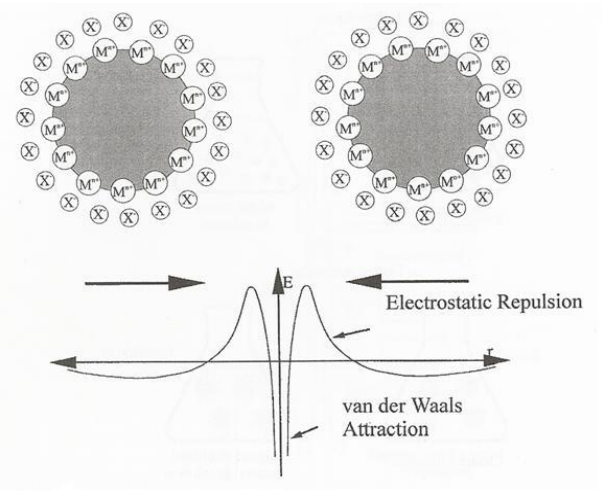

Figure 3.2: Scheme of the DLVO theory [108].

For a stable solution the energy barrier has to be high enough because when the energy barrier is exceeded the particles begin to coalesce due to Van der Waals forces. The double layer thickness decreases with increasing concentration and valence of the counter-ion, and increases with increasing dielectric constant of the solvent. The presence of ions in solution (the ionic force slightly increases) can cause a sort of a secondary minimum, where little nanoparticles aggregates can be stabilized, but this situation is very difficult to obtain experimentally.

Nanoparticles surface can be charged through ionization or dissociation of surface species or by adsorption of charged species, and its charge will be balanced by counter ions. In Figure 3.3 are represented the exponentially decay of the surface potential.

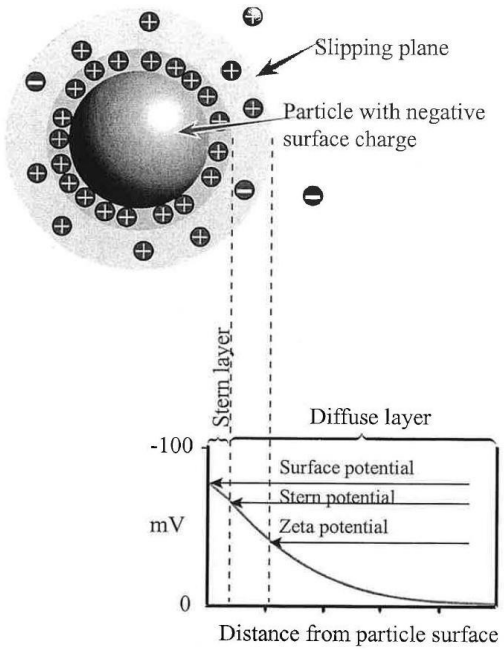

Figure 3.3: Scheme of the electrostatic double layer and potentials in the diffuse layer[108].

In particular, the surface potential at the interface between electrostatic double layer and solution is known as Z-potential. Its value gives an idea of the stability of the colloidal solution and can be measured: if the value is between 30 and 50 mV, negative or positive, the colloid is stable.

The steric stabilization is often easier to obtain, e.g. with polymers or surfactants, although it can present problems for further functionalization. The steric volume of the molecules avoids the nanoparticles to come too close together and therefore to aggregate.

3.2 Materials and characterization techniques

We synthesized the following gold nanostructures: nanoparticles, nanorods and nanoshells in water.

Gold (III) chloride solution 30% w/w in dilute HCl ($HAuCl_4$), silver nitrate ($AgNO_3$), sodium citrate dihydrate ($Na_3C_6H_5O_7 \cdot 2H_2O$), Tetraethyl orthosilicate (TEOS), cetyltrimethylammonium bromide (CTAB), Tetrakis(hydroxymethyl)phosphonium chloride (THPC) 80% in water, 3-Aminopropyl)trimethoxysilane (APTMS), sodium borohydride

($NaBH_4$), ascorbic acid, formaldehyde solution, potassium carbonate (K_2CO_3) and Polyvinylpyrrolidone (PVP, average mol wt 40000), purchased from Sigma-Aldrich, and m-PEG-SH (mol wt 2000), purchased from Laysan Bio Inc., are used without further purification. PC (Calibre 200–14) was provided as pellets LEXAN* OQ4320R resin, with a refractive index of 1.585 and density of 1.2 g cm^{-3}.The synthesis were performed in deionized Milli-Q filtered water.

Colloidal samples were characterized through UV-Vis absorption spectroscopy, dynamic light scattering (DLS), Z-potential and transmission electron microscopy (TEM).

3.2.1 UV-Visible Absorption Spectroscopy

The UV-Vis absorption spectra were collected with a Cary 5 Varian instrument. The deuterium lamp provides the UV region wavelengths, while a quartz-iodine halogen lamp works in the visible and infrared region. Measurements were performed using quartz cells with optical path of 1 or 10 mm or directly on thin films (polycarbonate or silk) of around 100 μm thickness.

3.2.2 Raman Spectroscopy

Raman measurements were carried out in a home-made setup equipped with an upright microscope (Olympus BX 41, 20x objective) coupled to a triple subtractive spectrograph (Jobin Yvon S3000). The Raman signal was detected by a liquid nitrogen cooled CCD (Jobin Yvon, Symphony). The laser source was an Ar^+/Kr^+ gas laser (Coherent, Innova 70) providing the lines at 488, 514.5, 530.8, 568 and 647.1 nm.

3.2.3 Transmission Electron Microscopy

Transmission electron microscopy (TEM) gives the possibility to analyze the morphology of a sample at high resolution. The electron generator is a field emission gun, where the electrons are extracted from a tungsten filament. The electron beam is then focused on the sample by electronic and magnetic lenses (condenser). The interaction between electrons and the sample atoms can generate elastic or inelastic scattered electrons. The elastic scattered electrons were deflected by an objective lens on a focal plane, where the diffraction image is collected. After

the focal plane the scattered beams are then focalized through another lense system on the image plane, where the constructive and destructive interference of the electrons creates the sample image. From bright field images it is possible to construct the dimensional distribution histogram of the observed nano-objects.

In the present work the samples were prepared by putting some drops of liquid sample on a copper support mesh grid. To prevent charge build-up at the sample surface, the samples need to be coated with a thin layer of conducting carbon material. The instrumentation used is a Field-Emission Gun (FEG) Tecnai F20 Super-twin TEM operating at 200 keV.

3.2.4 Dynamic Light Scattering and Z-potential measurements

Dynamic Light Scattering is also known as Photon Correlation Spectroscopy. This technique is one of the most popular methods used to determine the size of particles. Shining a monochromatic light beam, such as a laser, onto a solution with spherical particles in Brownian motion causes a Doppler Shift when the light hits the moving particle, changing the wavelength of the incoming light. This change is related to the size of the particle. It is possible to compute the sphere size distribution and give a description of the particle's motion in the medium, measuring the diffusion coefficient of the particle and using the autocorrelation function, i.e. a measure of how the intensity at time (t+τ) is correlated to the intensity at time t (Figure 3.4).

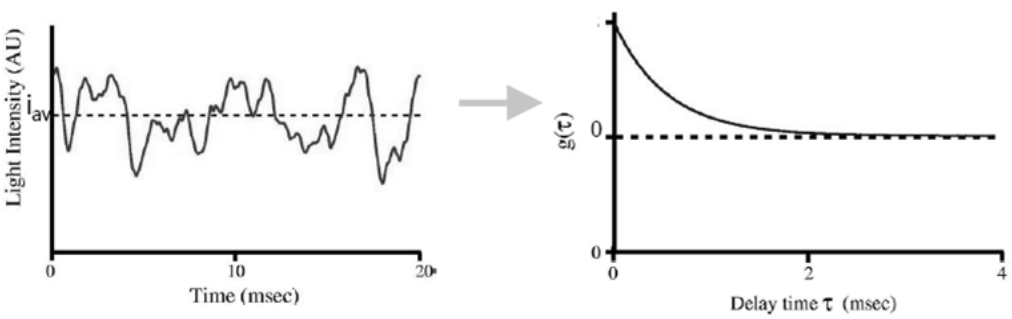

Figure 3.4: Light intensity fluctuation (left) and related correlation function (right).

The DLS instrument measures the degree of similarity between two signals over a period of time and constructs the correlation function $G(\tau)$:

$$G(\tau)^2 = \langle (I(t) - I_{av})(I(t+\tau) - I_{av}) \rangle \quad (3.5)$$

that can be written as

$$G(\tau)^2 = ce^{-2h^2 D\tau} \quad (3.6)$$

For a large number of monodispersed particles in Brownian motion we can relate the diffusion coefficient to the hydrodynamic radius through the Stokes-Einstein relation:

$$R_h = \frac{k_B T}{6\pi\eta D} \quad (3.7)$$

where k_B is the Boltzmann constant, T the temperature and η the viscosity of the solvent. This hydrodynamic radius of the particle can be calculated by fitting through Equation 3.7, using the known values of temperature, viscosity and sample concentration.

For Z-potential measurements, an electric field is applied inside the liquid sample: the charged particles will then move with a velocity that depends on the dielectric constant, the solution viscosity and the Z-potential. In our work DLS and Z-potential measurements are performed on nanoparticles in solution with a Malvern Zetasizer Nano ZS with a 633 nm laser excitation.

3.3 Synthesis and characterization of metal nanostructures

3.3.1 Synthesis and characterization of gold nanospheres

In the literature, there is a huge number of recipes for the synthesis of gold nanoparticles, but the most popular one is the synthesis developed by Turkevitch[109] in 1951 in water. This system was used as a model for subsequents studies of gold nanorods and nanoshells.

In the well known Turkevitch synthesis, $HAuCl_4$ is reduced by sodium citrate in water. Sodium citrate works both as reducing and stabilizing agent. By varying the ratio between $HAuCl_4$ and citrate and the reduction temperature, it is possible to prepare particles of different size and monodispersity and to red shift the plasmon band starting from approximately 520 nm (Figure 3.5).

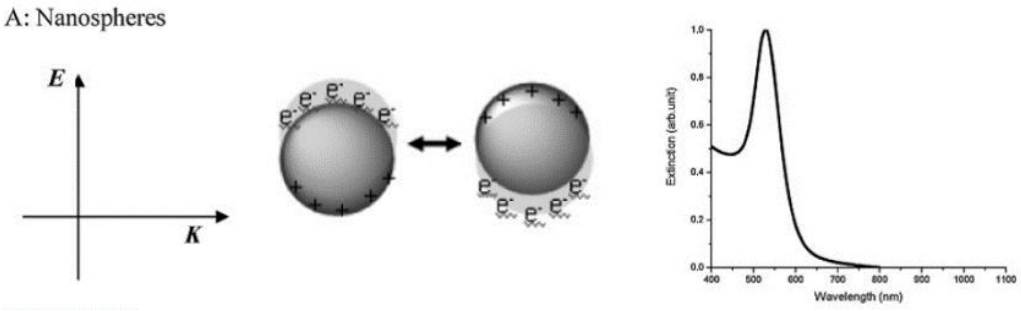

Figure 3.5: Schematic illustration of the interaction of polarized light and gold nanospheres to form the electronic coherent SPR[49]

In this thesis work Au NPs in aqueous solution were synthesized through the citrate Turkevich method[109]. For the preparation of Au NPs solutions, 1 ml of a 39 mM aqueous solution of sodium citrate were added to 9 ml of a 1 mM solution of Gold (III) chloride 30% w/w in dilute HCl, under reflux conditions. The reaction is kept for 30 min under vigorous stirring.

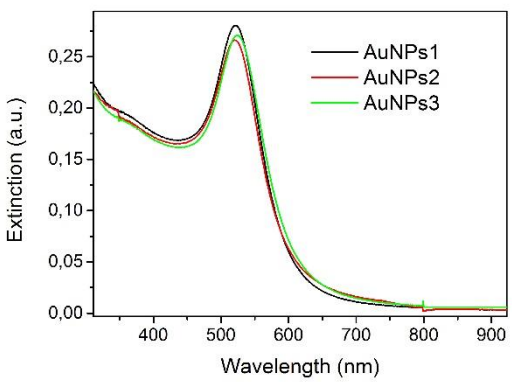

Figure 3.6**:** Extinction spectra of three different AuNPs (right) colloidal solutions.

As predicted, the synthesis is very reproducible (Figure 3.6), and it is easy to obtain stable and monodisperse solution of AuNPs. In Figure 3.7 a TEM image and the histogram of the dimensional distribution of AuNPs3 is reported.

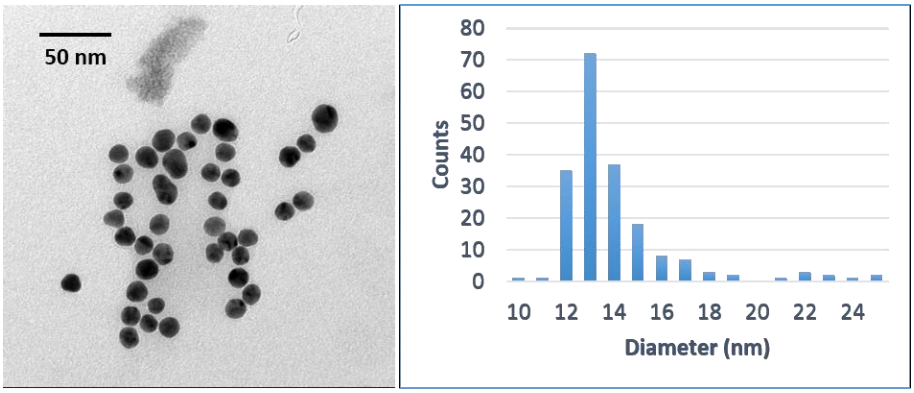

Figure 3.7: TEM image of a gold colloidal solution (left) and histogram of the dimensional distribution (right).

The concentrations of Au NPs in solution, expressed as NPs/ml, can be calculated with different methods.

In addition to the mean diameter extracted by histogram of the dimensional distribution, when TEM analysis is available it is possible to calculate NPs concentration using a different mathematical method:

$$w(Au) = NPs \cdot \rho(Au) \cdot \frac{4}{3}\pi \sum_{n} R_n^3 A_n \tag{3.8}$$

w(Au) is the weight of gold calculated from the precursor amount assuming all the gold precursor is reduced by sodium citrate (ICP-AES measurements are performed to demonstrate that more than 99% of gold precursor is reduced). ρ(Au) is the bulk weight density of gold. R_n and A_n are parameters extracted from the TEM histogram: R_n is the mean radius for each n histogram column and A_n is the fraction of Au NPs with the n-th mean radius. By this way, the total number of nanoparticles (NPs) is calculated taking into account the observed distribution of NPs dimension and not only its mean value[110]. The error affecting NPs is then calculated through a series expansion of the errors on R_n, according to the expression:

$$\sigma_{NPs}^2 = \sum_{n} \left[\left(\frac{\partial NPs}{\partial R_n} \right)^2 \cdot \sigma_{R_n}^2 \right] \tag{3.9}$$

Doing so, the errors on precursor mass and solvent volume are considered negligible, whereas the error of R_n (σ_{R_n}) is equal to half the width of each *n*-th column of the TEM histogram. Once the total number of NPs is established, the concentration of Au NPs (NP/ml) is calculated as the ratio of NPs to the solution volume.

With this method, 120 nanoparticles have been analyzed for solution AuNPs3 with a resulting dimension of (14±2.6) nm diameter and a concentration of (6.1 ± 0.3) x 10^{12} NP/ml.

A faster method of estimating the NPs dimension and concentration is fitting the UV-Vis spectrum in solution with the Mie-Gans relation and extracting the extinction cross section[111]. The resulting diameters for AuNPs 2 and AuNPs 3 are 14 nm and 16 nm diameter and concentrations are 6.8 x 10^{12} NP/ml and 5.1 x 10^{12} NP/ml, respectively. The values of the AuNPs3 are similar to that calculated with the above described TEM method (within 11% error) and could be a very interesting alternative when no TEM analysis is available.

DLS gives for the three solutions a diameter of 16, 18 and 19 nm respectively. Results are higher than the TEM ones because the method of calculation overrate bigger nanoparticles. Z-potential measurements confirm the stability of the AuNPs solutions, with values of about -45÷ -40 mV are obtained.

3.3.2 Synthesis and characterization of gold nanorods

Once size control and monodispersity have been reasonably achieved, the next level is achieving shape control: synthesis of non-spherical nanoparticles where not only the size, but also other topological aspects can be controlled changing experimental conditions and additives, as surfactants, ligands, adsorbates (Figure 3.8).

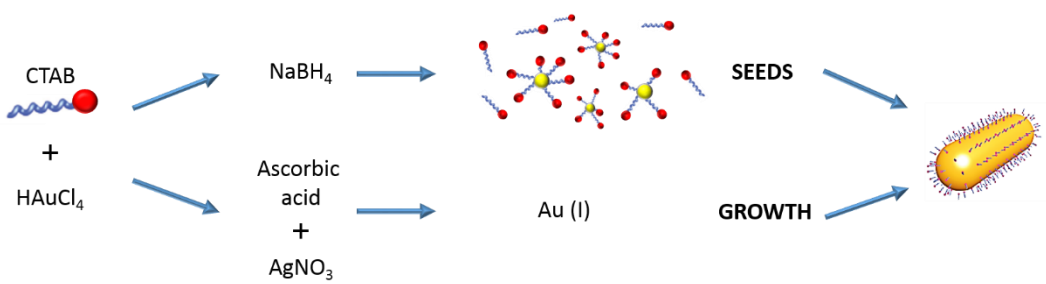

Figure 3.8: Schematic illustration of the seed-mediated for the growth of Au nanorods

The specific mechanisms governing morphology and geometry control over particle growth are not so well understood, but different theories has been proposed[112,113].

In the case of gold nanorods, electron oscillation can occur in one of two directions depending on the polarization of the incident light: the short and long axes. The excitation of the surface plasmon oscillation along the short axis (transverse band) induces an absorption band in the visible region at wavelength similar to that of gold nanospheres (Figure 3.9). Much stronger absorption band in the longer wavelength region (longitudinal band) are induced exciting the surface plasmon along the long axis. The longitudinal band is affected by the size of nanorods and is red-shifted from the visible to near-infrared region with increasing aspect ratio (length/width)[49]. This optical behavior can be well understood according to Gans[114] theory which was developed for the explanation of optical properties of ellipsoid particles based on a dipole approximation.

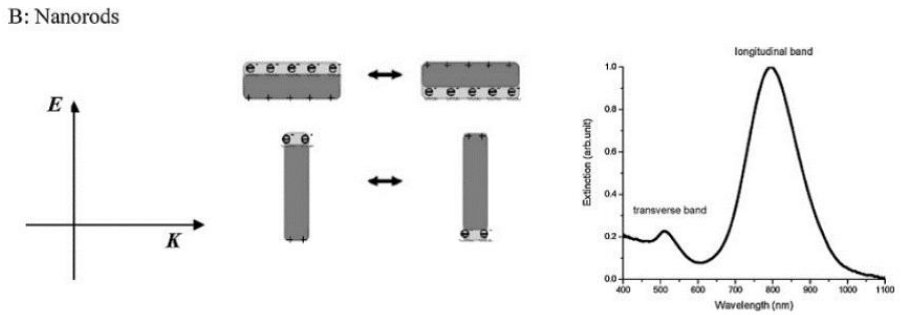

Figure 3.9: Schematic illustration of the interaction of polarized light and gold nanorods to form the electronic coherent SPR[49]

In aqueous media, hexadecyltrimethylammonium bromide (CTAB; Scheme 1) has been one of the most popular molecules in the synthesis of metals[105,115].

The as-grown Au nanorods using the seed-mediated method usually possess hemispherical heads. Close inspection of the heads indicates that they are enclosed with {110}, {111}, and {001} facets[106]. The formation of such structures is attributed to the site dependence of the CTAB binding strength on the surface of the nanorods. CTAB molecules are believed to preferentially bind to the middle cylindrical surfaces of the nanorods. This preferential binding

causes more Au atoms to be deposited at the ends, leading to the production of the dog-bone-like nanorods (Figure 3.10).

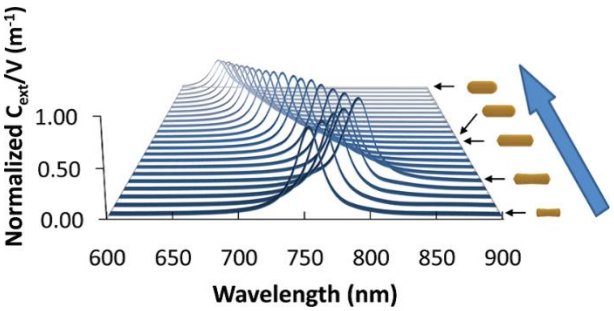

Figure 3.10: Schematic illustration of the UV-Vis spectrum change of the growth of Au nanorods[53]

Gold NRs synthesized in water present two plasmon bands due to their asymmetric structure. The one at lower wavelength (520 nm) arises from the electrons coherent oscillation along the short axis and is know as transverse mode and it is equivalent to the plasmon oscillation in a spherical particle of the same size. The second band arises from the electrons coherent oscillation along the long axis (longitudinal mode). The longitudinal plasmon wavelength is strongly tunable and it red shifts on increasing the rod length. The synthesis of gold nanorods is a two-step process: first a seeds solution is prepared and then the seeds are let grow along one preferential direction, thanks to a rod-like micellar environment. In this work, growth and seed solutions were prepared according to the protocol described by Jana et al.[105] Au seeds, smaller than 3 nm, were prepared by mixing equal portion (5 mL) of an aqueous 0.2 M CTAB solution and a 0.5 mM HAuCl4 solution, followed by the injection of 10 mM NaBH4 solution (0.6 mL) as reductant. Au seeds were then added to the growth solution composed by an aqueous solution of 0.08 M CTAB (5 mL) with 0.01 M AgNO3 (various quantities from 0.3 to 0.05 mL). The presence of $AgNO_3$ is essential for producing and controlling the aspect ratio of spheroids and rods nanostructures. The growth solution was treated with 0.024 M $HAuCl_4$ (0.5 mL) and 0.08 M ascorbic acid before the injection of the seed solution. In this way, we obtained NRs with aspect ratio from 1.9 to 2.4, with a longitudinal plasmon band at 620-680 nm (Figure 3.11).

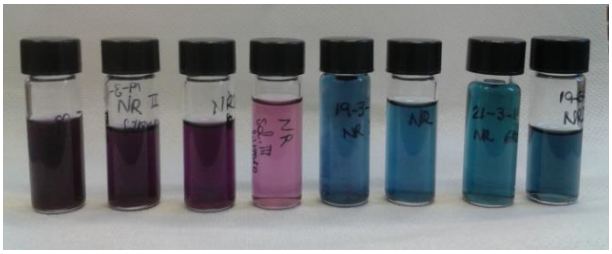

Figure 3.11: Photograph of AuNRs solution with different aspect ratio

All the syhteses conditions are resumed in Table 3.1. Differences in AuNRs absorption spectra of the samples with the same starting condition depend on little differences in the seed solutions that represent the critical step in the reproducibility in the synthesis.

Table 3.1: Reaction condition for nanorods synthesis after the addition of 12μL of seed solution

Solution	***CTAB***	***HAuCl4***	***AgNO3***	***Ac. asc.***
AuNRs 3	5mL	5mL	200 uL	70 uL
AuNRs 5	5mL	5mL	200 uL	70 uL
AuNRs 8	5mL	5mL	200 uL	70 uL
AuNRs 10	5mL	5mL	200 uL	70 uL
AuNRs 11	5mL	5mL	125 uL	70 uL
AuNRs 12	5mL	5mL	175 uL	70 uL

In order to functionalize the NRs with molecules soluble in organic solvents, we tried to stabilize and transfer them to a compatible solvent. Instead of using the functionalization method described by Jebb et. Al., requiring dodecanthiol, we tried to stabilized nanorods with polyvynilpyrrolidone (PVP). In this way, the subsequent functionalization with thiolated molecules does not require the thiol-thiol replacement but only a molecules displacement, faster and more efficient. After 3 hours the solution can be centrifuged, and re-dispersed in organic solvents with low aggregation effects.

Nanorods synthesized in this work have different UV-Vis absorption spectra, shown in Figure 3.12 induced by the difference in concentration of solutions and the ratio between longitudinal and transversal dimension.

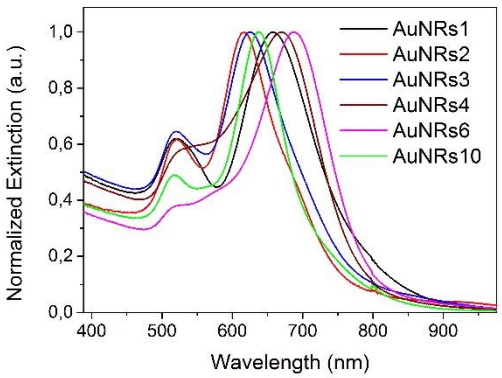

Figure 3.12: Different AuNRs synthesis with plasmon resonance peak tunable in the visible range

Nanorods grow and modify their shape between 20 minutes and an hour, and we followed the process through UV-Vis absorption. It is visible in Figure 3.13 the characteristic blue shift of the longitudinal resonance peak, that moves from 730 to 670 nm, while the transversal peak at 520 nm increase in intensity.

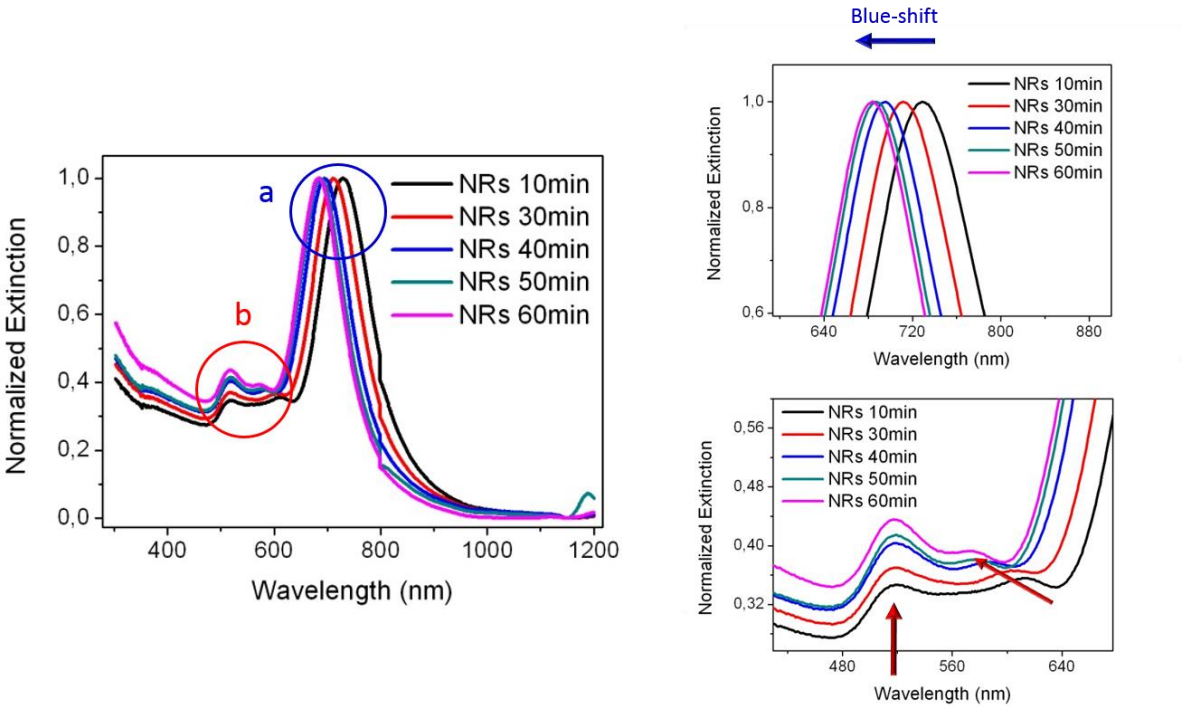

Figure 3.13: Normalized UV-Vis absorption spectra of AuNRs1 growth in 60 minutes

We characterize the nanorods shape the day after the synthesis with TEM analysis and conduct statistical calculation on the longitudinal and transversal dimensions.

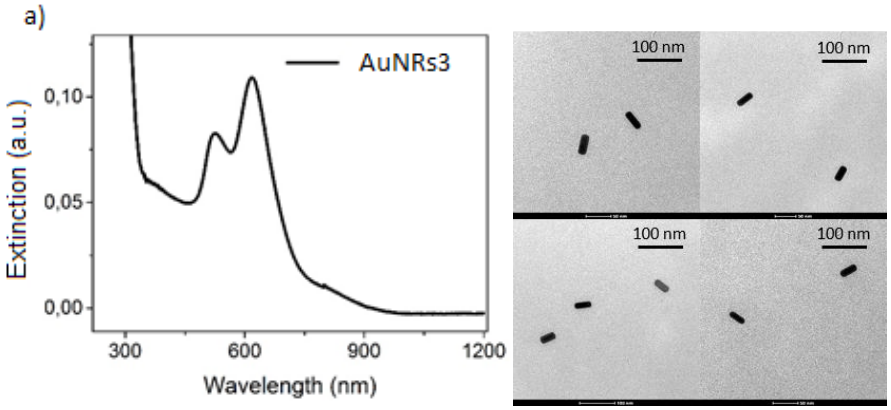

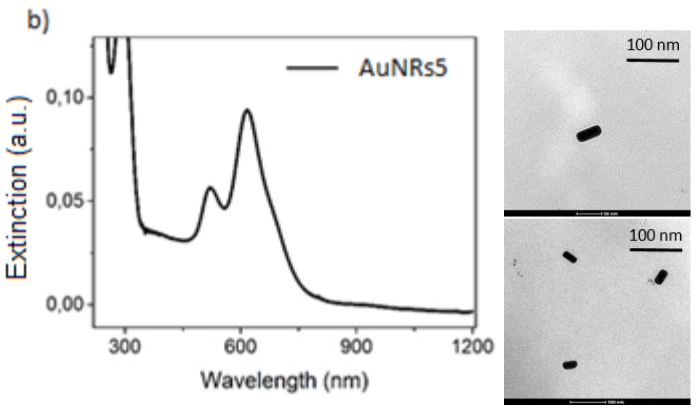

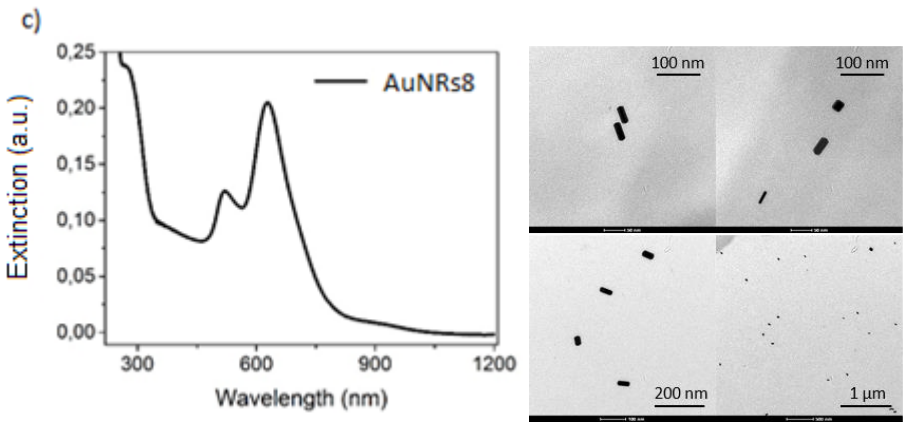

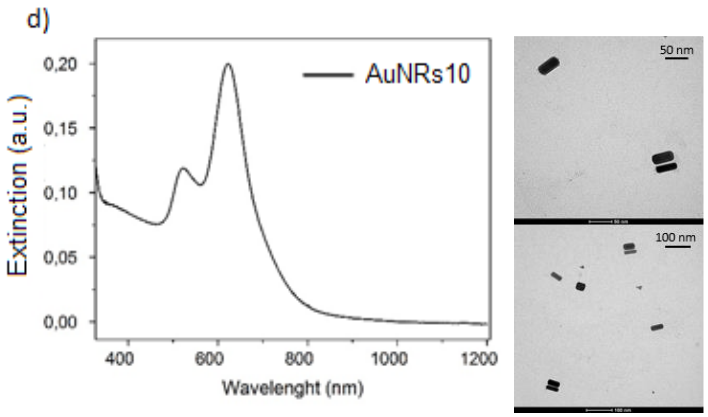

Figure 3.14: UV-Vis absorption spectra and TEM images of a) AuNRs3 b) AuNRs5 c) AuNRs8 and d) AuNRs10

Solutions result very dilute but we decided to not centrifuge to improve concentration in order to prevent aggregation and few AuNRs per image has been collected. Results are resumed in Table 3.2. The monodispersion of nanorods is not as high as for nanospheres: for three samples we find a dispersion of around 10-20%.

Table 3.2: Statistical calculation by TEM analysis for three nanorods synthesis, where N represent the number of nanoparticles analyzed, d_{TRAN} and d_{LONG} the transversal and longitudinal dimension respectively, λ the longitudinal peak position and R the ratio between the two dimensions.

Sample	N	d_{TRAN} (nm)	d_{LONG} (nm)	λ_{LONG} (nm)	R
AuNRs3	40	19 ± 4.3	42 ± 6.8	618	2.2
AuNRs5	28	21 ± 4	44 ± 3.5	610	2.1
AuNRs8	65	23 ± 5	49 ± 8.6	626	2.1

This change proceeds during months as highlighted by the spectra in Figure 3.15:

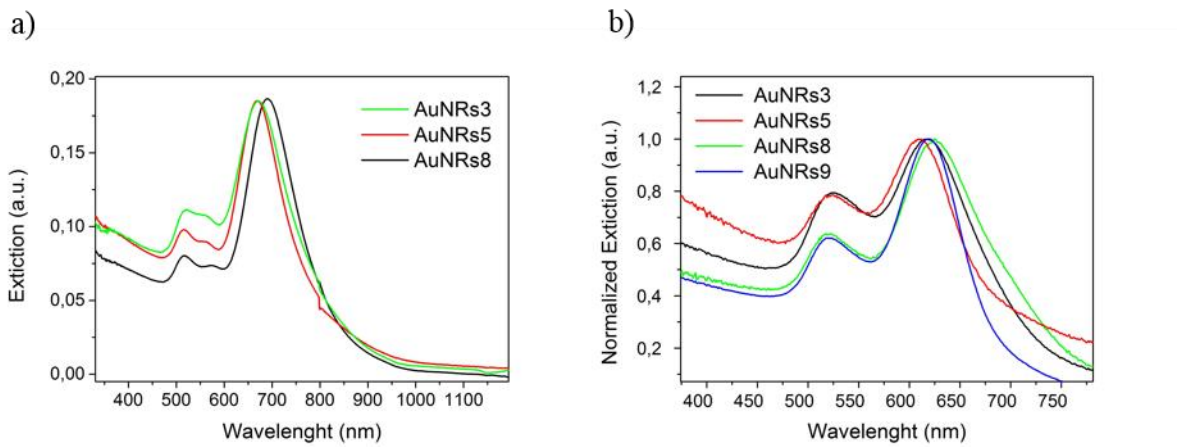

Figure 3.15: Comparison between different AuNRs synthesis with the same reagent ratio a) after 20 minutes reaction and b) after 4 months (black and red line), 3 months (green line) and 1 month (blue line)

We can analyze the spectra of distinct gold nanorods synthesis with the same reagent ratio and focus the attention on the resonance peak: both the longitudinal and the transversal are overlapped, respectively at 520 and 620 nm, but the extinction ratio are quite different. In particular the transversal plasmon peak is well overlapped between the two synthesis conducted 4 months ago (Figure 3.15 b) black and red line), while the other two (green and blue line) are different but comparable to each other, respectively at 3 and 1 month. This observation can suggest that nanorods change their shape during three months (decreasing ratio longitudinal/transversal peak I_L/I_T), and stop growing after the fourth. We take the I_L/I_T of different synthesis at various months in the attempt to compare the changes of the shape of nanorods (Figure 3.16 a-b).

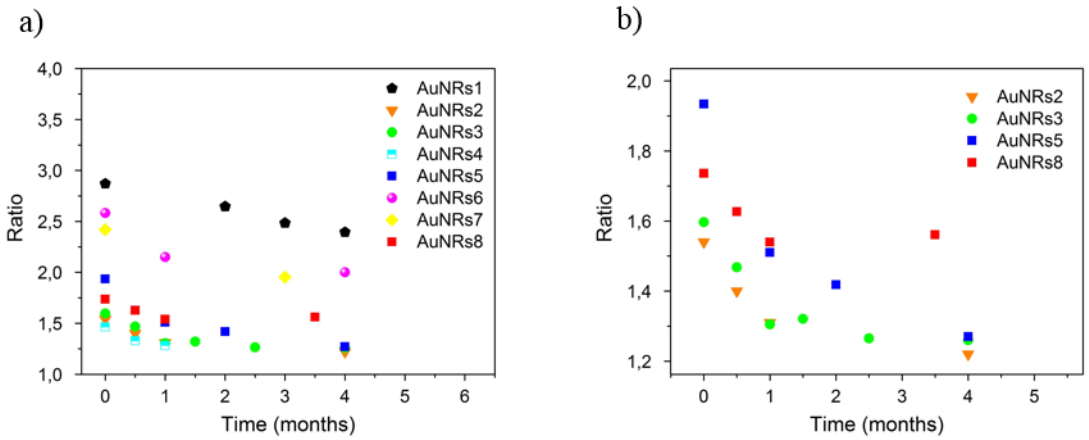

Figure 3.16: Ratio I_T/I_L of a) different nanorods measured up to six months, b) zoom with highlighted only AuNRs with same synthesis parameter

Synthesis of AuNRs2 and AuNRs3 are well reproduced (in Figure 3.16 with green and orange dots), but for example AuNRs5 and AuNRs8, synthesized in different days and so with different seed solutions, present a shifted ratio I_T/I_L.

The low reproducibility of the synthesis of gold nanorods, depending strongly on seed solution, is already know in literature[116]: the comparison of three different synthesis far-between a month present similar extinction at around 680 nm, while the transversal peak at 520 nm is quite different. Little differences in seeds solutions can lead to strong variation in final structure (Figure 3.17).

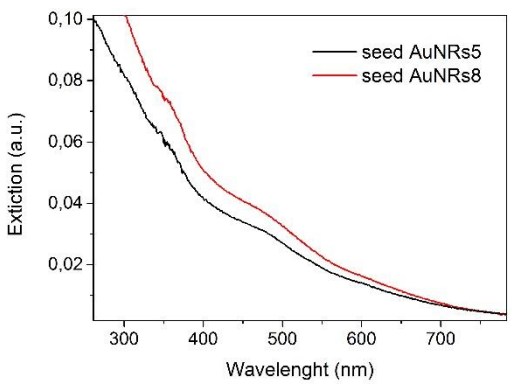

Figure 3.17: Comparison between different two seed solutions of AuNRs5 (black line) and AuNRs8 (red line)

The reshaping of gold nanorods has been followed by TEM analysis. To minimize the surface energy the structure drift from the cylindrical shape to a bone-shape configuration (Figure 3.18).

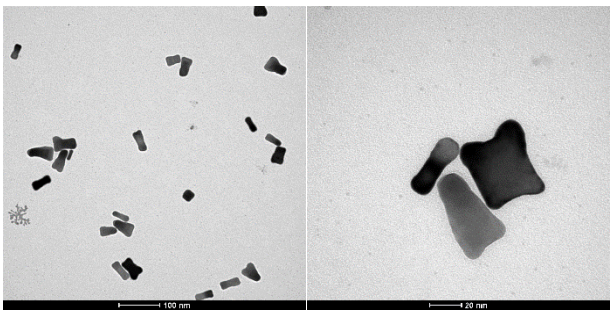

Figure 3.18: TEM images of bone-shape gold nanorods after 6 months after sysnthesis

It is possible to stabilize these nanostructures with PVP: as shown in Figure 3.19a that PVP stabilize the shape of nanorods, highlighted by the absorption spectra reproducibility.

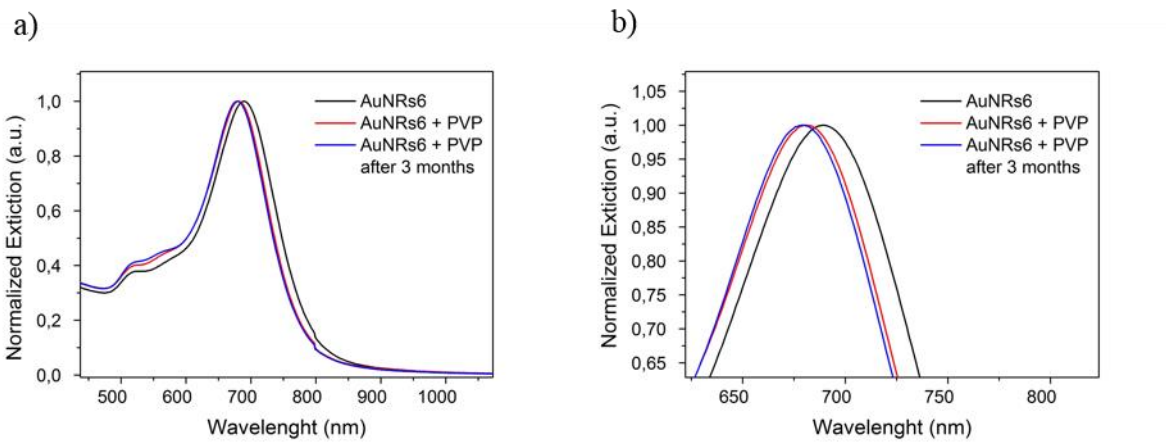

Figure 3.19: AuNRs6 a) after functionalization with PVP (red line) stable also after 3 months (blue line) and b) zoom on the transversal resonance peak

This functionalization can be useful for studies in solution, while present some problems in polycarbonate embedding, because PVP seems to induce segregation of nanostructures and preclude homogeneity in films. For this reason, PEG-2000 will be used for the solvent transfer for film production, described in paragraph 3.4.1.

3.3.3 Synthesis and characterization of gold nanoshells

In the present work gold nanoshells with a silica core and a gold shell were prepared following the multi-step process described by Pham et al.[117], to exploit the interesting plasmonic properties at different core and shell dimensions introduced by Halas et al. in 1998[118].

The synthesis of NSs (SiO2@Au) is realized in water following the procedure developed sketched in Figure 3.20.

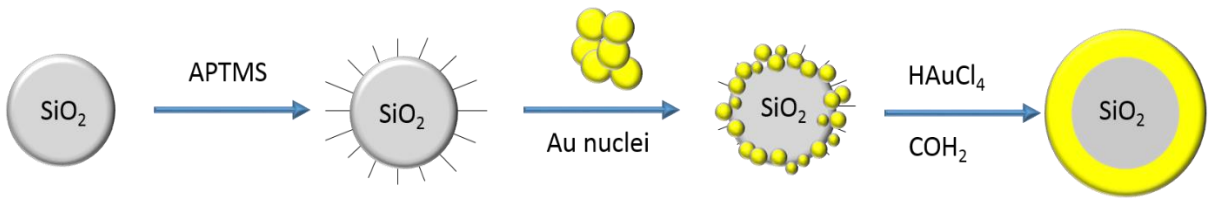

Figure 3.20: Simple scheme describing the synthesis of gold nanoshells

We first synthesized the silica cores via the Stöber method[119]. In this work the nanoshell samples are synthesized as follows: different amounts of ammonium hydroxide solution 30% are added (1.5-3 ml) to 50 ml of ethanol, dependent on the desired final silica particle dimension. Under vigorous stirring, 1.5 ml of TEOS are added slowly and dropwise, and the reaction is kept under stirring overnight, leading the formation of an opaque solution with a concentration of $8 \cdot 10^{11}$ NPs/mL.

We than functionalized silica NPs with 3-aminopropyltrimethoxysilane (APTMS), to allow the decoration of silica nanoparticles with gold nuclei. These molecules present amine groups outward as a new termination of the nanoparticle surface, act as a binding site for small colloidal gold particles (of about 2 nm diameter) prepared separately[119]. The covalent bonding between silica nanoparticles and APTMS is improved by heating the solution to 80°C. The solution (SiO_2@APTMS) is then purified by centrifugation and redispersed in ethanol.

The small gold nanoparticles for silica-APTMS decoration, are synthesized adding to 4.5 ml milli Q water 50 µl of a 1 M NaOH solution and subsequently 0.1 ml of a 68 mM THPC solution. The mixture is kept under vigorous stirring for 5 min and then a 0.2 ml of a 1% aqueos

$HAuCl_4$ solution is quickly added. The obtained NPs solution has a concentration of 4 x 10^{14} NPs/ml, calculated by estimating the NPs radius of 1 nm.

The gold/potassium carbonate (K_2CO_3) solution is prepared by dissolving 50 mg of K_2CO_3 in 100 ml H_2O Milli Q. After 10 min vigorous stirring 1.5 ml of a 1% $HAuCl_4$ aqueous solution is added to the salty water. The reaction is kept under stirring for 30 min, until the solution becomes colorless from bright yellow. The solution is aged at least for one night.

The final nanoshell synthesis is then performed by adding a different amount of SiO_2@APTMS@Au solution (100 µl) to 8 ml of aged $HAuCl_4$/ K_2CO_3 and finally 50 µl of formaldehyde. A different amount of SiO_2@APTMS@Au influences the final thickness of the gold shell. The NPs concentration depends on the silica core diameter. Nanoshells are stabilized by adding some PVP to the solution. By varying the ratio between the growth solution and the amount of gold-decorated silica particles, we could obtain different thickness for the Au shell covering the silica core surface. TEM analysis gives a diameter of D_{TEM}= (75 ± 18) nm, as shown in Figure 3.21.

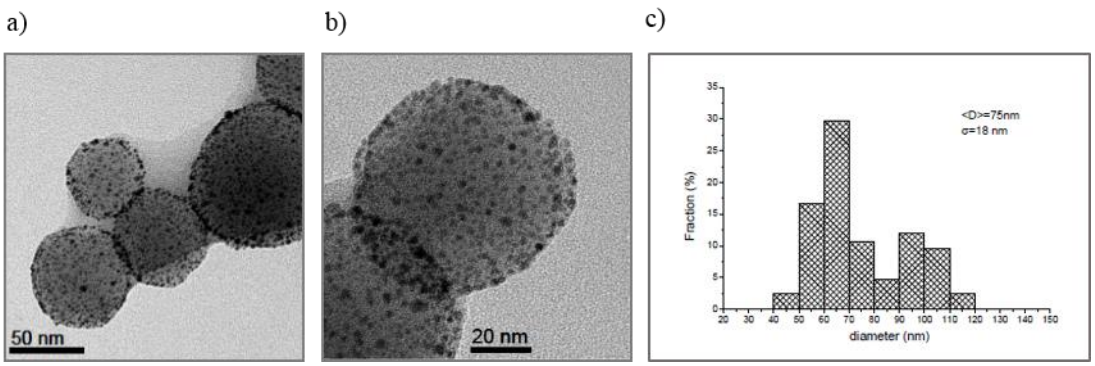

Figure 3.21: TEM analysis on SiO_2 (R1=38) cores: SiO_2@APTMS@Au (left and middle) and histogram of dimensional distribution (right).

The nuclei decoration seems to be homogeneous. The total diameter of the core-shell structure is 115± 17 nm, with a 20 nm shell thickness. We chose this core-shell ratio for our measures because we want a resonance peak around 650 nm (Figure 3.22).

The growth of a continuous, uniform Au layer on the dielectric core is the critical step in the synthesis of nanoshells[120]: the aqueous phase synthesis of gold nanoshells depends on the

reduction of tetrachloroauric acid in the presence of a reducing agent. Moreover both colloidal solutions and reductant solutions are known to change slowly over time, resulting in the growth of nanostructures with morphologies deviating from those achieved with freshly prepared solutions. All these elements make nanoshells synthesis a very sensitive process, which requires much care in operating and quite often leads to inhomogeneous and incomplete shell formation.

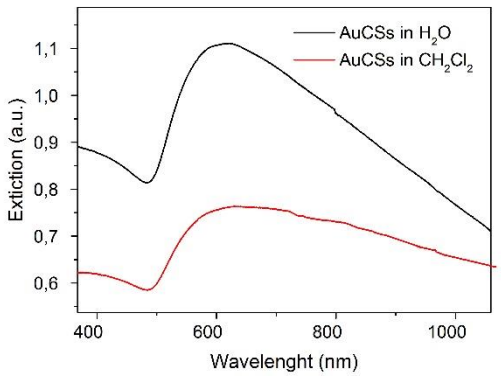

Figure 3.22: Extinction spectra of AuCSs as synthesized in H_2O (black line) and AuCSs in CH_2Cl_2 (red line)

Decrease of extinction show a lost nanoshells in the transfer and the change in the curve shape reveal a starting of aggregation. This solution will be functionalized with fulleropyrrolidine, as described in the the next paragraph.

3.3.4 Functionalization of gold nanospheres with fulleropyrroldine

Thiol functionalized fulleropyrrolidine dye was synthesized by Prof. Maggini group, at the Dept. of Chemical Science, of the University of Padova. We used it to functionalize NPs and NRs in dichloromethane.

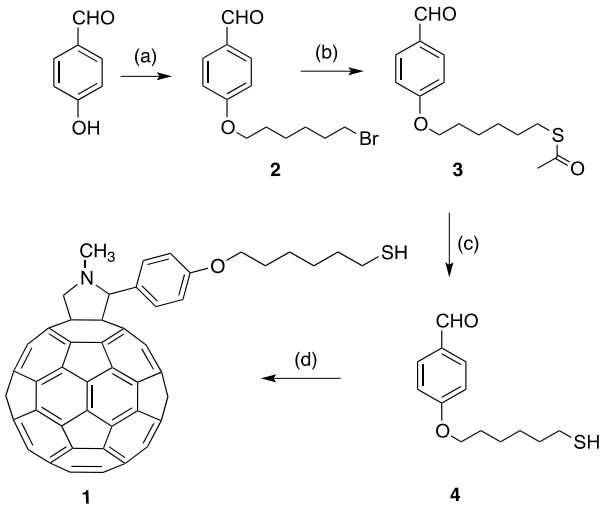

Scheme 1. Synthesis of thiolated fulleropyrrolidine (FP-SH) **1**. Reagents and conditions: (a) 4-hydroxybenzaldehyde, 1,6-dibromohexane, K_2CO_3, acetone, reflux 14h, N_2, 62%; (b) potassium thioacetate, acetone, room temperature, 16h, N_2, 87%; (c) THF, aq. NaOH, room temperature, 14h, N_2/dark, 48%; (d) N-methylglycine, [60]fullerene, chlorobenzene, reflux, 70 min, N_2/dark, 17%.

Stabilization and transfer of nanostructure in organic solvent have preceded the functionalization of gold nanoparticles with FP-SH.

The transfer of nanoparticles into organic solvents is generally made by thiols stabilization, for example with polyethylenglycol (PEG) or dodecanthiol[13,121,122]. We rather prefer using polyvinylpirrolidone (PVP): the displacement of PVP molecules by thiolated FP-SH results faster and more effective than the ligand replaces reaction[123]. We checked the development of the reaction using UV-Vis absorption: changing the nanostructure environment led to a shift of the resonance peak. After only 2 hours there are no more variation in absorption spectrum, and we proceed with the centrifugation for 10 minutes at 10000 rpm, adding an amount of acetone to promote the precipitation. Re-dispersion in CH_2Cl_2 has high yield, as shown in Figure 3.23, adding EtOH to promote further the dissolution. The comparison of the extinction value of the starting solution of AuNPs functionalized with PVP and the value of the supernatant extract from the centrifuged solution allow us to calculate the loss of nanoparticles, resulting in the order of 4-6%. Comparable results have been obtained with PEG-2000 functionalization, used for the film production.

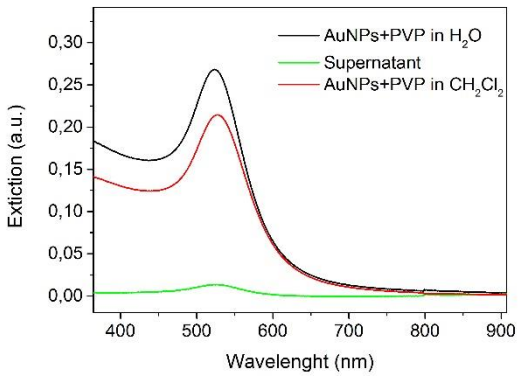

Figure 3.23: Absorption spectrum of AuNPs functionalized with PVP in H_2O (black line), CH_2Cl_2 (red line) and the supernatant after centrifugation (green line)

Gold nanoparticles in CH_2Cl_2 were than functionalized adding a solution of 0.5 mM of fulleropyrrolidine. The Surface Plasmon Resonance (SPR) peak is dependent upon the refractive index of the surrounding media, and its red-shift can be explained by the presence of FP-SH close to the AuNPs surfaces (Figure 3.24).

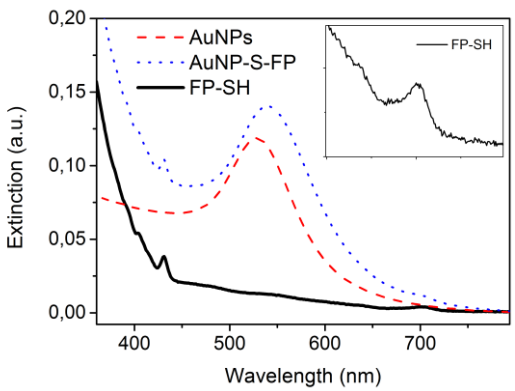

Figure 3.24: Absorbance of AuNPs (red dashed), AuNP-S-FP (black line) and FP-SH (blu dotted); the inset shows the zoom of FP-SH extinction curve

Extinction spectra of NPs colloids allow us the determine the particle size using a procedure reported in literature[111]: the diameter obtained was 14 nm.

Nanoparticles colloids were stabilized with a PVP 1 mM solution with a ratio 50:1, centrifuged and dissolved in CH_2Cl_2, adopting procedures described elsewhere[124].

Three samples were prepared, the first with AuNPs only, the second with both AuNPs and FP-SH, and the third one with only FP-SH, with concentrations of 6.4×10^{-9} molNP/L for gold nanoparticles and 0.45 mM for fulleropyrrolidine, to have around 10 time excess to ensure completion of ligation on nanoparticles.

Calculation of the complete coverage of a single nanoparticle with FP-SH molecules can be obtained with the areas ratio between the two systems:

$$\frac{N_{molec}}{NP} = \frac{A_{NP}}{A_{molec}} \tag{3.10}$$

where A_{NP} is the area of one nanoparticle (diameter of 14 nm) and A_{molec} is the area occupied by the fullerenthioled molecules (correspond to 0.785 nm^2), giving a value of around 1500 molecules for nanoparticle.

Samples are denoted AuNPs, AuNP-S-FP and FP-SH respectively. The AuNP-S-FP system is stable for more than 10 hours. After that period the unbound thiol molecules form disulfide crosslinks, changing the absorption spectrum.

After centrifugation an extinction spectrum of the supernatant has been made, confirming the excess of around 10 times unbounded molecules.

OL and z-scan measurements were conducted with solutions without further purification, to prevent nanoparticles aggregation and subsequent changes in the absorption profile.

In order to verify the functionalization of the AuNP surface with fulleropyrrolidine, the AuNP-S-FP solution was analyzed with two different techniques: Raman and Thermogravimetric Analysis (TGA).

A previous purification by centrifugation was carried out to separate the unbounded FP-SH molecules from the thiolated-nanoparticles. To confirm the removal of unbound molecules the supernatant of the second purification was also analyzed and did not show residual presence of FP-SH.

Information about the bonding of fulleropyrrolidine molecules to the gold surface could be given by a comparative Raman analysis of FP-SH powder and AuNP-S-FP purified and deposited on glass slide (Figure 3.25).

Both samples present peaks at 260-275 cm^{-1} and 486 cm^{-1}, assigned to intramolecular breathing modes[125], and 1434, 1470 and 1571 cm^{-1} modes, corresponding to CC stretching of the phenyl group of fullerene[126]. The presence of these bands in both spectra confirms the presence of the FP-SH molecules on the metal surface. Some spectra performed also at 647 nm irradiation wavelength show the quenching of the FP-SH fluorescence when AuNPs are present, confirming the proximity of the molecules to the gold surface.

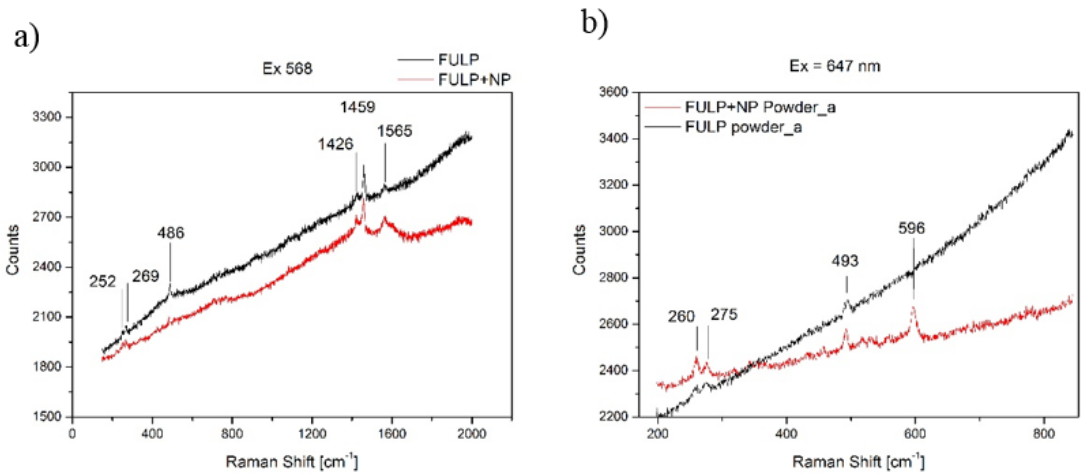

Figure 3.25: Raman spectra of FP-SH (black line) and AuNP-S-FP (red line) a) at 568 nm excitation wavelength and b) at 647 nm excitation wavelength

The thermal stability of the samples was verified by thermogravimetric analysis (Figure 3.26). Four samples were prepared by drop casting a dichloromethane solution of each material into platinum crucibles followed by thermal evaporation at 60 °C: PVP stabilized gold nanoparticles, FP-SH, centrifuged AuNP-S-FP and supernatant of the second centrifugation. The analysis of the supernatant verified the absence of FP-SH, confirming that all the FP-SH signals derive from the decomposition of bound molecules.

In the case of the gold nanoparticles functionalized with the fulleropyrrolidine moieties (AuNP-S-FP), the weight loss at 700 °C for gold nanoparticles is 47.4% which could be attributed to the thermal degradation of both the fulleropyrrolidine moieties and residual PVP. Since the value of the residue (52.6%) is similar to the value obtained for gold nanoparticles stabilized with PVP, it is arguable that the fulleropyrrolidine moieties replace the stabilizing PVP during the functionalization process. If, on the other hand, the fulleropyrrolidine moieties would have been physisorbed on the surface of PVP, the residue at 700 °C (i.e., the fractional amount of gold) would decrease with respect to the PVP stabilized nanoparticles.

Moreover, in addition to the peaks assigned to the degradation of PVP stabilizing the gold nanoparticles, the thermogram in Fig. 3.20 is characterized by a sharp degradation peaked between 408 and 440 °C which are compatible with the presence of pyrrolidine moieties on the sample. Under this assumption we may calculate the percentage in weight of each component: (a) 4.3% of fulleropyrrolidine; (b) 43.1% of PVP, and (c) 52.6% of gold.

These are typical shifts of the decomposition temperature for organic molecules in presence of metal nanoparticles[127,128]. A weight loss at 192 °C is attributed to the thermal retro-cycloaddition of the fulleropyrrolidine (retro-Prato reaction)[129,130].

This analysis allows us to calculate the number of molecules bound to the nanoparticle surface which is in the order of 10^3 molec/NP, with a coverage of 92%, consistent with other studies for the coverage of smaller nanoparticles in the way of molec/NP_{area}[131].

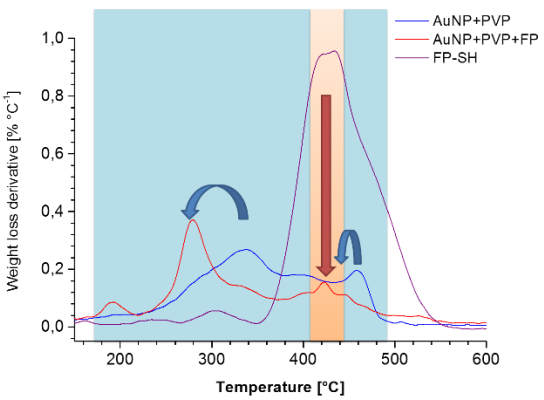

Figure 3.26: TGA spectra of AuNP-S-FP, bare AuNP and FP-SH.

In order to get optical limiting properties in a wider wavelength range, we have also studied gold nanoshells (AuNSs) whose plasmonic resonance can be tuned over all the visible and near infrared range depending on the ratio between Au shell thickness and SiO_2 core radius. This offers us the opportunity to protect the eyes against laser emitting in the red region. In order to obtain comparable limitation at high input intensity (see Chapter 4), the linear transmission of the nanoshell samples (Figure 3.27) is smaller than that of the AuNPs (Figure 3.19). This can be explained by a greater contribution of linear scattering to the extinction spectra of the nanoshells[88,110].

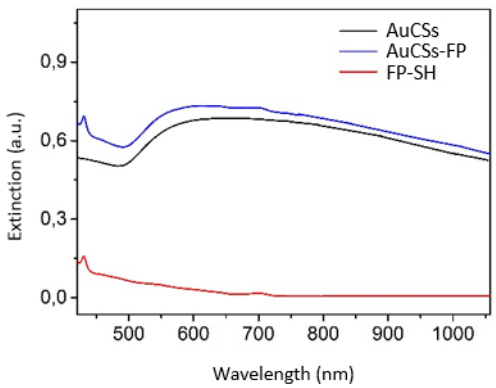

Figure 3.27: Extinction of AuCSs (black line), AuCSs-FP (blue line) and FP-SH (red line)

3.4 Film manufacturing

The inclusion of active materials, as gold nanostructures, in solid matrices is an essential step to realize optical devices: different matrices are used to this end, like polycarbonate [132], polyvinylpyrrolidone [133] and PMMA [134,135].

Interesting studies have also been conducted to embed nanostructures in polycarbonate. Larosa et al. [4] have studied a new nanostructured composite film, based on thiolated gold nanoparticles dispersed in polycarbonate, developed for applications as optical lenses. Many published papers [40,83,100,136] indicate AuNPs as promising active materials for the realization of solid state protection devices.

We have chosen polycarbonate (PC) because of its good optical properties, thermal stability and ease to process, that make it the favourite material for eyeglass production, from military to sport applications[137,138].

On the other side a useful matrix can be silk fibroin: some studies for the functionalization of silk matrix with nanostructures have been tried in the past[139–141], but it is in this last two years that silk fibroin coupled with gold nanoparticles has strongly emerged. Different applications borne out the great interest of this system: tissue engineering, with printable bio-electronic devices[142] and cell-biomaterial interactions study[143], thermoresponsive polymer[51], infection treatment[144] thanks to its good biocompatibility[41], etc. Its hydrosolubility after the extraction allow us to overcome the transfer of nanoparticles in organic solvent, while the conformation changes after thermal treatment stabilize the hydrophobic phase, improving mechanical properties.

3.4.1 Polycarbonate matrix

Polymer in form of pellets have been used without pre-thermal treatment and have been dissolved in dichloromethane by sonication and then mixed with solutions with different dyes and concentrations. The solvent was evaporated by drying under vacuum at 50 °C for 2 h in a Petri dish. When the procedure has been optimized, we proceeded with the functionalization with precise amount of nanostructures. We first tried different dyes to improve the embedding method, as phtalocyanine, spiropyran and fulleropyrrolidine. Then we started to embed different nanostructures, in particular AuNPs.

We obtain film with AuNPs at different concentration, but we used only two of them for the OL and z-scan analysis (see Chapter 4) namely those with PC weight ratios: 2.5 : 200 (AuNPs1), and 6 : 200 (AuNPs2) and a final thickness of 109 μm and 103 μm, respectively, shown in Figure 3.28b. Using a NPs diameter of 14 nm, the final concentrations have been calculated to be 1.14×10^{-7} mol_{NP}/dm^3 for AuNPs1 sample and 2.74×10^{-7} mol_{NP}/dm^3 for AuNPs2 sample.

Upon inclusion of NPs in PC (Figure 3.28 a-b) linear extinction properties are well preserved, confirming a high degree of NPs dispersion without aggregation. The observed peak shifts is

well explained by the variation of the dielectric constant, which is known to affect the plasmon resonance frequency [46,145].

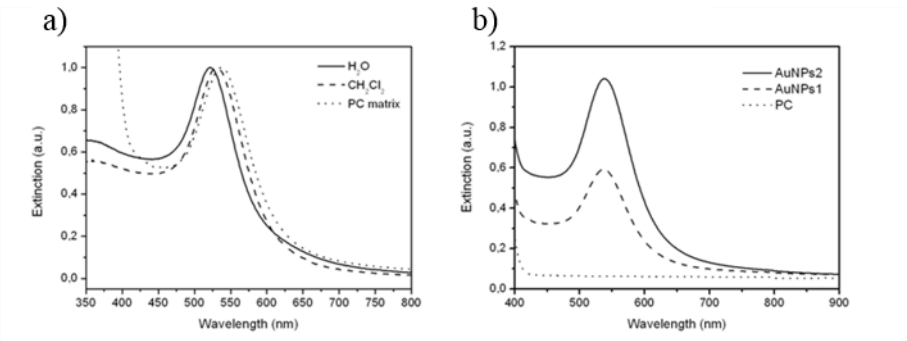

Figure 3.28: Normalized UV-Visible extinction spectra of a) AuNPs in different solvents and matrix and b) Samples of AuNPs in polycarbonate films, with different concentrations, and pure polycarbonate film

In order to obtain an eye protection device, two relevant parameters to consider are the *photopic* and the *scotopic* transmittance, the eye visibility in light and dark condition, generally higher than 20%.

To calculate the luminosity of a filter, simply calculate the area under the transmission spectrum curve weighted by the Photopic Curve $V(\lambda)$, and divide by (normalize by) the area under the photopic curve. The photopic and scotopic curves account for the eye sensitivy of human eyes to different visible wavelengths. Photopic refers to vision in daylight by "cones" as opposed to scotopic which refers to vision in dim light by the more sensitive but less color-discriminating "rods". Mathematically, the luminosity L is given:

$$L = \frac{\int_0^\infty I(\lambda)T(\lambda)V(\lambda)d\lambda}{\int_0^\infty I(\lambda)V(\lambda)d\lambda} \tag{3.11}$$

$T(\lambda)$ is the transmission spectrum of the filter ($0 \leq T \leq 1$), $V(\lambda)$ the photopic curve of the human eye, $I(\lambda)$ is the spectrum of the illuminant[146].

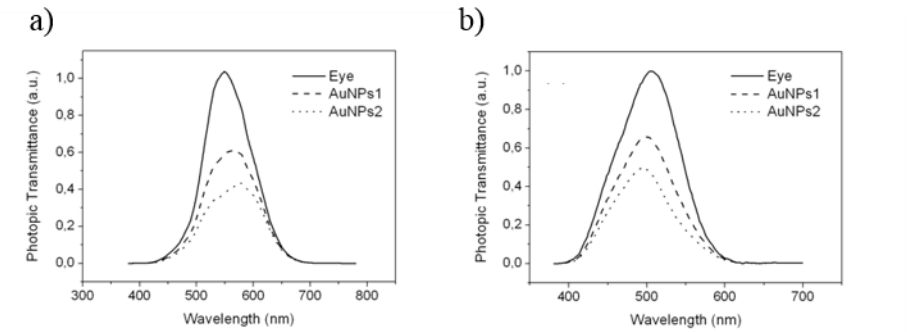

Figure 3.29: (a) Photopic Trasmittance of AuNPs1 is 65.2%, AuNPs2 is 47.3%, and (b) Scotopic Transmittance of AuNPs1 is 66.3% and AuNPs2 is 49.2%.

Our samples present a photopic transmittance of 65.2% for AuNPs1 and 47.3% for AuNPs2; in dark conditions the transmittance is lightly higher, 66.3 and 49.2 respectively (Figure 3.29).

The same procedure has been used to transfer AuNRs in CH_2Cl_2 and for the embedding in polycarbonate matrix. Firstly we conducted a study on the stabilization of AuNRs with various concentration of two different capping agents, PEG and PVP: AuNRs capped with PVP result not stable and aggregates after centrifugation and redispesion, while PEG seems to be efficacy at the lower concentration tried (200uL/mL of a solution with 2 mg/mL). Results reported in Figure 3.30 show the high stability of AuNRs functionalized with PEG-2000 (Samples 1-2-3) and the aggregation of samples functionalized with PVP (Samples 4-5).

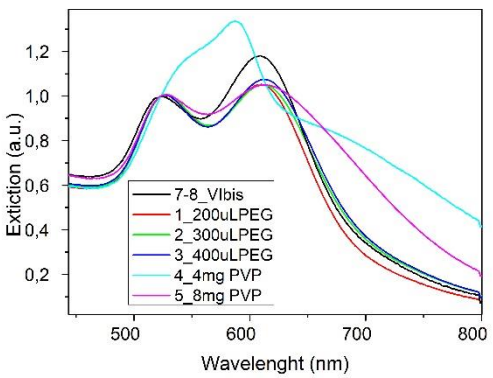

Figure 3.30: Extinction spectra of AuNRs with different capping agents normalized at 520 nm

A preliminary study of properties of AuNRs embedded in polycarbonate matrix are reported below: the functionalization only shift the transversal resonance peak as expected and also the film formation maintain the plasmon resonances and ratio between longitudinal and transversal peaks.

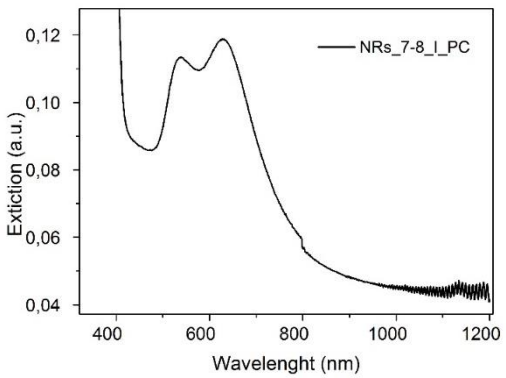

Figure 3.31: Extinction spectrum of AuNRs embedded in PC matrix

In the inset of Figure 3.31 the film appear transparent and homogeneous and also the UV-Vis spectrum do not present aggregates, compared with the starting AuNRs in CH_2Cl_2 solution.

3.4.2 Silk fibroin matrix

Silk fibroin has been provided by Prof. Zamboni group, at the Insitute for the organic synthesis and photoreactivity, of the CNR of Bologna. The extraction and purification of this fiber follow the procedure describe in literature[147].

There are at least four different types of secondary structures in silk, depending on the physical state of silk: random coil, α-helix, silk I, and silk II. Silk fibroin in solution consists of a combination of random-coil, silk I and α-helical conformations, that represent the non-crystalline region of the protein, with only a small percentage of β-sheet silk II. On the contrary, the decreasing of water content in the solid form promote interaction through hydrophobic sequences in the protein, generating crystalline domains[148].

The hydrosolubility of silk fibroin allowed us to eliminate the step of the functionalization and solvent transfer, reducing the time of production and the loss of nanoparticles.
Homogenizing AuNPs and silk fibroin solutions does not require sonication, as for polycarbonate, because of inter-diffusion with gentle mixing. The stability of silk in presence of nanoparticles is anticipated by the z-potential value (-40).
With our film production technique, we have been able to obtain good optical quality film (Figure 3.32) also for undoped silk fibroin.

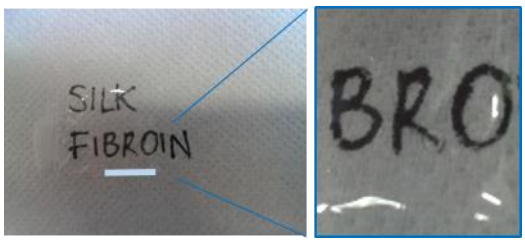

Figure 3.32: Silk fibroin film

We have tried different substrate in order to improve the optical quality of the film. Simple drop casting produce high rough surface (Figure 3.33).

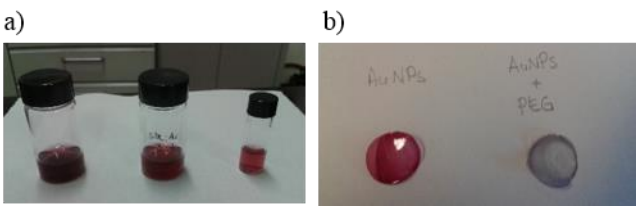

Figure 3.33: Silk fibroin and AuNPs a) solution and b) films

We implemented the technique used for polycarbonate casting through a PDMS petri dish obtained casting PDMS on a silicon surface (Figure 3.34 a). The film casted show a high homogeneity and transparency with no image distortion (Figure 3.34 b).

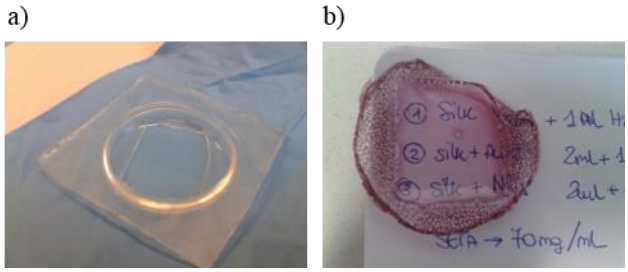

Figure 3.34: a) PDMS petri dish with optical quality bottom obtained with silicon surface master, b) AuNPs-SF film obtained casted in PDMS petri dish

AuNPs common stabilizers, as PEG or PVP, seem to destabilize silk, causing the formation of fibroin domains and aggregation of gold nanoparticles. We do not achieve the embedding of AuNRs in silk matrix because also CTAB destabilizes the solution and induces the formation of a gel.

Absorption spectra of films show that the adopted procedures are successful in producing good nanoparticles embedding without aggregation (Figure 3.35 a-b).

The ratio between silk fibroin and AuNPs solutions together with the deposition substrate used for the casting process are resumed in Table 3.1.

Table 3.1: Experimental details of silk matrix film manufacturing

Sample	**Substrate**	**Ratio (Au:SF)**	**Thickness (um)**	**Extinction (514 nm)**
SF1	Petri PDMS	-	80	-
SF2	Becher	-	120	-
Au-SF1	PDMS	2:1	125	0.25
Au-SF2	Becher	1:1	114	0.33
Au-SF4	Petri glass	1:1	102	0.35
Au-SF7	Petri PDMS	2:1	85	0.19

Good optical quality has been reached also for simple silk fibroin matrix: this goal can be useful also for different applications[149].

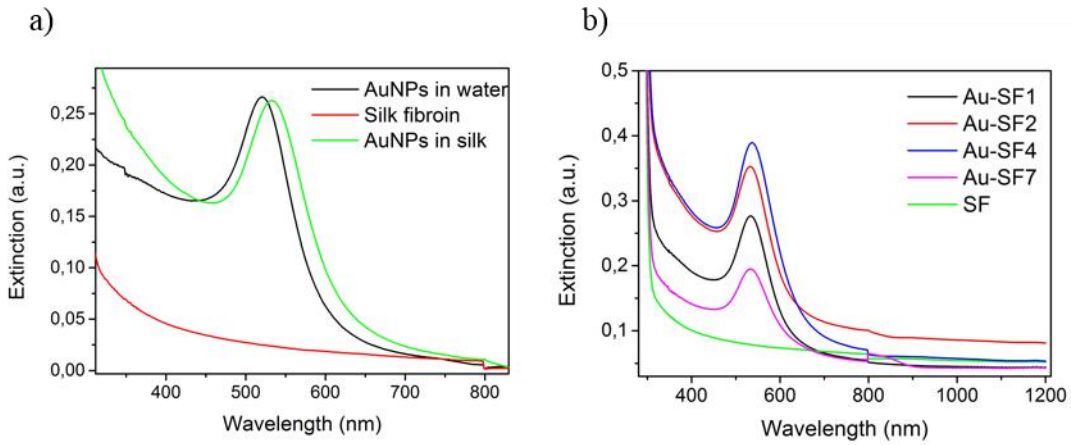

Figure 3.35: Extinction spectra of a) AuNPs transfer in silk fibroin and b) AuNPs-SF films obtained with different casting methods

Thermal analysis of the matrix, doped and undoped, show differences in conformational organization of the fibers due to the production technique (Figure 3.36). This behavior of silk fibroin has been studied varying the deposition temperature[150], revealing a maximum in B-sheet formation at between 50 and 60 °C. TGA analysis on our films confirm this preferential configuration. The presence of nanoparticles induce in the matrix an increase in thermal stability, as shown in the Figure 3.36 a, higher for the deposition over plastic than over glass.

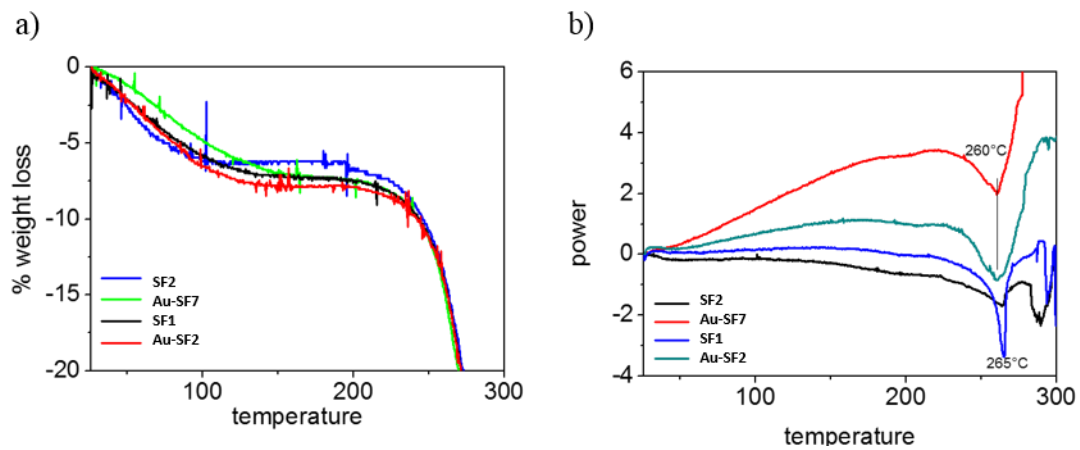

Figure 3.36: TGA and DSC analysis of silk and composite silk-AuNPs films obtained with different casting support

Chapter 4

4 NONLINEAR OPTICAL MEASUREMENTS

In this chapter, the nonlinear (NL) optical properties of gold nanospheres, nanorods and nanoshells bares, functionalized and embedded in different matrices are described. It starts with the description of laser systems (paragraph 4.1) and the nonlinear characterization techniques (paragraphs 4.2-3-4-5): z-scan technique is used to characterize nonlinear absorption and refraction coefficients and Optical limiting (OL) to characterize the thresholds of nonlinear effect. Temporal responses at different input powers have been collected and analyzed.

4.1 Laser system

Z-scan and Optical limiting experiments are performed with Innova 70, a mixed Ar^+/Kr^+ cw laser system delivering a set of discrete emission lines within the range 450-647 nm. The output power of the laser system has the following features: wavelength of 488 nm at about 400mW, 514 nm at 600mW and 647 nm at 200mW. During the experimental measurements, the beam properties – time duration, power – were controlled through two photodiodes calibrated and connected to an oscilloscope, and interfaced to the computer with a LabView program, while spatial shape of the beam is measured with a CCD camera.

The set-up used for Z-scan, Optical limiting and temporal response measurements is shown in Figure 4.1: F are the filters used to change the input power, BS is the beam splitter to collect a part of the incoming intensity and get a reference signal, L1 and L2 are the focalizing lenses, D the diaphragm, P1 and P2 the photodiodes and S the sample (free standing film or solution in 1mm or 1cm cuvette).

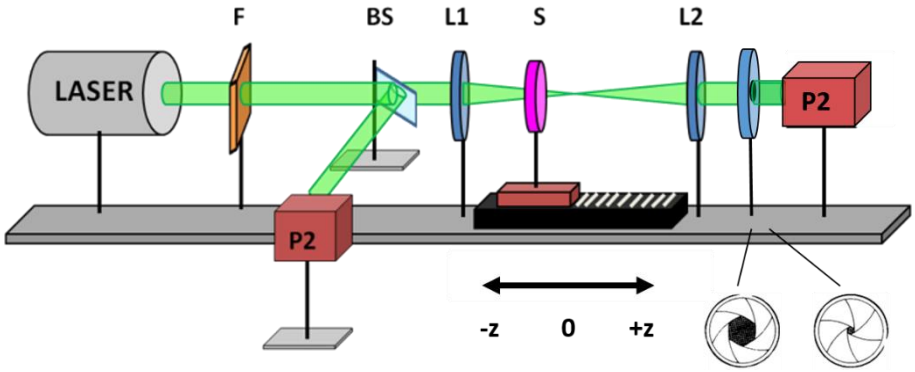

Figure 4.1: Z-scan and optical limiting setup

4.2 Z-scan measurements

The z-scan is a technique[151] that allow to measure characteristic constants associated at NL optical phenomena (i.e. NL refractive index and NL absorption coefficient) simply measuring variations in transmittance. This is possible because the NL optical effects depend on the irradiance of the incident beam: moving the sample along the z direction of propagation of the focalized beam, the cross-section area decreases, hence the irradiance (power per unit area) increases.

In Figure 4.1 is represented the setup configuration: a laser beam is focused by a lens (L1) onto a sample mounted on a translation stage and reaches the detector: the stage is moved around the focal region along the beam propagation direction (Z axis).

Away from the focus, the beam irradiance is low, nonlinear phenomena do not occur and the transmittance remains constant. As the sample get close to the focus, the beam irradiance increases, leading to NL phenomena.

When all the transmitted light passed through the sample is collected (open-aperture configuration) the transmittance decreases and this can be due to different processes, i.e. multiphoton absorption, reverse saturable absorption etc. In the closed-aperture configuration, a diaphragm is put after the sample, before the photodetector, and allow us to measure changes in spatial intensity distribution of the light beam due to changes in nonlinear refractive index of the sample.

Considering the case of closed-aperture, z-scan measurements are used to determine the nonlinear refractive index (n_2). For a material with negative n_2, as the sample approaches the focus the irradiance increases and the sample acts as a defocusing lens. In this way the beam is

narrowed increasing the intensity that reach the detector (Figure 4.2a). On the other hand, when the sample passes the focal plane (Figure 4.2b) the beam diverges and the transmittance collected decreases.

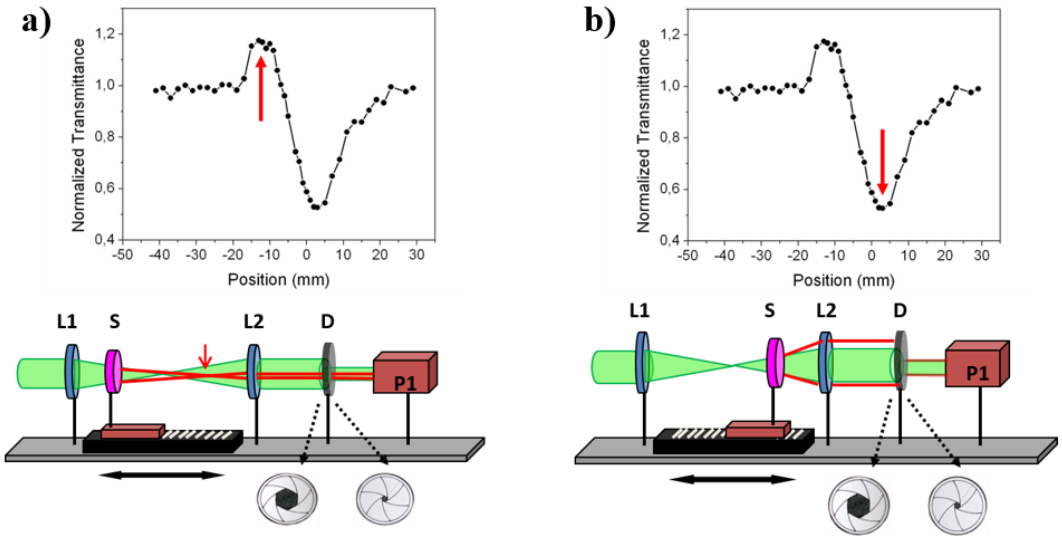

Figure 4.2: Example of closed-aperture z-scan measurement of a self-defocusing mechanism indicated by red arrows a) pre-focal position and b) post-focal position

Assuming a TEM_{00} Gaussian beam of beam waist radius w_0 traveling in the +z direction: if the sample length (L) is small enough that changes in the beam diameter within the sample due to either diffraction or nonlinear refraction can be neglected, the medium is regarded as "thin," in which case the self-refraction process is referred to as "external self-action". For linear diffraction, this implies that $L << z_0$, while for non-linear refraction, $L << z_0$, where $z_0 = \frac{\pi\omega_0{}^2}{\lambda}$ is the diffraction length of the beam and ω_0 is the beam waist. For nonlinear refraction process $L<<z_0/\Delta\varphi_0$, where $\Delta\varphi_0$ is the maximum phase shift induced, that must be small to satisfied the condition. Such an assumption simplifies the problem considerably, and the amplitude and phase of the electric field as a function of z' are now governed in the slowly varying envelope approximation (SVEA) by a pair of simple equations:

$$\frac{d\Delta\varphi}{dz'} = k\Delta n(I) \tag{4.1}$$

$$\frac{dI}{dz'} = -\alpha(I)I \tag{4.2}$$

where z' is the propagation depth in the sample and a (I), in general, includes linear and nonlinear absorption terms. $\Delta n(I)$ is the nonlinear refractive index variation and $\alpha(I)$ is the nonlinear absorption coefficient. In the case of a cubic nonlinearity and negligible nonlinear absorption, Eq. (4.1) and (4.2) are solved to give the phase shift at the exit surface of the sample, which follows the radial variation of the incident irradiance at a given position of the sample z. Thus:

$$\Delta\varphi(z,r,t) = \frac{\Delta\varphi(t)}{1+\frac{z^2}{{z_0}^2}} e^{\frac{-2r^2}{\omega^2(z)}} \tag{4.3}$$

$$\omega^2(z) = {\omega_0}^2\left(1+\frac{z}{z_0}\right) \tag{4.4}$$

Where $\omega^2(z)$ is the beam radius and

$$\Delta\varphi(t) = k\Delta n_2(t) L_{eff} \tag{4.5}$$

with $k = \frac{2\pi}{\lambda}$ is the wave vector and λ the laser wavelength, $L_{eff} = \frac{(1-e^{-\alpha L})}{\alpha}$. The refractive index variation $\Delta n_0 = n_2 \mathrm{I}_0(\mathrm{t})$ is defined through n_2, the nonlinear refractive index and I_0 is the irradiance at the focus.

In the limit of small non-linear phase change $|\Delta\varphi_0| \ll 1$ and in the far field condition $d \gg z_0$ the normalized transmittance read by the detector can be written as:

$$T(z,\Delta\varphi_0) = 1 - \frac{4\Delta\varphi_0 x}{(x^2+9)(x^2-1)} \tag{4.6}$$

where $x = \frac{z}{z0}$ represent the ratio between the position and the Rayleigh range and so, it is possible to obtain the nonlinear refractive index n_2.

With larger phase distortions ($|\Delta\varphi_0| > 1$), for the corresponding sign of non-linearity ($\pm\Delta\varphi_0$) the peak-valley separation remains nearly constant, given by:

$$\Delta z_{p-v} = 1.7\, z_0 \tag{4.7}$$

For all aperture sizes (S) of the iris positioned before the photodiode (Figure 4.1), the variation of ΔT_{p-v} is found to be almost linearly dependent on $|\Delta\varphi_0|$. For small phase distortion and small aperture ($S \cong 0$):

$$\Delta T_{p-v} = 0.406|\Delta\varphi_0| \tag{4.8}$$

Numerical calculations show that this relation is accurate within 0.5 percent for $|\Delta\varphi_0| < \pi$. For larger apertures, the linear coefficient 0.406 decreases such that with S = 0.5, it becomes 0.34, and at S = 0.7, it reduces to 0.29. Based on a numerical fitting, the following relationship can be used to include such variations within a +2% accuracy:

$$\Delta T_{p-v} = 0.406(1-S)^{0.25} \tag{4.9}$$

The model equation that we have used include the parameter S (aperture), obtained as the ratio between the linear absorption without and with diaphragm [151].

$$\Delta T_{pv} = 0.290 \cdot (1-S)^{0.25}\ \Delta\Phi_0 \tag{4.10}$$

$$\Delta\Phi_0 = \frac{2\pi L_{eff} n_2 I_0}{\lambda} \tag{4.11}$$

The on-axis nonlinear phase-shift ($\Delta\Phi_0$) can be experimentally measured from the peak-to-valley transmittance (ΔT_{pv}).

If the detector (removing the diaphragm) collects the total transmitted irradiance it is possible to determine also the nonlinear absorption coefficient. In the open-aperture configuration the normalized transmittance become:

$$T(z) = \frac{1}{\sqrt{\pi} q_0(z)} \int_{-\infty}^{+\infty} \ln\left[1 + q_0(z) e^{-\tau^2}\right] d\tau \tag{4.12}$$

$$q(z,t) = \frac{\beta I_0 L_{eff}}{\left(1+\frac{z^2}{{z_0}^2}\right)} \tag{4.13}$$

where β is the nonlinear absorption coefficient, correspond to TPA coefficient for ultrafast processes or effective coefficient for different processes, including thermal (see Paragraph 4.4). Under the condition $|q_0| < 1$ the resulting formula is:

$$T(z, S=1) = \sum_{m=0}^{\infty} \frac{[-q_0(z,0)]^m}{(m+1)^{\frac{3}{2}}} \tag{4.14}$$

where $|q_0(z,t)| < 1$ for the validity of the model, β is the effective nonlinear absorption coefficient, z_0 is the Rayleigh range of the focusing optics, I_0 the intensity at the focus, $L_{eff} = \frac{(1-e^{-\alpha L})}{\alpha}$ the effective length of the sample and α is the linear absorption coefficient.

Guo et al.[152] described a simplified second Z-scan technique for cases where nonlinear refraction is accompanied by strong nonlinear absorption and for extracting the nonlinear refraction, separately evaluating the nonlinear refraction and the nonlinear absorption by performing straightforward measurement with the aperture removed. In the same condition of Gaussian beam, thin film and low irradiance limit $\Delta\varphi_0 < 1$, the normalized transmittance can be written as[153,154]:

$$T = 1 + \frac{(1-S)^{\mu} sin\xi}{S(1+x^2)}\Delta\varphi_0 - \frac{1-(1-S)^{\mu} sin\xi}{S(1+x^2)}\Delta\psi_0 \quad (4.15)$$

$$\mu = \frac{2(x^2+3)}{x^2+9} \quad (4.16)$$

$$\xi = -\frac{4xln(1-S)}{x^2+9} \quad (4.17)$$

$$\Delta\varphi_0 = k\gamma I_0 L_{eff} \quad (4.18)$$

$$\Delta\psi_0 = \frac{\beta I_0 L_{eff}}{2} \quad (4.149$$

Defining the $\Delta\psi_0$=0 the theoretical normalized transmittance from the contribution of the pure nonlinear refraction can be obtained from Equation. 4.20:

$$T_{refr} = 1 + \frac{(1-S)^{\mu} sin\xi}{S(1+x^2)}\Delta\varphi_0 \quad (4.20)$$

An interesting contribution to z-scan measurements using cw laser has been given by Tian et al.[155].

They gave an indication that can be employed to distinguish thermally induced nonlinearities from others by varying the beam waist radius and measuring the peak-valley distance. If only thermal nonlinear refraction is present, $\alpha(I)$ can be consider constant, we can write:

$$\Delta n = \frac{dn}{dT}\Delta T \approx \frac{dn}{dT}\frac{I\tau\alpha}{\rho C} \quad (4.21)$$

where $\frac{1}{\tau} = \frac{1}{t} + \frac{1}{t_c}$ with t time exposed to the laser and $t_c = \frac{\omega^2\rho C}{4K}$ is the thermal relaxation time, K is the thermal conductivity, ρ is the density and C is the specific heat. Thus:

$$\Delta n = \frac{dn}{dT}\frac{I\omega^2\alpha}{4K} \quad (4.22)$$

The solution obtained in Equation. 4.5 changes substituting the irradiance with the power using the relation $P_{in} = \frac{I\omega^2\pi}{2}$:

$$\Delta\varphi_0 = \frac{dn}{dT}\frac{P_{in}L_{eff}\alpha}{\lambda K} \tag{4.23}$$

By spatially integrating the electric field to the aperture radius, we can obtain transmitted power and then the normalized transmittance through the aperture results:

$$T(z) = \frac{P_T}{P_{in}Se^{-\alpha L}} \tag{4.24}$$

when the linear transmittance is $S \ll 1$ the calculate:

$$\Delta T_{p-v} \approx 1.35|\Delta\varphi_0|, \qquad |\Delta\varphi_0| \ll \pi \tag{4.25}$$

$$\Delta z_{p-v} \approx 5.9 z_0 \tag{4.26}$$

In this analysis $\Delta\varphi_0$ is proportional to the power, not to the intensity, for thermally induced nonlinearity for cw illumination.

NL optical properties of noble metal NPs in solution and embedded in a polymer matrix have been investigated by the open aperture z-scan technique because of their large third-order susceptibility[20,38,93,156–159]. In general, when excited with ultrafast pulses near to the Surface Plasmon Resonance (SPR) band, metal NPs behave as a saturable absorbers owing to the bleaching of the ground-state plasmon band. In some cases, at higher pump intensity, gold nanospheres and nanorods[160], change their behavior from saturable absorber to reverse saturable absorber (i.e., absorption increases at high input intensities) due to free carrier absorption.

Also using cw laser excitation the behavior of gold nanostructures give negative nonlinear refraction process, leading to a diminishing of transmittance after a certain threshold[8,39,100,133]. Nanospheres (AuNPs) nanorods (AuNRs) and nanoshells (AuNSs) are typically characterized by z-scan technique, the majority in solution, but for gold nanoparticles also in film.

Metal nanostructures have been excited by 488, 514 and 647 nm cw laser excitation, depending on the SPR band wavelength. By fitting the experimental results, it is possible to obtain effective NL absorption coefficients; the data obtained are strongly dependent on the experimental conditions as we will discuss in this chapter. Very different nonlinearity values are published for different dyes[134,161–163] and metal nanostructures[39,40,83,136] from 10^{-1}–10^{-3}

cmW^{-1} for effective nonlinear absorption coefficient, to 10^{-5}–10^{-8} cm^2W^{-1} for nonlinear refractive coefficient. For this reason, comparing NL absorption coefficient for different nanostructures should be difficult when the experimental condition are not the same.

4.3 Optical power limiting

The optical power limiting technique, already described in Chapter 1, with a simple geometry and instrumentation allow determining the transmittance decrease after irradiation with different input intensities. The setup is the same used for z-scan measurements, with the only difference of changing input irradiance: instead of varying the beam area on the sample moving the stage, we maintain constant the position varying the input power with optical density filter (Figure 4.3).

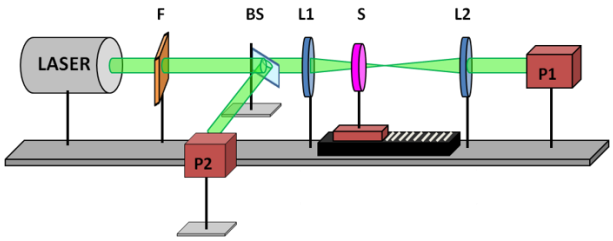

Figure 4.3: Optical limiting measurements setup

The sample is placed in different positions, depending on the type of measure: for example measurements in polycarbonate matrix are conducted in pre- and post-focal positions. Each position and consequent irradiance are reported in the correspondent paragraph.

4.4 Temporal responses

We have discuss in Chapter 1 the importance of the exposure time also in presence of cw laser, and specific characteristic of a protection device.

Concerning the damage threshold for optical sensors, also low power cw lasers, with output powers in the 1–5 mW range, can damage the human eye if directly exposed for times less than 0.25 s. Therefore, the maximum permissible exposure by a laser is calculated to be at an irradiance of ~2.5 mW cm^{-2}, corresponding to a fluence of 0.63 mJ cm^{-2} for a safe exposure of 0.25 s [164,165]. In other words, a good optical limiter for cw lasers should activate in a short time, less than 0.25 s and present output irradiance lower than 2.5 mW cm^{-2}.

For these reasons, the temporal response analysis represents an instrument to determine the total fluence that reaches the sensor under defined geometrical condition. We have chosen an exposure interval of 300 ms for the characterization of our systems to overestimate the energy in the sensor.

We analyzed the dynamics of the nonlinear transmittance responses of colloidal nanoparticles samples (Figure 4.4) using a model for the time evolution of the thermal lens effect under illumination with varying input intensities [166]. The time dependent expression for the far-field on-axis transmittance can be written as a function of the sample position:

$$T_N{}^{TLM}(z,t) = \left\{1 + \left[\frac{\theta}{1+(1+x^2)\frac{t_c}{2t}}\right]\frac{2x}{1+x^2}\right\}^{-1} \tag{4.27}$$

where

$$\theta = \frac{\alpha_0 P d}{\lambda k}\frac{dn}{dT} \tag{4.28}$$

$$t_c = \frac{\omega^2}{4D} \tag{4.29}$$

with θ is the phase-shift, α_0 is the absorption coefficient, P is the input power, d is the thickness of the sample, λ is the irradiation wavelength, k is the thermal conductivity and dn/dT is the thermo-optic coefficient, t_c is the diffusion time, w the beam diameter and D the diffusion coefficient.

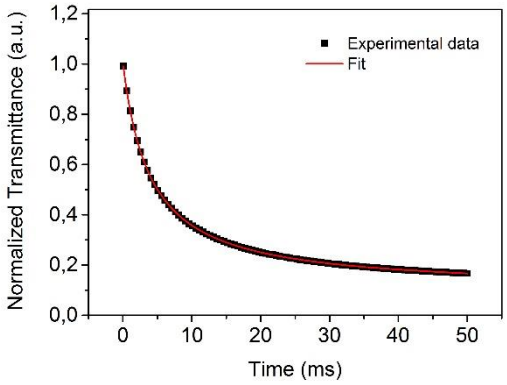

Figure 4.4: Example of trasnmittance decrease caused by a thermal lens process in 50 ms

4.5 Photoacoustic measurements

Photoacoustic spectroscopy is part of a class of photothermal techniques, in which an impinging light beam is absorbed and alters the thermal state of the sample. This process was first invented by Bell, Tyndall and Rontgen in 1880, and in 1973, Parker[167] noticed a photoacoustic signal apparently coming from the windows of the sample cell, which should have been transparent to the incoming radiation. Gordon et al.[67] first by means of this technique measure very low absorption in liquids. The commonly accepted mechanism for the photoacoustic effect is called RG theory, after its developers Rosencwaig and Gersho[168]. The basic theory behind photoacoustic detection is quite simple. Light absorbed by a sample will excite a fraction of the ground-state molecular population into higher energy levels. These excited states will subsequently relax through a combination of radiative and nonradiative pathways. The nonradiative component will ultimately generate heat in the localized region of the excitation light beam and generate a pressure wave that propagates away from the source. The pressure wave is then detected with a suitable sensor such as a microphone used for a gaseous sample.

In the present work, photoacoustic excitation profiles are performed on different gold nanospheres and nanorods in water solution (Figure 4.5). Measurements are performed with a Quanta System Nd:Yag laser-pumped dye laser at 532 nm (10 ns pulse duration, 10Hz repetition rate). The incident laser energy was measured with a pyroelectric head energy meter before each measurement, put in front of the sample cuvette (1 cm length).

Photoacoustic signals were detected with a 1 MHz bandpass Panametrics V103-RM piezoelectric transducer clamped to a standard quartz cuvette for absorption spectroscopy. The signals were amplified with a Panametrics 5660 B amplifier and averaged with a Tektronix TDS-3054B digitizing oscilloscope. The minimum number of signals was 512 for each average. The sample temperature was kept constant within 0.1°C with a Lauda Eco RE 415 cryostat and monitored by a thermocouple placed inside the cuvette. The excitation source was a GWU – Lasertechnik GmbH optical parametric oscillator pumped by the third harmonic of a Quanta System Nd:Yag laser.

The fluence was therefore on the order of 0.1 mJ/cm^2, with a beam shaped by a rectangular slit 1x10mm. The photoacoustic signal was considered as the peak to valley value of the oscillation

observed on the oscilloscope (Figure 4.6). Each sample was controlled comparing the extinction spectra before and after each measurement.

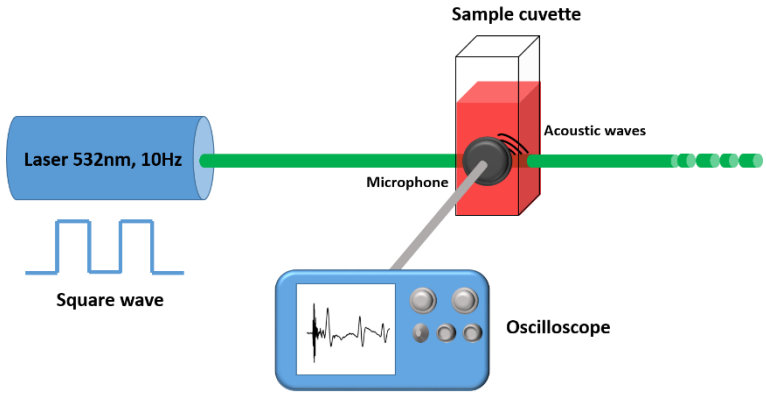

Figure 4.5: Photoacoustic Spectroscopy setup and recorded signal scheme.

The equation which describes the photoacoustic signal can be written as:

$$S = kn_{ph}\left(E_\lambda \beta / C_p \rho\right) \tag{4.30}$$

The signal depends on the instrumental constant k, the number of absorbed photons n_{ph}, the photon energy E_λ, the volumetric thermal expansion coefficient β, the heat capacity at constant pressure C_p and the solvent density ρ.

The signal of the sample has to be correlated to the signal of a calorimetric reference and the substance generally used is $KMnO_4$-$CuSO_4$ solution, because the absorption covers the whole Vis- near IR region, releases all the absorbed energy as heat instantaneously and does not scatter light.

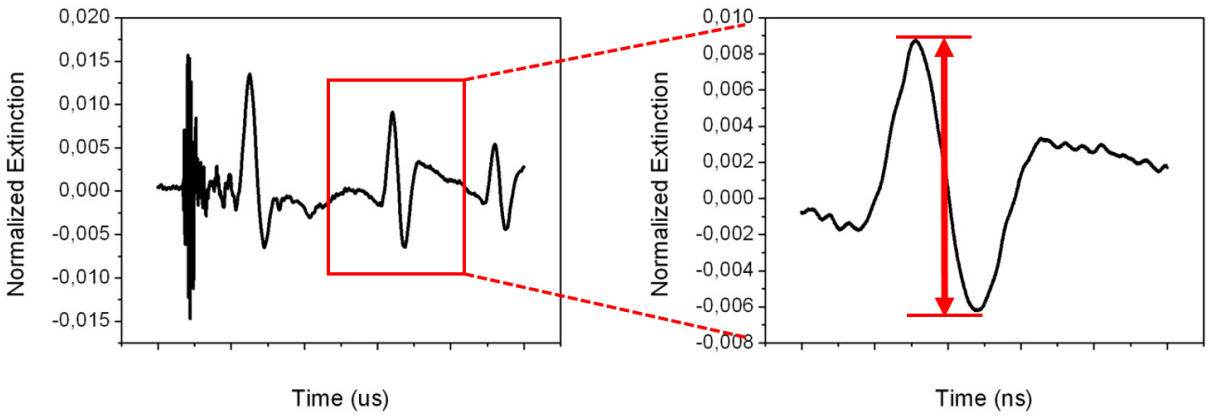

Figure 4.6: Example of photoacoustic signal and zoom in the first “echo”, with a highlight on the peak-valley measurement

The signal was normalized for small extinction variations between sample and reference: we correlated the absorption contribution of the sample to the ratio between the slope of the reference and the sample one (Figure 4.7).

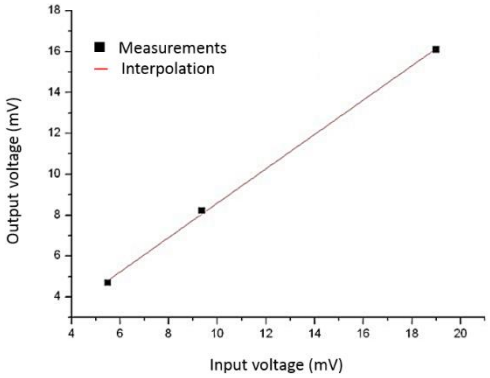

Figure 4.7: Fitting of linear ratio between photoacoustic signal and energy

In absence of other photochemical and photophysical processes in the sample, the distance between the reference and the sample slope, measured starting from the same extinction, can only depend on scattering losses.

Chapter 5

5 RESULTS

In this Chapter we show all the different analysis that we have conducted on different gold nanostructures, comparing solution and films, functionalized systems, different matrices and photothermal properties. All the measurements lead to the characterization of an optical limiting material for cw laser protection. In particular, we will present a comparison between film and solution of gold nanostructures (paragraph 5.1), their functionalization with an organic molecule to improve the limiting action (paragraph 5.2) and a specific analysis of different AuNPs film in polycarbonate and silk matrices (paragraph 5.3-4). The thermal effect generated in these systems by cw laser irradiation has been correlated with absorption contribution, measuring separately the linear scattering contribution and the photoacoustic measurements (paragraph 5.5). Comparison between experimental and theoretical models are discussed (paragraph 5.6).

5.1 Gold nanospheres in solution and in polymer matrix

In this paragraph we compare nonlinear responses of AuNPs in CH_2Cl_2 solution and in polycarbonate matrix, in order to understand if properties studied in literature for solution can be obtain also in a film: a solid free standing smart material could be a good candidate for the realization of a protection device.

Gold nanoparticles synthesized through the Turkevich[109] method described in Chapter 3 and transferred into CH_2Cl_2 with a concentration of 8.2×10^{-9} mol_{NP}/dm^3, have been compared with a solid sample of AuNPs in polycarbonate (PC) matrix through z-scan, optical limiting and temporal response measurements. AuNPs extinction spectra are reported in Figure 5.1: the embedding in polymer matrix causes a red-shifts of the resonance peak, from 530 to 535 nm.

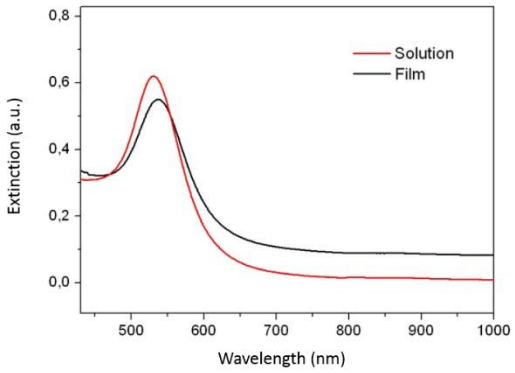

Figure 5.1: Extinction spectra of AuNPs in CH_2Cl_2 and AuNPs in PC film

The final concentration of AuNPs in CH_2Cl_2 solution is $1.2x10^{-8}$ molNP/dm^3, while the one of AuNPs in film have been calculated to be $1.14x10^{-7}$ molNP/dm^3. Such concentration difference should nearly compensate for the difference in sample thickness. The inclusion in PC does not change the shape of the resonance peak, confirming the absence of AuNPs aggregation. The higher background signal in the PC film is likely due to some weak scattering that is barely visible by visual inspection of the optically clear polymer films.

The nonlinear properties of AuNPs in CH_2Cl_2 are measured by z-scan measurements. An example of open-aperture configuration at different input powers is reported in Figure 5.2. The value of nonlinear absorption coefficient is calculated using the Sheik-Bahae method[151] to fit a Z-scan curve with a minimum normalized transmittance ca. 0.8.

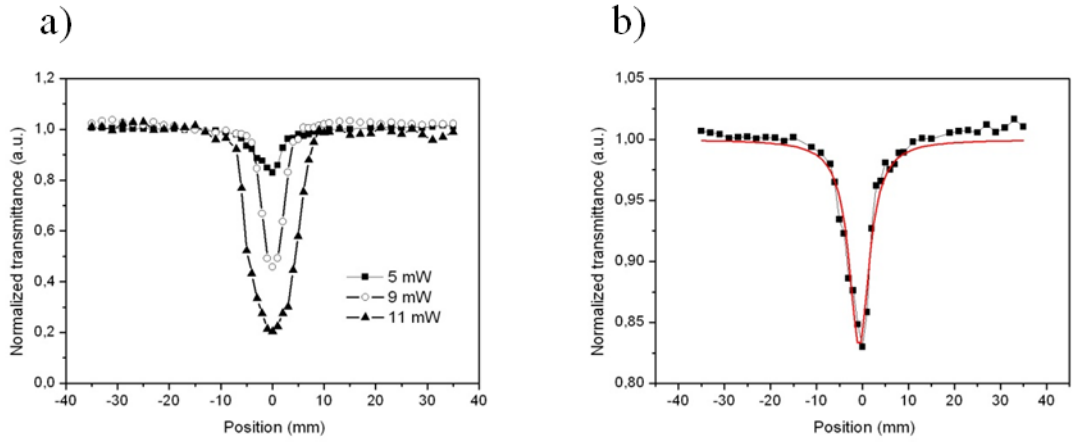

Figure 5.2: Open-aperture z-scan measurements of AuNPs in CH_2Cl_2 (dots) expressed in normalized transmittance a) at different input powers and b) with nonlinear fit (red line)

The values of β calculated result 0.1 cm/W, comparable with literature data for AuNPs in solution[40].

Optical limiting measurements at 488 nm have been made placing samples in a pre-focal position, with an exposure time of 300 ms limited by a shutter. Each point in the graph in Figure 5.3 is the mean value of irradiance, calculated in the time interval.

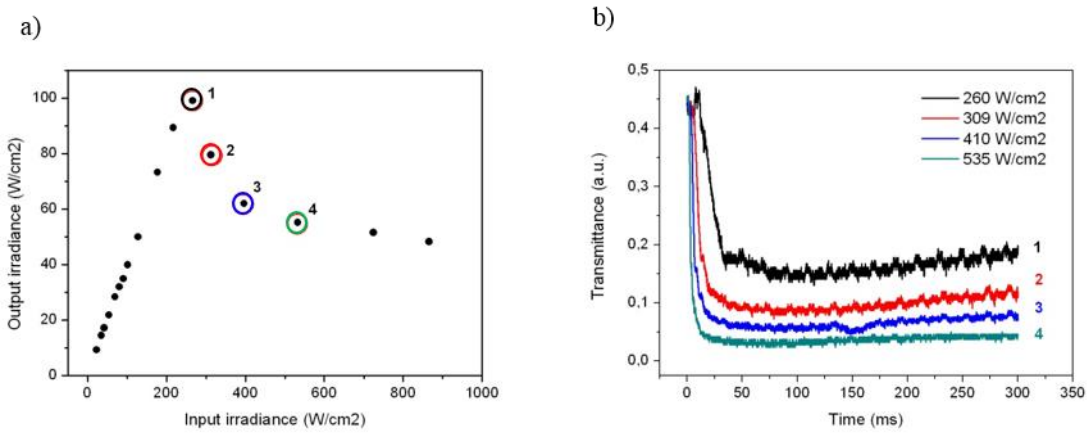

Figure 5.3: Optical limiting measurements of AuNPs in CH_2Cl_2 solution plotted as a) output versus input irradiance and b) time dependent transmittance in 300 ms interval. The curves in b) correspond to irradiance values of circled point evidenced in a).

High input irradiance produces a matrix modification, visible by comparing the output irradiance at fixed position with that obtained at different positions on increasing the input irradiance (Figure 5.3). For this reason we preferred performing measurements while varying the irradiated spot on the sample, in order to avoid affecting the measurements with previous irradiations. Error bars are calculated with a 5 measures statistics.

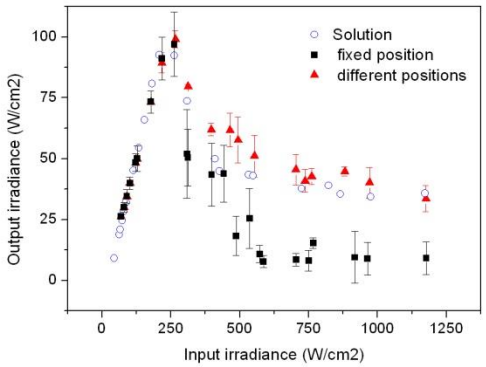

Figure 5.4: Comparison of optical limiting measurements of AuNPs solution and film at the same sample position and at different positions

Another interesting comparison can be made observing the temporal response of solution and film samples Figure 5.5 shows the transmittance variation at different input irradiances for

solution and films. In the first 30 ms, the transmittance decrease is faster for the solution, probably due to the easier refreshing of the media surrounding the nanoparticles.
Nevertheless at longer time the irreversible modification of the film causes a continuous decreasing in transmittance, which results in a mean value of output irradiance comparable with the solution.

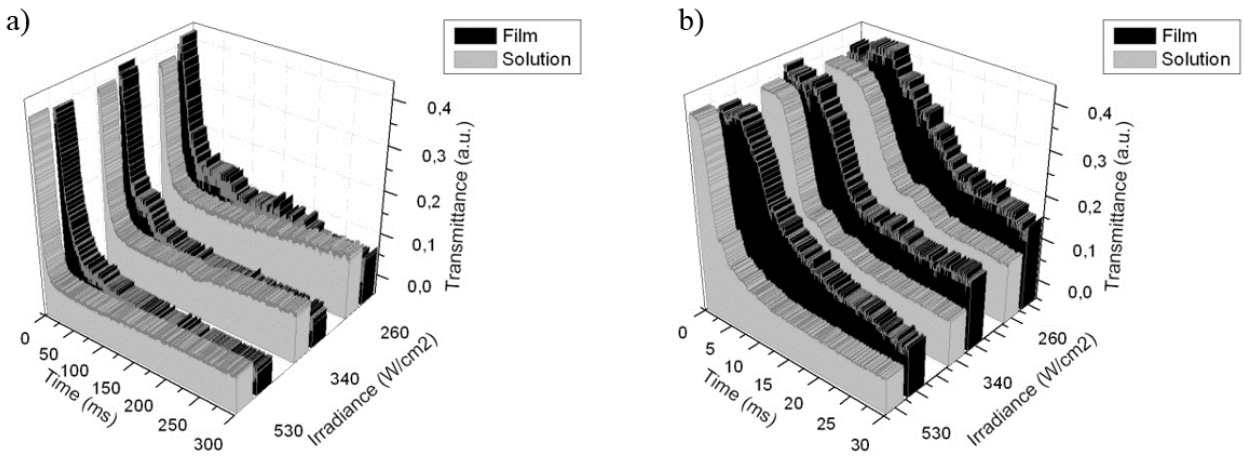

Figure 5.5: Comparison of transmittance variation of AuNPs in solution and in film a) in 300 ms and b) zoom in 30 ms

In view of the production of a smart optical limiting device, it can be useful to extend the protection in a wide range of wavelengths: we have made optical limiting measurements at 488, 514 and 647 nm, shown in Figure 5.6. Threshold values, defined as the deviation from linearity, have a strong dependence from the absorption characteristics: the best efficiency is evident at 514 nm irradiation, corresponding to the resonance peak, with an output of 25 W/cm^2 at input irradiance of 85 W/cm^2. At 488 and 647 nm instead the performances are poorer, in particular for the last one that is out of the resonance region.

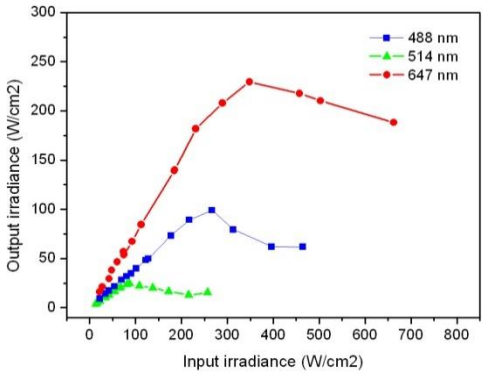

Figure 5.6: Optical limiting measurements of AuNPs film at three different wavelengths

Nonlinear absorption coefficient calculated as 0.1 cm/W is comparable with the values reported in the literature for gold nanoparticles colloids.

5.2 Gold nanospheres and core-shells functionalized with fulleropyrrolidine

In order to improve the protective action of these smart materials we decided to combine the thermo-optical process with a faster one, so as to reduce the light intensity that can reach the eye during an accidental exposure. We functionalized two different metal nanostructures with thiolated-fulleropyrrolidine (FP-SH): gold nanoparticles and silica-gold core-shell for 514 and 647 nm irradiation wavelengths, respectively.

As we have seen in the Chapter 3, for the transfer of gold nanoparticles in an organic solvent to promote the subsequent FP-SH functionalization, instead of using common thiols[5,56,122], like thiolated-polyethylenglycol (PEG) or dodecanthiol, we preferred polyvinylpirrolidone (PVP): this steric stabilizer can be displaced by FP-SH molecules and results in a faster and more effective functionalization. Gold nanoparticles solutions, transferred in CH_2Cl_2 solvent have a concentrations of $6.4x10^{-9}$ mol_{NP}/L, while gold core-shell have a concentration of $2x10^{-11}$ Au/mL. To compare the limiting behavior of bare nanostructures with those functionalized, we add a 0.45 mM fulleropyrrolidine solution (FP-SH).

Solutions were diluted but used without further purification, to prevent nanoparticles aggregation and subsequent changes in the absorption profile. In order to verify that the unbound molecules do not cause a fictitious improvement of power limitation, also a solution of only FP-SH has been measured.

Z-scan experiments on nanoparticles functionalized and bare give information about nonlinear properties, and among these parameters we find Rayleigh range z_R, reported in Table 5.1, used as fixed parameter for the time response analysis.

Table 5.1: Nonlinear properties of the three samples obtained with an irradiation of 16 mW, with α the linear absorption coefficient, z_0 the Rayleigh range, β the nonlinear absorption coefficient, $\Delta\Phi_0$ the phase shift, n_2 the nonlinear refractive index

Sample	**α**	**z_0**	**β**	**$\Delta\Phi_0$**	**n_2**	**dn/dT**
	(cm^{-1})		(cm/W)		(cm^2/W)	(K^{-1})
AuNP	1.1	0.24	$0.9x10^{-2}$	4.6	$4.6x10^{-7}$	$2.6x10^{-4}$
AuNP-S-FP	1.2	0.25	$1.2x10^{-2}$	4.7	$4.7x10^{-7}$	$2.7x10^{-4}$

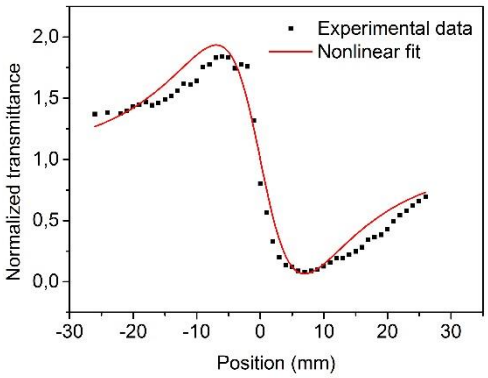

Figure 5.7: AuNP-S-FP closed-aperture z-scan measurement (black point) and nonlinear fit (red line) at 16mW

Parameters obtained from the fit of the Z-scan are in the same order of magnitude as literature reported values[39,40,83].

Optical limiting (OL) measurements performed with the sample in a pre-focal position (with a beam diameter w=100 μm) show a nonlinear response of AuNP-S-FP at lower input power compared to AuNPs, with similar linear transmittance. Also, a solution with only FP-SH molecules has been analyzed but no limitation occurs at comparable input power values (Figure 5.8a).

It is worth noting that, for the case of AuNP-S-FP solution samples used for OL measurements, it was not possible to eliminate the excess of FP-SH since AuNP-S-FP aggregation occurred in the course of the purification procedure. Thus, in order to further verify that the improvement of power limiting was not caused by the unbound molecules, solutions with three different concentrations of FP-SH were analyzed: corresponding to 50, 100 and 250 times excess on the calculated amount for nanoparticles coverage. The value of power limiting of these solutions did not show any noticeable dependence on concentration compared with measurements of only nanoparticles solution.This result is also confirmed by the absence of power limiting effects by only FP-SH in that range of input powers (Figure 5.8a).

Therefore, OL measurements show an improvement brought about only by the chemically bonded FP-SH molecules (Figure 5.8).

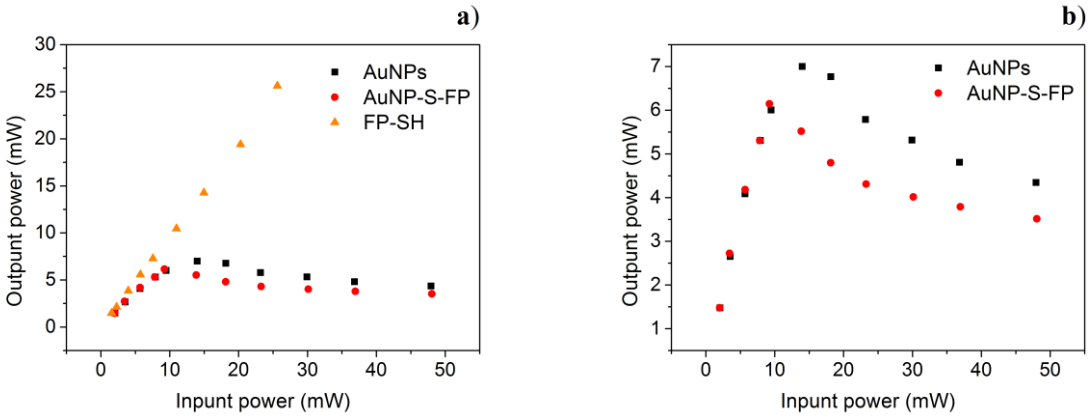

Figure 5.8: optical limiting in pre-focal position a) AuNPs, AuNP-S-FP, FP-SH and b) AuNPs and AuNP-S-FP comparison

We also analyzed the dynamics of the nonlinear transmittance responses of AuNPs and AuNP-S-FP samples using a model for the time evolution of the thermal lens effect under illumination with varying input intensities [166]. The time dependent expression for the far-field on-axis transmittance is described in the paragraph 4.4; the phase shift θ and the diffusion time t_c are kept free during data fitting in order to obtain respectively the thermo-optic coefficients and response times, are shown in Figure 5.9. The range of analysis was limited to the first 50 ms to permit a coherent characterization of all the responses at different input powers: thermal lens model approximation needs a short exposure time otherwise the relation in Equation 4.2 is no longer valid[169]. Fig. 4a shows an example of 50 ms normalized time response of AuNPs and AuNP-S-FP at 18 mW input power: it is evident observing the fitting curve, that FP-SH capped nanoparticles have a faster response than AuNPs, confirmed by fitting data reported in Table 5.2. The faster response in first milliseconds (Figure 5.9b) of the thioled nanoparticles results in a lower total fluence compared to the bare ones.

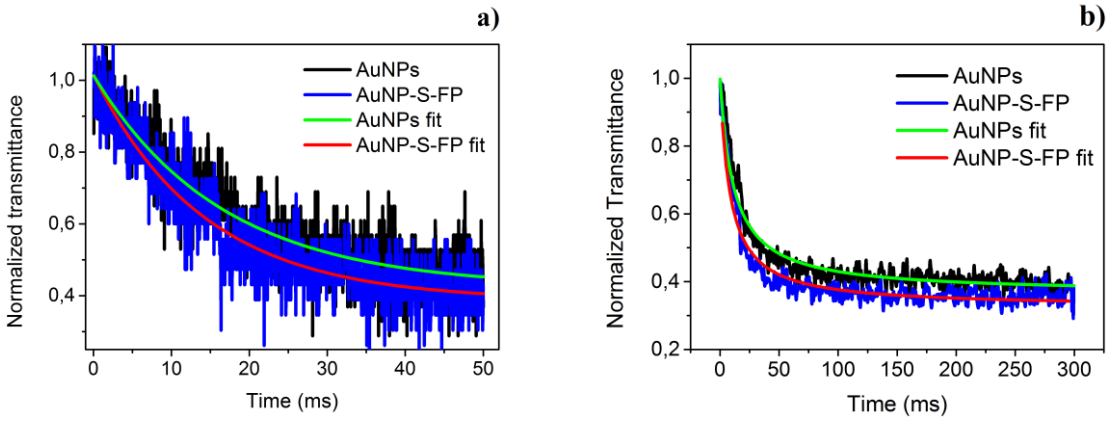

Figure 5.9: Examples of normalized thermal responses of AuNPs (black line) and AuNP-S-FP (blue line) samples with nonlinear curve fits (green and red lines) at (a) 18 mW input power and (b) 24 mW input power.

Thermal time response values, thermo-optical coefficients and nonlinear phase shifts θ, obtained through a systematic study at different input powers with and without FP-SH functionalization, are resumed in Table 5.2. At first we fit data with free parameters for both samples and notice that time response decreases with the increase of input power, faster for coupled system than bare AuNPs.

Table 5.2: Values of thermal response time (tc), nonlinear phase-shift (θ) obtained by fits for different input powers, and calculated thermo-optic coefficient (dn/dT)

P	**t_c** (ms)		**D** (m^2/s)	**θ**		**dn/dT** (K^{-1})	
	Au	*AuNP-S-FP*	*Au*	*Au*	*AuNP-S-FP*	*Au*	*AuNP-S-FP*
18	194	174	$1.3x10^{-7}$	10.1	12.4	$3.6\ x10^{-4}$	$4.1\ x10^{-4}$
24	112	95	$2.2\ x10^{-7}$	13.4	16.0	$3.6\ x10^{-4}$	$4.0\ x10^{-4}$
32	76	61	$3.3\ x10^{-7}$	17.8	19.9	$3.5\ x10^{-4}$	$3.7\ x10^{-4}$
38	53	41	$4.7\ x10^{-7}$	19.9	22.6	$3.4\ x10^{-4}$	$3.6\ x10^{-4}$
50	32	25	$7.7\ x10^{-7}$	24.8	28.1	$3.2\ x10^{-4}$	$3.4\ x10^{-4}$

To understand the behavior of the two systems and obtain the thermo-optic coefficient, we fixed the thermal diffusion coefficient (D) (Equation 4.2), which decreases in presence of nanostructures with respect to the pure solvent, as shown in previous studies[21].

With D derived from the analysis of AuNPs with free parameters (both t_c and θ) we can so fit AuNP-S-FP responses and determine the nonlinear phase-shift. Values of thermal response time (t_c), nonlinear phase-shift (θ) obtained by fits for different input powers, and calculated thermo-optic coefficient (dn/dT). The thermo-optic coefficients result higher for AuNP-S-FP than for AuNPs, of around 10^{-4} (Table 5.2), comparable with values obtained in closed-aperture z-scan measurements (Table 5.1).

The temporal responses in Figure 5.9 show that these differences are not just represented by the final transmittance values after 300 ms irradiation, but are also evident in the faster transmittance decrease for AuNP-S-FP in the first 50 ms. Actually, it is the integrated irradiance over the 300 ms interval, i.e. the fluence, that should be kept under control to avoid damages to the eye. With this in mind, in order to give information about the efficiency of protection, we have integrated the output intensities at different input powers and compared the results for AuNPs and AuNP-S-FP.

Despite the fact that all the data in Table 5.3 pertain to dilute solutions with a linear transmission of 77%, the use of functionalized NPs produces a significant improvement in the attenuation of the output fluence.

Table 5.3: Fluences of AuNPs and AuNP-S-FP calculated as the integral of the output irradiances (mW/cm^2) in 300 ms, and transmittances (T)

		AuNPs			**AuNP-S-FP**		
Input Power *(mW)*	***Input fluence*** (mW·s/cm^2)	***Linear fluence*** (mW·s/cm^2)	***Output fluence*** (mW·s/cm^2)	***T***	***Linear fluence*** (mW·s/cm^2)	***Output fluence*** (mW·s/cm^2)	***T***
18	20318	15627	9038	0.38	15413	7975	0.27
24	27091	20837	8318	0.25	20551	6983	0.19
32	36122	27782	7502	0.18	27401	6616	0.13
38	42894	32991	6782	0.13	32539	6120	0.1
50	56440	43410	6463	0.09	42814	5695	0.07

In order to get optical limiting properties in a wider wavelength range, we have also studied gold nanoshells (AuNSs) whose plasmonic resonance can be tuned over all the visible and near infrared range depending on the ratio between Au shell thickness and SiO_2 core radius. This offers us the opportunity to protect the eyes against laser emitting in the red region. Measurements were conducted on bare and functionalized AuNS-FP nanoshells using 647 nm irradiation.

Optical limiting in 300 ms interval shows again an improvement in limitation effects upon functionalization with FP-SH. The nonlinear behaviour (Figure 5.10) shows significant differences with respect to that of gold nanoparticles: the nonlinear transmission starts at around 20 mW input power and reaches a *plateau*.

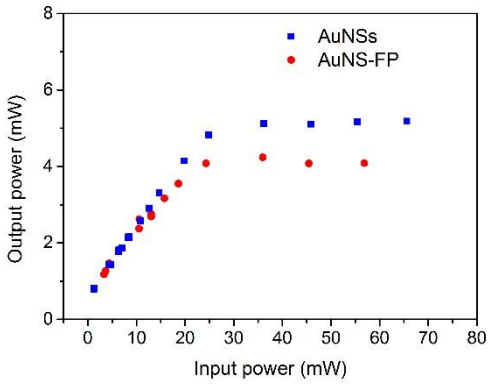

Figure 5.10: Optical limiting in pre-focal position of AuNSs (blue dots) and AuNS-FP (red square)

However, in order to obtain comparable limitation at high input intensity, the linear transmission of the nanoshell samples is smaller than that of the AuNPs, evident by absorption spectra in Figure 5.11**Errore. L'origine riferimento non è stata trovata.**. This can be explained by a greater contribution of liner scattering to the extinction spectra of the nanoshells[88,110].

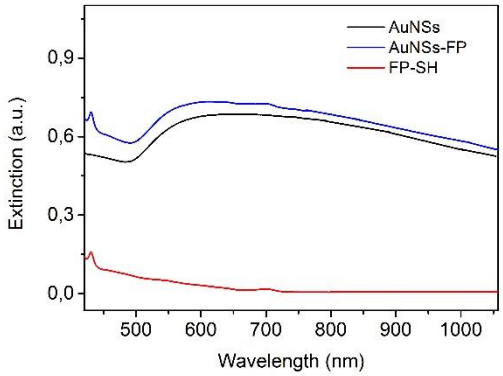

Figure 5.11: Extinction of AuNSs (black), AuNS-FP (blue) and FP-SH (red)

Optical power limiting values for both nanoshell systems are reported in Table 5.4: in terms of the improvement obtained upon functionalization, the results are comparable with those for AuNPs, but we have to remark the different linear absorbance of the two systems, changing from around 0.14 for AuNPs to 0.6 for AuNSs.

Table 5.4: Optical power limiting values of AuNSs and AuNS-FP at different input intensity

P_{in} (mW)	P_{out} (mW)	
	AuNSs	*AuNS-FP*
19	4.1	3.5
25	4.8	4.1
36	5.1	4.2
46	5.1	4
55	5.1	4

Transient transmission measurements on AuNSs confirm an improvement of temporal response for functionalized nanoshell system, as we have seen for nanoparticles. An example of temporal response curves is reported in Figure 5.12: the transmittance decreases faster for AuNS-FP than for AuNSs and the final value reached in a 50 ms time window is lower.

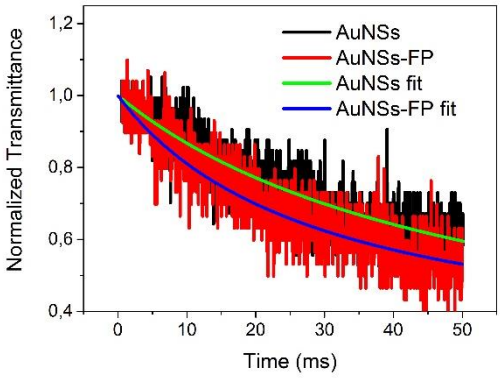

Figure 5.12: Examples of time responses curves of AuNSs (black line) and AuNS-FP (red line) at 36 mW input power, and and thermal lens model nonlinear fit

As we have seen before, the response is faster for high input powers, with a strong transmittance decrease in the first 50 ms (Figure 5.13).

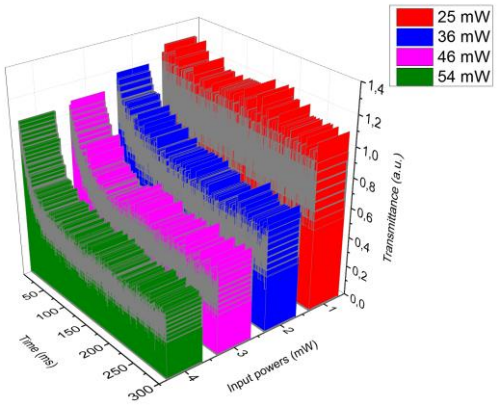

Figure 5.13: Normalized responses of AuNS-FP sample at different input power in a 50 ms interval

This can represent an efficient method to functionalize gold nanoparticles and nanoshells, synthesized in aqueous solution, with a thiolated fulleropyrrolidine. SERS and TGA characterizations on this system after purification confirm the effective bonding of the molecules on the metal surface. Nonlinear optical measurements show improvements in the OL effect in the functionalized AuNPs both in terms of a reduced nonlinear transmission and of a faster response, fully described in Chapter 6.

5.3 Different concentrations of gold nanoparticles in polycarbonate matrix

In this Paragraph we made an in depth study of the AuNPs film through different analysis and characterize the self-diffraction beam pattern. To promote the inclusion of AuNPs in polycarbonate films, Au colloids were firstly functionalized with mPEG2000-SH, the water was removed and NPs were dissolved in dichloromethane, obtaining a solution with a concentration of $7.6x10^{-9}$ mol/L. Nanoparticles were mixed with polycarbonate by ultrasonication in dichloromethane to obtain solutions with different concentrations. The solvent was evaporated by drying under vacuum at 50 °C for 1 h in a Petri dish. We finally obtained two films, shown in Figure 5.14, with different NPs:PC weight ratios:, 2.5:200 (AuNPs1), and 6:200 (AuNPs2) and a final thickness of 109 and 103 μm, respectively.

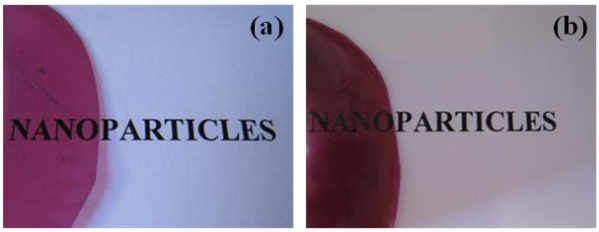

Figure 5.14: AuNPs in PC films with concentration (a) 1.14x10-7 molNPs/L (AuNPs1), and (b) 2.74x10-7 molNPs/L (AuNPs2).

Open and closed-aperture Z-scan measurements permit the determination of an effective nonlinear absorption coefficient and of the nonlinear refractive index, respectively.

The PC matrix does not show nonlinear behavior even at the highest energies used: the data indicate that there is no nonlinear absorption contribution nor laser damage. AuNPs in PC measurements reported in Figure 5.15 show a deep dip of nonlinear transmittance.

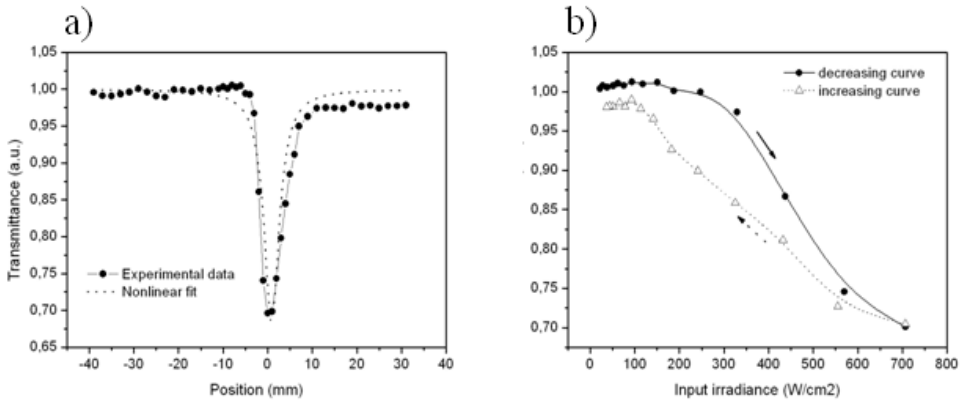

Figure 5.15: Open aperture z-scan of AuNPs2 at 488 nm irradiated with 7 mW reported a) as a function of sample position b) as a function of irradiance; the solid line is obtained on approaching the focal plane, the dotted line is obtained on moving away.

Notice that the linear transmittance value in the flat regions of the Z-scan curve (Figure 5.15a) shows some reduction after crossing the focal plane. Furthermore, Figure 5.15b shows some hysteresis on cycling the irradiance on the sample while performing a Z-scan. Both features are probably due to some laser induced matrix modification when the irradiance reaches high values (see below).

The parameters obtained from the fit of the Z-scan data are reported in Table 5.5, and are in the same order of magnitude as those reported in the literature.

Closed Aperture Z-scan experimental data of AuNPs2 at 488 nm, are reported in Figure 5.16. The reduced data are obtained as the ratio (closed aperture)/(open aperture) Z-scan values. The peak to valley configuration suggests that the sign of n_2 is negative, indicating self-defocusing effect. The solid line is a theoretical fit.

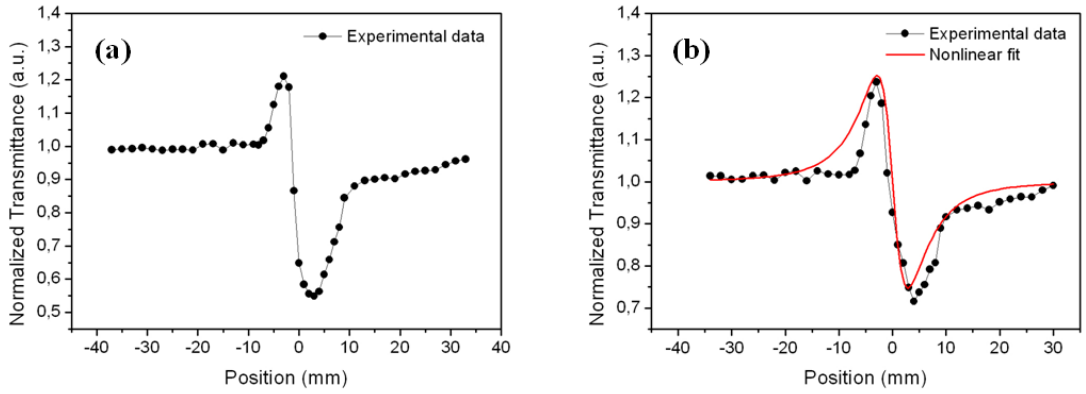

Figure 5.16: AuNPs2 at 488 nm: (a)Closed-aperture z-scan of and (b) ratio closed/open with fit Equation 4.4.

The modulus of the nonlinear refractive index is high for AuNPs2 at 514 and 488 nm, which are wavelengths close to the plasmon resonance peak. A comparison with data reported in the literature for organic dyes in solid matrices as well as for AuNPs in solution is also provided in Table 5.5.

Table 5.5: Nonlinear optical parameters of dyes in films and gold nanoparticles in solution of recent works; λ is the irradiation wavelength, β the effective nonlinear absorption coefficient, n_2 the nonlinear refractive index and dn/dT thermo-optical coefficient.

Sample	**matrix**	**λ**	**β**	**n_2**	**dn/dT**	**Ref.**
		nm	*cm/W*	*cm^2/W*	*K^{-1}*	
Night blue (2006)	PMMA film	633		-1.47×10^{-7}		[161]
Phthalocyanines in PMMA (2007)	PMMA film 10μm	633	1.1	-1.5×10^{-5}		[134]
Amido Black 10 B (2007)	PVA film	633		-1.5×10^{-7}		[162]
Metanyl yellow (2009)	film	532	1×10^{-3}	-4×10^{-8}		[163]
AuNPs (2008)	water solution	633		-1.6×10^{-8}	-2×10^{-4}	[136]
AuNPs in Cyclohexanone (2010)	solution	532		-3×10^{-7}	-1.5×10^{-4}	[39]
AuNPs (2010)	water solution	532		-1×10^{-8}	-2×10^{-5}	[100]
AuNPs in castor oil (2012)	solution	532		-5×10^{-7}	-2×10^{-4}	[83]
AuNPs (2012)	solution	633	0.5	-2×10^{-7}		[40]
AuNPs1	film	488 514	[a] 5×10^{-2} [b] 3×10^{-2}	-1×10^{-6} -2×10^{-5}	-2.9×10^{-4} -4.4×10^{-4}	
AuNPs2	film	488 514	[a] 7×10^{-2} [b] 6×10^{-2}	-1×10^{-6} -3×10^{-5}	-2.3×10^{-4} -5.0×10^{-4}	

a- I_0=1121 W/cm²
b- I_0=660 W/cm²

CW measurements show that the nonlinear absorption depends on a thermal effect. The effective nonlinear absorption coefficient (β) depends on irradiation wavelengths: β reported in

Table 5.5 at 514 nm is obtained with much lower irradiance than at the other wavelength. For 660 W/cm^2 at 488 nm no signal occurs. This indicates that at comparable irradiance the nonlinear absorption coefficient is higher at 514 nm. As expected, the β values for AuNPs2 are consistently larger than those for AuNPs1 owing to the larger NP concentration in the polymer. A peak-to-valley amplitude greater than 1.7 of the Rayleigh range (z_0) confirms the thermal origin of the phenomenon[151,170]. In Table 5.6 are reported the on-axis nonlinear phase-shift, $\Delta\Phi_0$, for different wavelengths.

When considering only thermally induced nonlinear refraction, making use of the thermo-optical coefficient, *dn/dT*, one can express the refractive index change (Δn_{th}) as:

$$\Delta n_{th} = -\frac{dn}{dT} \cdot \Delta T \tag{5.1}$$

If, in the steady state (cw irradiation), it is assumed that

$$\Delta T = \alpha\omega_0^2 I_0/4K \tag{5.2}$$

and $\Delta n_{th} = n_2 I_0$, we can extract the thermo-optical coefficient from:

$$\frac{dn}{dT} = -n_2 \frac{4\,\mathrm{K}}{\alpha\omega_0^2} \tag{5.3}$$

In Equation. 5.2, α is the linear absorption coefficient, ω_0 the beam waist and K is the thermal conductivity.

All the parameters used and our results for the thermo-optical coefficient are reported in Table 5.6. Values in the order of 10^{-4} K^{-1} for *dn/dT* are comparable with the literature data reported in Table 5.5.

Table 5.6: Nonlinear parameters obtained from z-scan measurements: z_0 is the Rayleigh range, ω_0 is the beam waist, α is the linear absorption coefficient, I_0 irradiance at the focus, L_{eff} the effective length, S the diaphragm aperture, ΔΦ the on-axis phase shift, n_2 the nonlinear refractive index and dn/dT the thermo-optic coefficient.

Sample (488 nm)	z_0 *cm*	ω_0 *cm*	α_{Au} *cm^{-1}*	I_0 *W/cm^2*	L_{eff} *cm*	S	Δ Φ	n_2 *cm^2/W*	dn/dT
AuNPs1	0.61	2.5x10^{-3}	33.1	1121	9.1$_x$10^{-3}	0.62	-1.63	-1.23x10^{-6}	-2.9x10^{-4}
AuNPs2	0.20	2.3x10^{-3}	61.8	1121	7.7x10^{-3}	0.73	-1.45	-1.31x10^{-6}	-2.3x10^{-4}

Sample (514 nm)	z_0 *cm*	w_0 *cm*	α_{Au} *cm^{-1}*	I_0 *W/cm^2*	L_{eff} *cm*	S	Δ Φ	n_2 *cm^2/W*	dn/dT
AuNPs1	0.33	2.6x10^{-3}	53.1	1036	8.5x10^{-3}	0.74	-2.30	-2.68x10^{-6}	-4.4x10^{-4}
AuNPs2	0.12	2.6x10^{-3}	86.4	1036	6.9x10^{-3}	0.64	-3.14	-4.20x10^{-6}	-5x10^{-4}

Optical limiting measurements were performed in a pre-focal position to compare, with a beam area of 0.03 mm^2 at 488 and 514 nm wavelengths. The exposure time has been limited to 300 ms by the use of a shutter. Experiments were also conducted by putting a 7 mm diameter diaphragm before the sensor, representing the pupil diameter in the worst condition.
Measurements on neat polycarbonate film at different wavelengths are made and no limitation occurs. An example of limitation for AuNPs2 with and without diaphragm is reported in Figure 5.17.

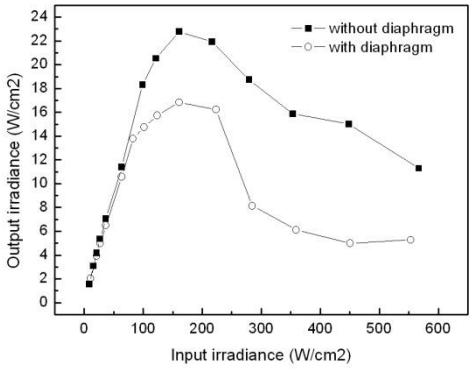

Figure 5.17: Optical limiting of AuNPs2 at 488 nm with (open circles) and without (black squares) diaphragm.

The threshold values of the input intensities required for the beginning of optical limiting, also corresponding to the appearance of self-diffraction rings, are reported in Table 5.7 for different wavelengths. Best result is obtained for the more concentrated AuNPs2 sample.

Table 5.7: Optical limiting thresholds at different wavelengths for the two samples. I_{IN} and I_{OUT} are the input and the output irradiances, respectively.

Sample	488 nm		514 nm	
	I_{IN}	I_{OUT}	I_{IN}	I_{OUT}
	W/cm^2		W/cm^2	
AuNPs1	243	84	166	45
AuNPs2	161	22	123	13

The effect of a focused cw laser beam on AuNPs doped polymer samples is to induce a local heating followed by heat diffusion in the medium. This effect can be easily observed by recording the dynamics of the sample transmittance during a time interval of 300 ms for different irradiation powers, with the concentric rings formation.

We tried to give a global description of the optical limiting response of our systems with 3D depiction of transmittance decrease in function of time for different input powers
Experimental data have been collected by positioning samples 10 mm before the beam-waist position, with an area of around 0.03 mm^2. The transmittance is recorded in a time window 0-300 ms, while the samples are irradiated with laser wavelengths at 488 and 514 nm, with input irradiance in the range 30-700 W/cm^2.
The transmittance is a function of both the input power and the irradiation time: for AuNPs2 at 514 nm thetransmittance (T_L = 0.10) decreases by increasing the power and reaches a constant value of 0.04 after 300 ms, by pumping with an irradiance of about 160 W/cm^2. With input irradiance of 300 W/cm^2 and above, a value of 0.01 is attained after less than 50 ms. The behavior of AuNPs2 sample is reported in Figure 5.18, using input irradiances in the range 40-700 W/cm^2.

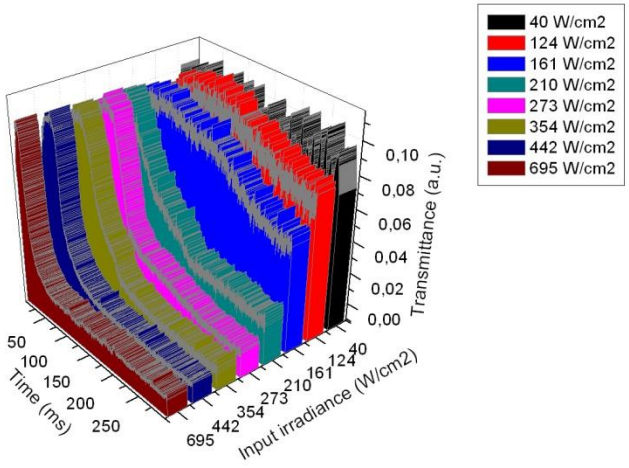

Figure 5.18: Response dynamics of AuNPs2 sample at 514 nm for different irradiance values without diaphragm in a 300 ms interval at 10 mm before focus.

The thermal diffusion effect of all film samples has been measured at different input powers using 488 and 514 nm wavelengths. All results are reported in Table 5.8, with similar input

irradiance for the two wavelengths. The response time and the plateau transmittance decrease at increasing concentration, as expected.

Table 5.8: Threshold values and dynamics of optical limiting measured at 10 mm before the focal point. T_{in} is the linear transmittance of the samples. In the 300 ms measurement time window, $t_{1/2}$ is the signal at half-time, $t_{plateau}$ is the time required to reach the plateau and $T_{plateau}$ is the least value of transmittance (all times in ms).

Wavelength	I	AuNPs1				AuNPs2			
nm	*W/cm²*	T_{in}	$t_{1/2}$	t_{plat}	T_{plat}	T_{in}	$t_{1/2}$	t_{plat}	T_{plat}
488	250	0.44	160	300	0.12	0.14	14	140	0.003
514	180	0.31	191	240	0.034	0.11	85	170	0.002

The thermo-optical effect can be observed also by detecting the far field beam shape with a CCD camera.

The self diffraction beam patterns, generated with a 514 nm TEM_{00} laser beam, on AuNPs2 placed at 10 mm in the pre-focal position, are shown in Figure 5.19 (images are collected with 15 Hz acquisition rate, i.e. at 67 ms time intervals): the sample forms a doughnut shaped diffraction pattern with a bright spot in the center. The transmittance variation during 300 ms irradiation time is shown in Figure 5.20 and compared with the corresponding diffraction patterns at the end of the time steps.

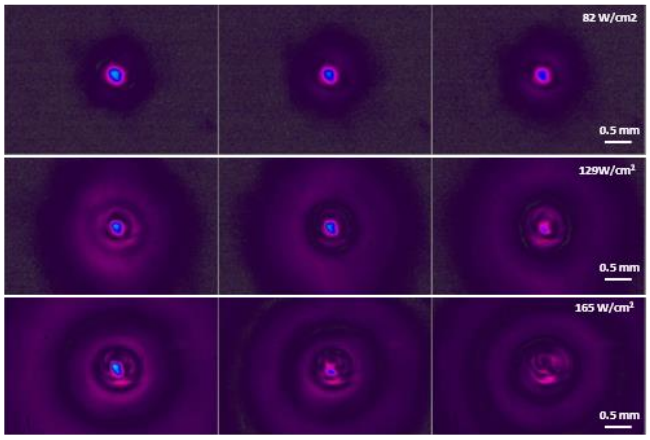

Figure 5.19: Diffraction patterns. generated by AuNPs2 placed at 10 mm before focus, irradiated for 300 ms with a 514 nm TEM_{00} laser beam at different input powers: 82, 129, 165 W/cm^2.

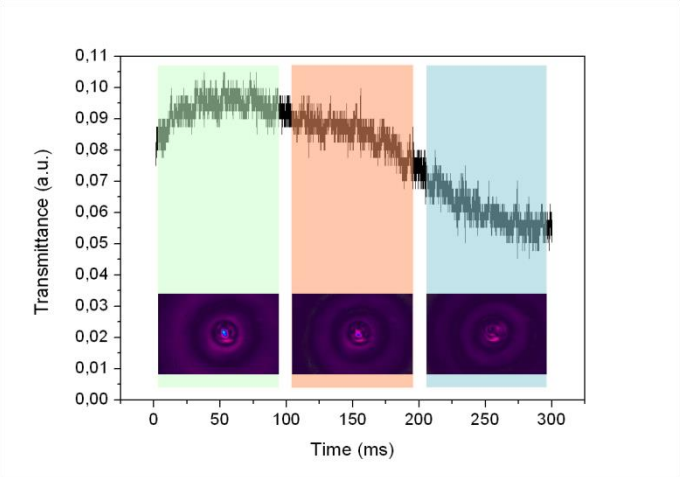

Figure 5.20: Response of AuNPs2 placed at 10 mm before focus, irradiated for 300 ms with a 514 nm TEM_{00} laser beam. The insets show the self-diffraction patterns collected with 15 Hz acquisition rate.

At increasing input power, when the laser intensity exceeds a certain threshold value, multiple concentric diffraction rings appear: there is a dynamic change in the pattern during irradiation, with a continuous ring formation with expanding propagation. The number and dimension of rings change with different wavelengths under the same intensity and with the sample position with respect to the focal point[171].

Measurements made after the focus, instead, present a dark spot in the middle, as reported in Figure 5.21 (clearly seen in panel b). Therefore, the post-focal position yields an increase of the limitation efficiency, changing the threshold irradiance value, defined as that for initial deviation from linearity, from around 230 W/cm^2 to 100 W/cm^2, with a maximum output irradiance of 26 W/cm^2 instead of 50 W/cm^2. These results agree with those reported in the literature[171] and are exemplified in Figure 5.22 for convergent (black squares) and divergent (open circles) beam on a self-defocusing medium.

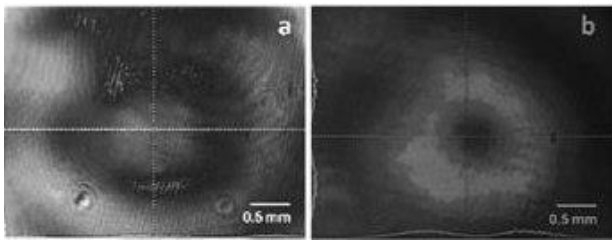

Figure 5.21: Self diffraction patterns at far field generated after a 300 ms irradiation, collected in a) pre-focal position b) post-focal position.

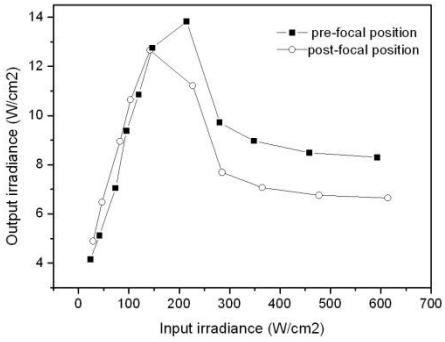

Figure 5.22: Input/output analysis at 514 nm of AuNPs2 for a10 mm pre (black squares) and post (open circles) focal positions, with around 0.03 mm^2 illuminated area.

Clearly, to optimize the protection the position of the active material in the focusing system and that of the sensor are critical. In particular, as shown in Figure 5.22 moving the sample from pre- to post-focal position, with constant beam area, the threshold for deviation from linearity is reduced from 166 W/cm^2 to 130 W/cm^2. In particular, the position with respect to the focus becomes relevant when the ring thickness increases, because it is the dimension of the dark central spot that cause a significant decrease of transmitted irradiance when the sample is placed in a post-focal position.

The rings formation and the optical limiting effect due to the change of nonlinear refractive index start at irradiance close to or above the nonlinear threshold. The corresponding thermal gradient at the illuminated area, as calculated from Equation. 5.2[172], is given in Table 5.9.

Table 5.9: Temperature variation when starts optical limiting (ΔT)

Wavelength		ΔT AuNPs1		ΔT AuNPs2
nm		*°C*		*°C*
488		152		146
514		140		181

This variation reaches a temperature higher than the polycarbonate melting point (270 °C), causing irreversible changes in the polymer microstructure that are the likely origin of the hysteresis observed on cycling the irradiance Figure 5.15b), as confirmed by the irregular shape

of the central spot of the diffraction pattern recorded for irradiance values above the nonlinear threshold (Figure 5.19).
Other works based on polymer films (Table 5.5) do not consider the temperature variation induced in the matrix by dyes absorption. This is a crucial point in the nonlinear response of the sample. Only Mathews[134] notice the damage of the matrix. However, this phenomenon does not hamper the use of polymer composite materials for protection devices since it is unlikely that cw beams hit the device consecutively in exactly the same position.

The ANSI Z-136.1[103] exposure limits for visible light (400 to 700) nm for times between 18 x 10^{-6} to 10 seconds can be obtained from the relation, using a 300 ms exposure time (t):

$$MPE = 1.8 \times t^{\frac{3}{4}} = 0.7296 \left[\frac{mJ}{cm^2}\right] \tag{5.4}$$

The maximum exposure limit (MPE) is given in terms of an energy flux (or fluence) as if the energy were evenly distributed across the incident beam. For laser safety calculations, a 7-mm, aberration-free pupil is assumed, a worst-case assumption.
The MPE defined in this way can be recast in terms of maximum transmitted energy that, in 300 ms, a protection device should guarantee:

$$E = MPE \times (pupil\ area) = 0.7296 \times 0.3848 = 0.28\, mJ \tag{5.5}$$

Considering the data in Table 5.8 for the AuNPs2 sample, one can see that, when the transmittance plateau is reached for irradiation at 488 and 514 nm, the requirements for eye protection would be within reach. The energy reaching the retina in the second part of the exposure time would be roughly in the order of 50 and 20 mJ, respectively.

Different plasmonic nanostructures can be used to widen the wavelength range of operation, and a first approach has been tried with nanorods, promising for their tunable longitudinal plasmon peak and their high absorption coefficient (see Paragraph 4.5.6).
A first analysis at 647 nm irradiation wavelength of AuNRs solutions confirmed the nonlinear refraction behavior at different positions along the beam direction. In fact, in the post-focal position they act as a self-defocusing medium crossed by a divergent beam, causing the

formation of a central hole in the diffraction image. Results are in agreement with the ones obtained for gold nanoparticles, with a higher limiting in the post focal position in respect of the pre-focal position with the same beam diameter and thus irradiance value (Figure 5.23).

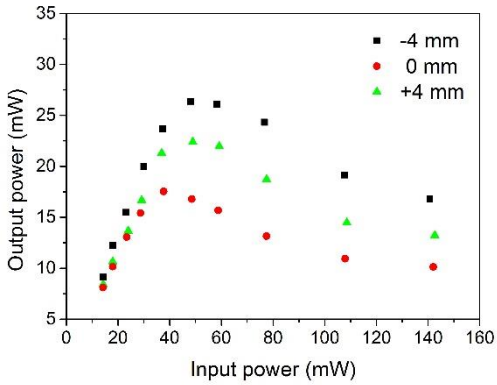

Figure 5.23: Optical limiting measurements of AuNRs solution irradiated at 647 nm in a pre-focal (balck squares), focal (red dots) and post-focal (green triangles) position

We tried to compare optical limiting measurements of AuNRs with different aspect ratio obtained by different syntheses and ageing of the solutions. As we have seen in Chapter 3, without adding a further stabilizer (e.g. PVP) we observed a reshaping of the rods. This process diminishes the aspect ratio of cylindrical rods towards cubic or spherical shapes (Paragraph 3.3.2). This behavior is shown by the comparison of optical limiting action in Figure 5.24 for three different aspect ratio with the same extinction values. Samples 1 (black dots), sample 4 (blue square) and sample 6 (pink triangles) have respectively 1.25, 1.5 and 1.3 aspect ratios. We can observe an increase of limiting action for nanorods with higher aspect ratio, in this case AuNRs4.

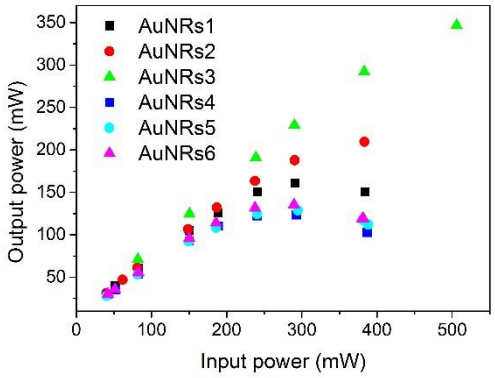

Figure 5.24: Optical limiting measurements of different AuNRs at 647 nm irradiation wavelength in a pre-focal position

Another parameter to take into account is the ageing of the solutions: if we look at the first three samples in Figure 5.24 (black, red and green dots) with the same aspect ratio, we can see very different behaviors. In this case the three samples have been synthesized 4 months before and the reshaping process generated different structures. Looking at the extinction spectra in Figure 5.25 we can see the widening of the longitudinal peak, pointing out the presence of a different contribution to the extinction. We can deduce that AuNRs2 possesses a higher scattering component in the extinction peak and less absorbed energy can contribute to the optical limiting process, confirmed by the photoacoustic measurements described in paragraph 5.5.

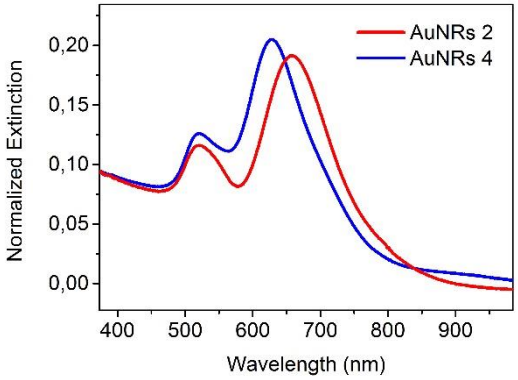

Figure 5.25: Extinction spectra of AuNRs 2 (red line) and AuNRs 4 (blue line) solutions with the same extinction intensity at 647 nm

After the transfer in organic solvent we embedded AuNRs in polycarbonate matrix and we started a preliminary study of its optical limiting properties.

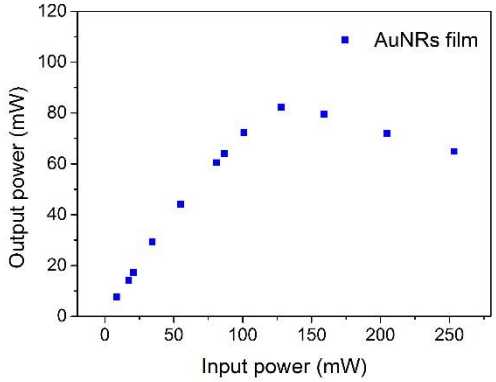

Figure 5.26: Optical limiting measurements of AuNRs film at 647 nm irradiation wavelength

Optical limiting measurements on AuNRs in PC matrix show that effective limitation occurs at 100 mW input power (Figure 5.26) and those results are similar to the one obtained for AuNPs in PC.

5.4 Gold nanoparticles in silk matrix

In order to try different embedding matrix for gold nanostructures, we conducted OL measurements at 514 nm on silk fibroin that, as we have seen in Chapter 3, is water soluble so the embedding of AuNPs is easier. Film of AuNPs in silk fibroin (Au-SF) obtained with different deposition techniques are resumed in Table 5.10: the four samples present different final extinction spectra and optical limiting properties.

Table 5.10: Au-SF samples obtain with different techniques and different concentration

Sample	***AuSF-1***	***AuSF-2***	***AuSF-4***	***AuSF-7***
Substrate	PDMS	becher	petri	petri PDMS
Ratio	2:1	1:1	1:1	2:1
Volume (mL)	5	5	5	3

Measurements on AuNPs in silk matrix reveal different optical limiting properties depending also on the deposition method, as already shown by TGA: different substrate contribute to the formation of distinct organization of silk fibers and a consequent different stability increasing temperature.

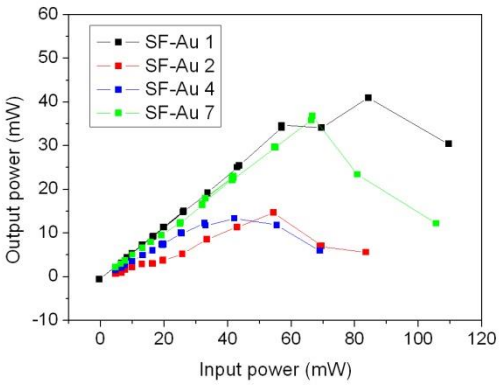

Figure 5.27: Optical limiting measurements of AuNPs in silk matrix using different substrate for the film production

In Figure 5.27 the comparison between PDMS substrate (black dots) and PDMS petri (green dots) shows a faster matrix degradation for the second: the low affinity of the solution with the support and the freedom film formation let the fibers aggregates randomly (α-elic) while the confinement generated by the petri blocks the fibers, forcing them to elongate during the solvent evaporation (β-sheet).

The two thicker samples (blue and red dots) compare the results of a plastic becher and glass petri dish: the second one present a higher affinity with the solution and the temporal responses confirms a redistribution of the fibers before the complete matrix degradation. These results are verified looking at the temporal responses of the samples shown in Figure 5.28 : the Au-SF2 (red dots) at different input powers show an instantaneous decrease of the signal, while Au-SF4 present a slower transmittance variation.

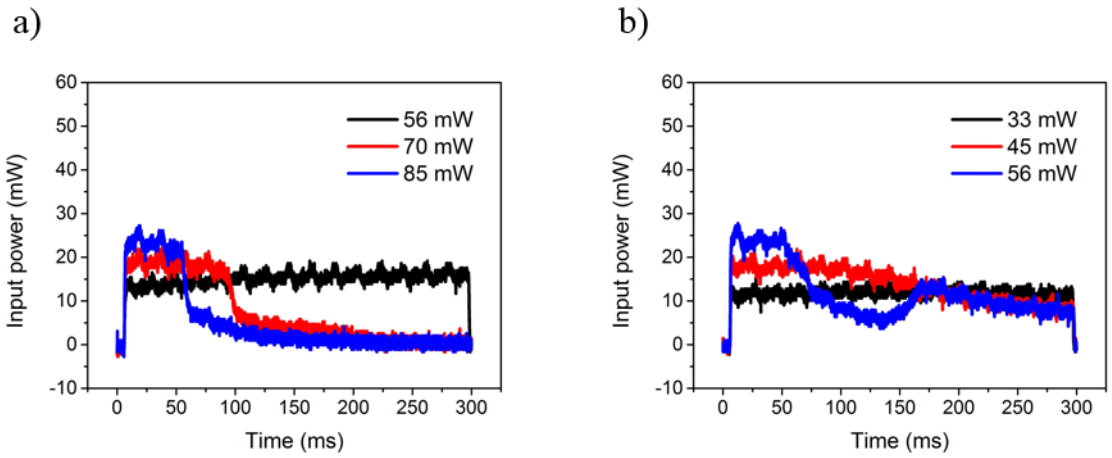

Figure 5.28: Temporal responses of a) AuNPs-SF2 and b) AuNPs-SF4

High irradiances produce a modification of the matrix revealing the presence of a melting process. The Figure 5.29a shows a microscope image where the film gets thinner and this causes the transmittance increase. In fact, the temperatures reached correspond to the matrix degradation results by TGA measurements (Paragraph 3).

Compare silk fibroin and PC matrices show that silk melts while in PC presents density variation and bubble formation (Figure 5.29b).

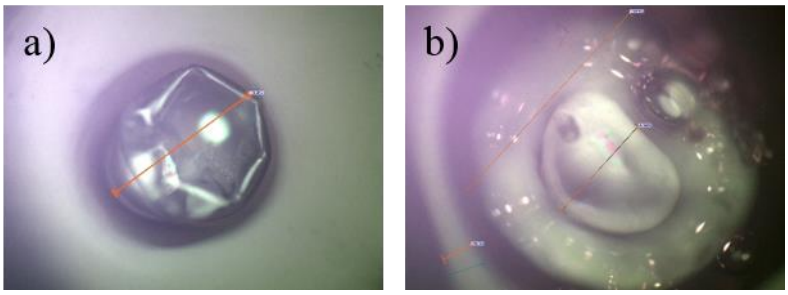

Figure 5.29: Microscope image of a) silk fibroin matrix and b) PC matrix after high input powers irradiation

The very high stability of AuNPs in fibroin matrix could be used for sensing: in fact porous matrix can be easily obtain adding acetone or by sonication (Figure 5.30). These homogeneous plasmonic matrices presents porous of around 1um, where the molecules in solution can be trapped and revealed by SERS analysis.

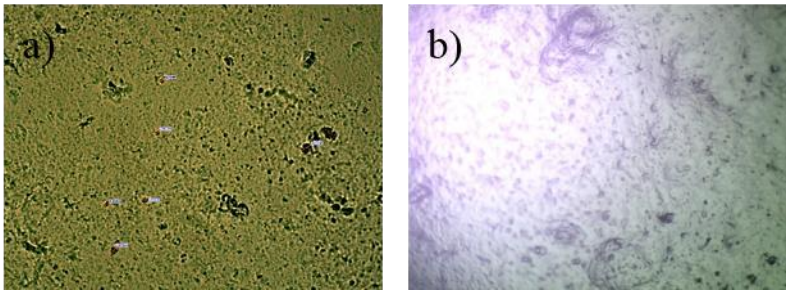

Figure 5.30: Microscope images of silk fibroin porous matrix in a) transmission and b) reflection

First SERS studies conducted on Malachite Green, a common pesticide, in these matrices show the signal of the molecule but further improvement should be done on the matrix production parameters.

5.5 Comparison between AuNPs and AuNRs with photoacoustic technique

Photoacoustic measurements give information about absorption and scattering contribution of a solution, in this case colloids. This analysis helps us to understand how nanoparticles increase the limiting process in respect with a classical absorptive medium as an organic or inorganic molecule, and to compare results obtained for AuNPs and AuNRs, starting from the same absorbance, not extinction, intensity.

In 1995 Chen et al.[173] discover an anomalous photoacoustic effect in carbon nanoparticles suspension: an amplitude three order of magnitude higher than the one produced by a dye

solution with an equivalent absorption coefficient. The effect is thought to originate in high-temperature chemical reactions between the surface carbon and the surrounding water.
Photoacoustic measurements with 514 nm pulsed laser at 10 Hz were conducted using $KMnO_4$ as the reference and on two samples in water of AuNPs and AuNRs with extinction value of 0.2, as displayed in Figure 5.31:

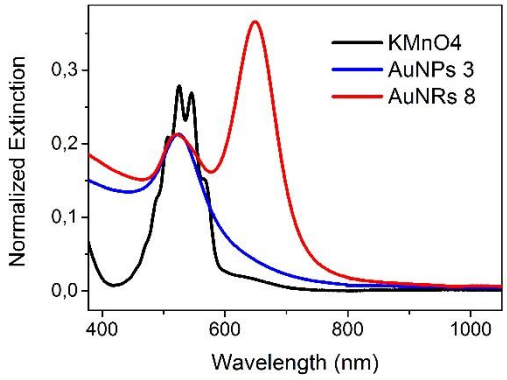

Figure 5.31: Extinction spectra of $KMnO_4$ (black line), AuNPs (blue line) and AuNRs (red line) with the same intensity at 514 nm

The photoacoustic signal, together with the energy measured, has been fitted (as described in Paragraph 4.5) and the slope gives us information about the absorption and subsequent heat conversion percentage, calculated in 93.5% for AuNPs and 86.9% for AuNRs.

Measurements have been conducted on dilute solutions of around 0.2 extinction intensity, comparing optical limiting effects of AuNPs solution with and absorbance of 93% and $KMnO_4$ with absorbance of 100%. In fact, as we have seen in paragraph 4.5, $KMnO_4$ is used as a reference for absorption in the visible range because it is an only absorptive molecule.

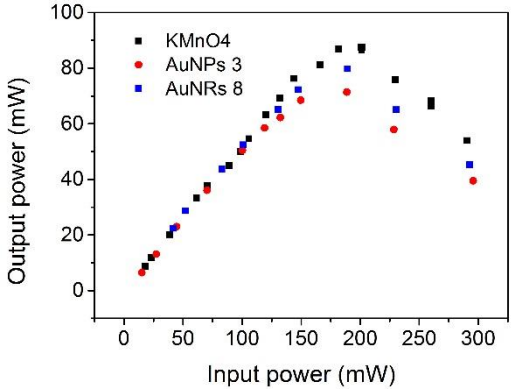

Figure 5.32: Optical limiting measurements of $KMnO_4$ (black dots), AuNPs 3 (red dots) and AuNRs 8 (blue dots) in water irradiating at 532 nm wavelength.

Figure 5.32 shows optical limiting measurement at 532 nm for solution of $KMnO_4$ and AuNPs with the same linear absorbance, highlighting the difference in threshold values for the two systems: AuNPs start limiting at around 120 mW while $KMnO_4$ at 200mW. This is a confirmation of the improvements given by the nanostructured system instead of simply absorbing molecules: not only absorption contributes at the density change and consequent the refractive index change.

Optical limiting results for AuNPs (red dots) show a lower threshold and output transmittance than and AuNRs (blue dots) at the same irradiation wavelentgh. We can explain this behavior with the different parameters that contribute to the extinction: absorption and scattering. The thermal response depends only on the absorption part so we tried to discriminate the two contributions with the photoacoustic measurements. We have also performed Z-scan measurements at 532 nm at 8 mW and 14mW.

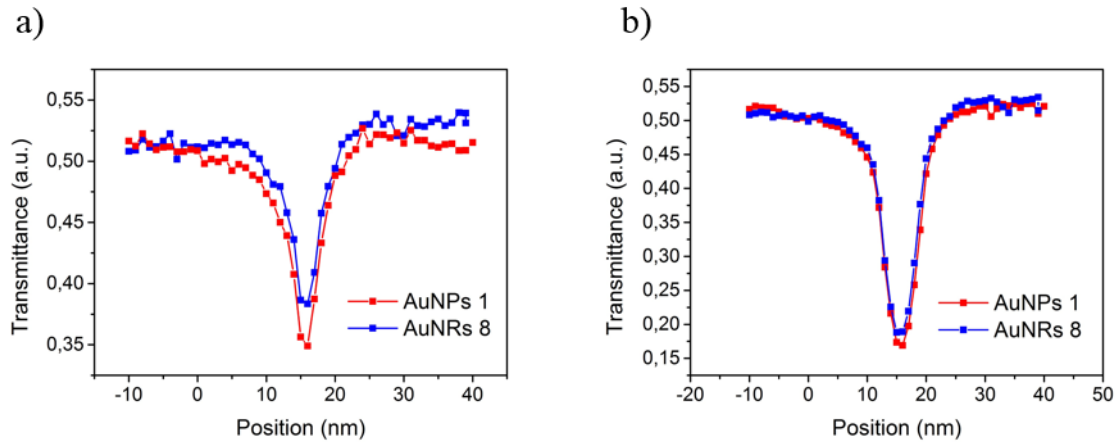

Figure 5.33: Open-aperture z-scan measurements of AuNPs 4 (red line) and AuNRs 8 (blue line)

Different results obtained for AuNPs 1 and AuNRs 8 confirm the different absorption efficiency: starting from the same extinction value at 532 nm, the two structures show different thresholds (Figure 5.34 a-b).

Photoacoustic measurements on two couple of AuNPs and AuNRs with similar structures are presented in Figure 5.34. In particular, in Figure 5.34a) are represented extinction spectra of AuNPs 2 with 21 nm diameter and AuNRs 5 and 25x50 nm, while in Figure 5.34b) AuNPs 4 14 nm and AuNRs 8 21x44 nm respectively.

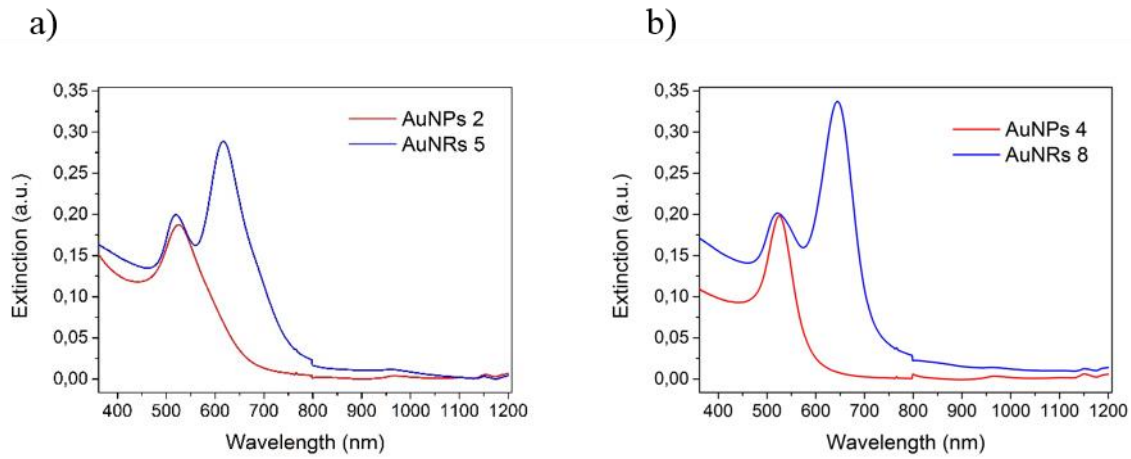

Figure 5.34: Extinction spectra of AuNPs and AuNRs with a) 21 nm and 25x50 nm and b) 14 nm and 21x44 nm respectively

Measurements of AuNPs and AuNRs with the one similar dimension and the presence (or absence) of aggregation show different percentage of absorption.

The shift of the plasmon resonance peak can be different for the two nanostructures and give an additional parameter that has to be controlled.

Table 5.11: Absorption percentage of AuNPs and AuNRs

Sample	***AuNPs 2***	***AuNRs 5***	***AuNPs 4***	***AuNRs 8***
Extinction	0.185	0.194	0.197	0.191
Percentage (%)	87.9	84.5	96.9	92.2

Another important parameter that must be taken into account is the reshaping of the nanorods that can occur with the local increase of temperature[95]. It is obvious that dynamics depend on the time duration of the heating, so probably no strong changes should verify in 300 ms, but this fact must be taken into account.

Gonzàlez et al.[174] demonstrated that the photoacoustic signal is grater for smaller nanoparticles, because the absorption/scattering ratio is higher and this confirms our choice to use small nanoparticles (12-14 nm diameter). We have analyzed two different AuNPs with 14 nm (black dots) and 21 nm (red dots) diameter: our results (Figure 5.35) confirm the decrease of the threshold for smaller AuNPs of previous studies.

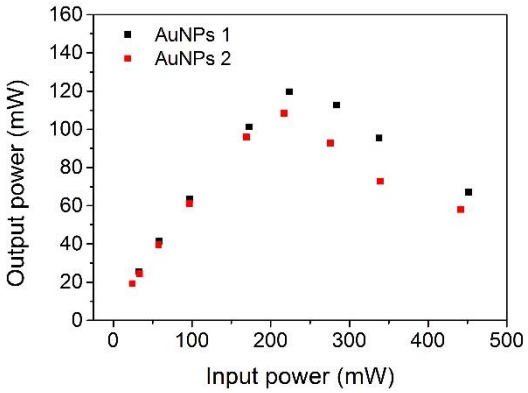

Figure 5.35: Comparison of optical limiting measurements of gold nanoparticles with different diameter in water solvent

This strengthened the idea that to extend the limiting action also in the red region it is more advisable the use of nanorods instead of aggregates of nanospheres that display an higher scattering cross-action, as well as a lower intensity and a broadened peak[175,176].

5.6 Comparison between AuNPs and AuNRs with theoretical model

The interaction between metal nanostructures and incoming light has been studied: a particular attention has been given to the theoretical analysis diffraction patterns generated and the refractive index variation with temperature. We compare our experimental results with the one obtained by PhD Alabastri[177,178], student of prof. Zaccaria Group, who simulated the temperature and the refractive index variation for different input powers.

Starting from polycarbonate matrix parameters, with a beam waist of about 30 um, at 514 nm irradiation wavelength, the temperature and refractive index in the particle environment can be displayed.

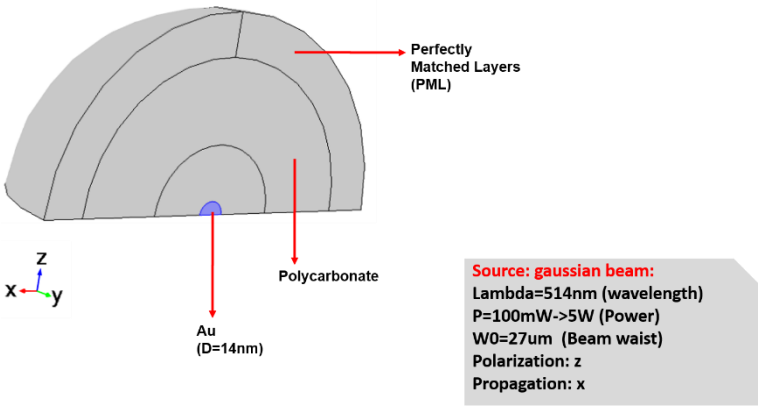

Figure 5.36: Scheme of gold nanoparticle embedded in polycarbonate

Simulated data of temperature and refractive index variation are reported in Figure 5.: the effects of the laser excitation for 100 mW input power (blue line) are visible in a 50 nm radius. We have calculated the distance between two nanoparticles for our concentrations in the approximation of order array distribution, where $r = \sqrt[3]{\left(\frac{1}{n}\right)}$ with $n = \frac{N}{V}$ and determined that the mean value corresponds at 150-200 nm,

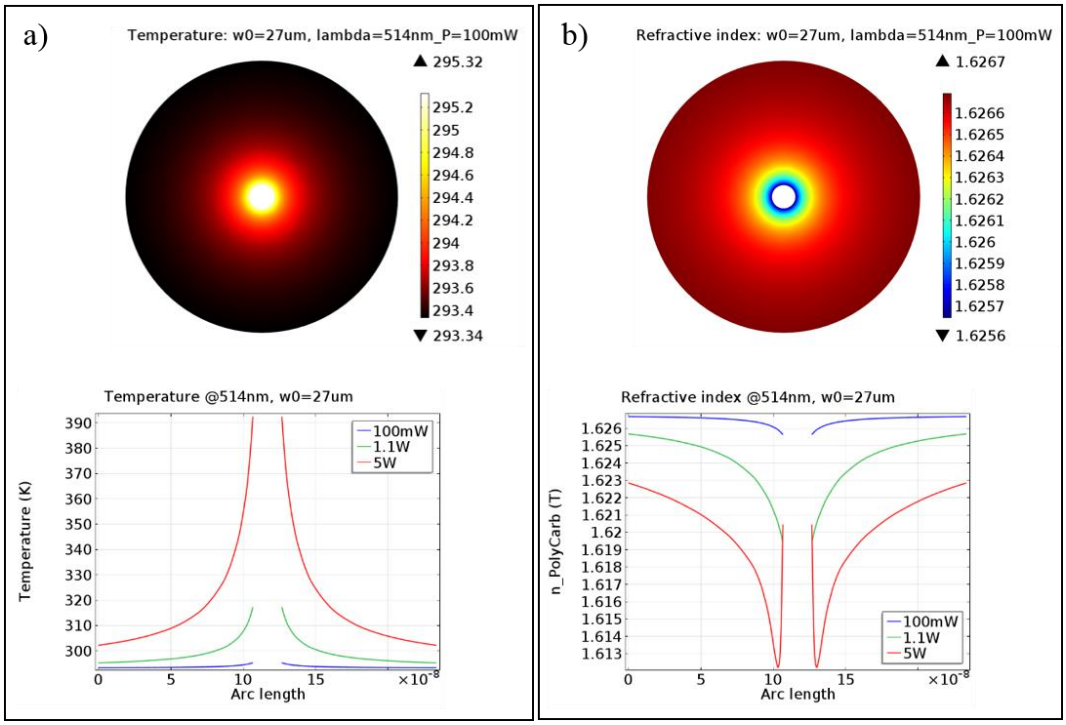

Figure 5.37: Temperature and refractive index simulations on distance: a) 2D color maps at 100 mW input power and b) T and n variation at different input powers

The calculus with the nearest neighbor distribution is more precise and start from the assumption that the mean inter-particle distance is proportional to the size of the per-particle volume $r_{mean} \cong \frac{1}{n^{\frac{1}{3}}}$ where $n = \frac{N}{V}$ is the particle density. If we try to describe the system as a gas with a mean distribution of Nearest Neighbor (NN)[179], we have to consider the probability distribution function:

$$P_N(r)dr = P_{IN}(P_{OUT})^{N-1} \tag{5.6}$$

$$P_{IN} = 4\pi r^2 \frac{N}{V} dr \tag{5.7}$$

$$P_{OUT} = 1 - \frac{4}{3}\pi\frac{r^3}{V} \quad (5.8)$$

Where P_{IN} is the probability to find a particle at the distance d with r<d<dr from the origin while P_{OUT} the probability to find a particle outside that sphere, and if we change with $a = \left(\frac{3}{4\pi n}\right)^{\frac{1}{3}}$, in the approximation of N→ ∞ we can obtain

$$\int_0^\infty \mathrm{P(r)} = \int_0^\infty \frac{3}{a}\left(\frac{r}{a}\right)^2 dr\left(1 - \left(\frac{r}{a}\right)^3 \frac{1}{N}\right)^{N-1} = 1 \quad (5.9)$$

$$r_{mean} \cong 0.893a \quad (5.10)$$

Results obtain in this way are comparable with the approximation of array system. Nanostructures used for our measurements result have a mean distance of 100 nm for AuNPs in CH_2Cl_2 (paragraph 4.6.1), 750 nm for AuNPs functionalized with FULP-SH (paragraph 4.6.2), 200 and 260 nm for AuNPs in PC matrix (paragraph 4.6.3). We can assume that the nanoparticles do not directly interact with one another. Values of thermo-optical coefficient dn/dT for 100 mW input power calculated by this simulation results as $4.8 \cdot 10^{-4}$ K^{-1} and correspond to the one calculated with thermal lens model of $5 \cdot 10^{-4}$ K^{-1} (Table 5.5).

To figure out the rings formation we have tried a simple refractive index change description[180]: if we get a beam passing through this kind of medium variation we can describe the first ring formation.

Following the relation for the description of refractive index changes with an exponential decay

$$n = n0 + dn(1 - e^{\frac{-R}{\alpha}}) \quad (5.11)$$

where n_0 is the linear refractive index, dn the variation, R the radial distance and α the exponential decay constant. Fitting parameters used in this simple simulation are resumed in Table 5.122.

Table 5.12: Fitting parameters for the simulation of an input beam passing through a nanostructure, where N is the photon number, x is the particle distance, PC is the matrix thickness, l is the CCD distance, n_0 is the lower refractive index reached at those temperatures, dn is the refractive index variation, α a is the esponential decay constant, ρ is the radial distance and dt is the integration step.

N	**X**	**PC**	**L (cm)**	**n_0**	**dn**	**α (nm)**	**dt**
4000	350	5000	35	1.612	1.625-n_0	50	0.01 fs

The photons trajectories represented in Figure 5.38 show that the central spot is generated by all the non-interfering photons, while the closer to the nanoparticle the higher the deviation that contributes to the ring formation.

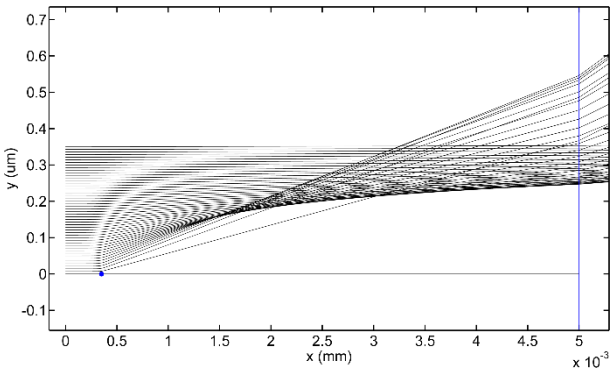

Figure 5.38: Image of photons trajectories deviation after passing through a nanobject with a refractive index variation surrounding

When the beams cross the sample matrix surface (after 5 um in the example in Figure 5.38) they are further deflected: the final absolute rings dimensions will depends also to the CCD camera position (Figure 5.39).

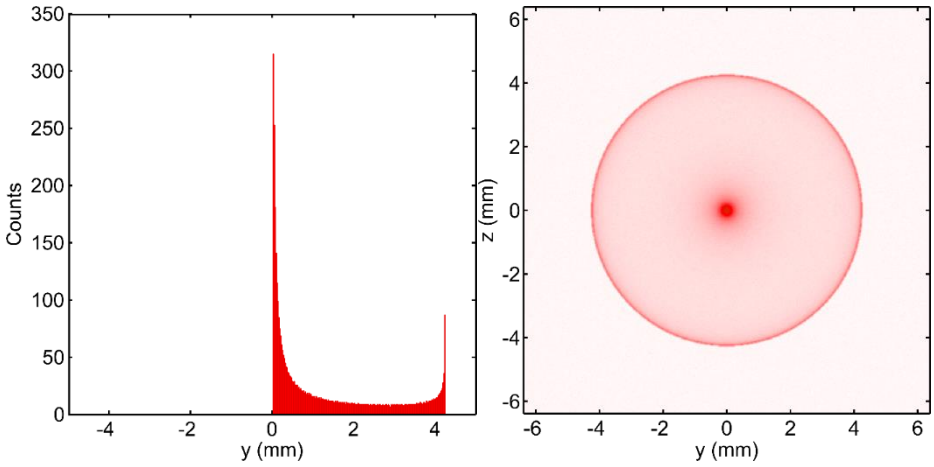

Figure 5.39: Graphs of photon counts vs position represented as a) positive y coordinates and b) circular symmetry

The far-field distribution pattern with multiple rings is obtained considering the free propagation of the optical wave through space, by means of the Fraunhofer approximation of the Fresnel-Kirchhoff diffraction integral[181,182] as

$$I(\rho) = I_0 \left| \int_0^{\infty} J_0(k_0 \theta r) e^{\left[-\frac{r^2}{\omega p^2} - i\phi(r)\right]} r dr \right|^2 \quad (5.12)$$

where ***J0*** (***x***) is the zero-order Bessel function of the first kind, q is the far field diffraction angle, r is the radial coordinate in the far field observation plane. In the paraxial approximation, the distance from the exit plane of the medium and the far-field observation plane, ***D*** , is related to the radial coordinate and the diffraction angle in the far-field are related by r = ***D***q . The parameter $\boldsymbol{I_0}$ is written as

$$I_0 = 4\pi^2 \left| \frac{E(0, z_0 e^{-\frac{\alpha L}{2}})}{i\lambda D} \right|^2 \quad (5.13)$$

When the light beam is convergent, the radius of the wave front curvature is negative, while if the beam is divergent the radius is positive. If the beam is transmitted through the self-defocusing (self-focusing) medium, the nonlinear phase-shift is negative (positive). The two different behaviors can be observed for the far-field patterns in each case, as we have seen in polycarbonate matrix studies (paragraph 5.3).

Chapter 6

6 DISCUSSION

All the analysis we have made give a complete description of linear and nonlinear optical behavior of gold nanostructures. In this Chapter we discuss the results for all the gold nanostructures we have studied and compare them with literature. Finally we will give a description of the performance results of our system and the future perspectives.

6.1 Gold nanospheres in solution and in polymer matrix

We compared nonlinear responses of AuNPs in CH_2Cl_2 solution and in polycarbonate matrix, with the aim of the production of a solid free standing smart material as a candidate for the realization of a protection device. The comparison of the thermo-optical response of solution and of a polycarbonate film doped with AuNPs with comparable absorbance reveals a similarity: they present the same input threshold and comparable optical limiting behavior. This implies that the mechanisms should present some differences. In fact, the nonlinear refractive process is activated by the temperature variation generated by increasing laser irradiances. In the solid sample it produces a local modifications of the PC matrix while in the solution gold nanoparticles release the absorbed energy as solvent heating and bubble generation. This mechanism has been studied in recent works [183,184]: in liquid samples the temperature reached leads to a local solvent bubbling and these scattering centers disperse the beam.
As expected, time responses of solution result faster than film, thanks to refreshing of the surrounding media. However the mean values of output irradiance measured after 300 ms for the film become comparable with the solution owing to the matrix modification that causes a decrease of transmittance.

6.2 Gold nanospheres and core-shells functionalized with fulleropyrrolidine

In order to improve the protective action of these smart materials we decided to combine the thermo-optical process with a faster one, so as to reduce the light intensity that can reach the

eye during an accidental exposure. We functionalized with thiolated-fulleropyrrolidine (FP-SH) two different metal nanostructures: gold nanoparticles for protection at 514 nm irradiation wavelength and silica-gold core-shell active at 647 nm.

Different fulleropyrrolidine molecules have been extensively investigated for optical limiting of nanosecond laser pulses through a reverse saturable absorption (RSA) mechanism [63,82,185,186]: in the case of FP-SH a fast transfer of excited state population to a triplet state with strong excited state absorption activates the RSA mechanism. The fast inter-system crossing and the long lifetime of the triplet state can be exploited to capture part of the energy that would otherwise decay through a slow thermal mechanism and give a faster transmittance reduction compared with the simple thermo-optical process.

As we have seen in the Chapter 3, we preferred polyvinylpirrolidone (PVP) for the transfer of gold nanoparticles in an organic solvent instead of using common thiols[5,56,122], like thiolated-polyethylenglycol (PEG) or dodecanthiol. In this way we promote the subsequent FP-SH functionalization, because PVP, as a steric stabilizer, can be easily displaced by FP-SH molecules and results in a faster and more effective functionalization.

Optical limiting (OL) measurements performed with the sample in a pre-focal position show a nonlinear response of AuNP-S-FP at lower input power compared to AuNPs, with similar linear transmittance. We then performed Z-scan measurements on bare and functionalized AuNPs in order to determine the nonlinear optical parameters: they result in the same order of magnitude as literature reported values[39,40,83]. This suggests a slightly higher nonlinear absorption response for AuNP-S-FP samples, while small differences can be observed for nonlinear refractive index at low input power.

We also collected the temporal responses of the two systems in 300 ms at different input powers. The faster response in first milliseconds (**Errore. L'origine riferimento non è stata trovata.**b) of the thioled nanoparticles results in a lower total fluence compared to the bare ones. To understand the behavior of the two systems we obtain the thermo-optic coefficient by fitting our data with a fixed thermal diffusion coefficient. The value of this parameter decreases in presence of nanostructures with respect to the pure solvent, as confirmed by previous studies[21]. Thermo-optic coefficient (dn/dT) results to be of around 14% higher for the functionalized nanoparticles, comparable with values obtained in closed-aperture Z-scan measurements. This indicates a higher refractive index variation with temperature changes for

AuNP-S-FP and together with the diminishing of the diffusion time, confirms the faster response of the coupled system compared to bare AuNPs.

The Z-scan Analysis (ZSA) and Thermal Lens Model (TLM) analysis discussed above give different information on the nonlinear response of the samples.
A theoretical and experimental comparison between these two models was described by Cuppo et al.[166]. The main difference is that the ZSA starts from the assumption of a local interaction between the radiation field and the sample, while in the TLM the diffusion of heat after the irradiation causes a spatially variation of temperature around the absorbing unit and, consequently, a nonlocal dependence of the refractive index.
The initial motivation of this work was the attempt at combining different mechanisms for OL, in particular, the thermal lens mechanism, already active for bare AuNPs, could be complemented by an enhanced excited state absorption of FP-SH induced by the adjacent AuNP. In the case of FP-SH a fast transfer of excited state population to a triplet state with strong excited state absorption activates the RSA mechanism. The fast inter-system crossing and the long lifetime of the triplet state could be exploited to capture part of the energy that would otherwise decay through a slow thermal mechanism and give a faster transmittance reduction compared with the simple thermo-optical process.
Z-scan measurements allowed us to obtain these nonlinear properties: values of nonlinear absorption coefficient β and nonlinear refraction n_2 show only little differences between AuNPs and AuNP-S-FP samples. These results reveal that the energy transfer mechanism between nanoparticles and FP-SH molecules is not efficient as we expected: probably the high number of molecules bound to a single nanoparticle reduce the energy disposable for the energy transfer.
For this reason z-scan analysis, that is effective for fast local responses, does not provide adequate information to describe the process.
On the contrary, the analysis using the thermal lens model provides a time-dependent description of the transmittance variation. It shows that the phenomenon is still dominated by a simple thermal lens effect as for bare nanoparticles, but a different contribution for the coupled AuNP-S-FP system should be taken into account. It is evident from the results in Table 5.2 that AuNP-S-FP have a faster transmittance decrease in respect to AuNPs, with the outcome of reducing the output power values.

We conclude that the variation of the plasmon resonance wavelength induced by the increase of local temperature[6,187] may be affected by the FP-SH functionalization, causing a different response in the functionalized system.

Our results receive confirmation also in an interesting study carried out on gold nanoparticle in presence of Rodamine 6G[17]: authors reveal the different contribution of these two systems on the thermal dissipation and their interaction under resonant condition. They observed the variation of diffusivity with different relative volume fractions of gold and dye in the mixture and at different concentrations in a pure gold sol: at the lowest power level, the diffusion is four times larger than that of water, which is a very good indicator of the application of this nanofluid as a coolant.

Pure gold solution and the gold–dye mixture show different heat diffusion mechanisms: the former case, the decrease in metal concentration reduces D. They explain this behavior associating as the major thermal decay channel the collision of the metal nanostructures and their Brownian motion. Whereas results obtained in the presence of the dye suggest an energy transfer between the two species and cage formation of the dye around the metal, causing reduction in heat increasing and slowing movements of the system respectively. They obtained similar results also for silver nanoparticles[21].

A recent study by Setoura et al.[92] gives a description of the absorption spectra changes for gold nanoparticles samples after cw irradiation. In particular they show the opposite behavior of solid and liquid samples: a red-shift of gold nanoparticles deposited on a glass substrate in air, and a blue-shift for a colloidal solution in water solvent. These results have been explained by the refractive index gradient of the medium, larger for liquids than for air or glass substrate. In our samples the solvent is CH_2Cl_2 and the main difference between AuNPs and AuNP-S-FP becomes the presence of thiols bound on the surface of nanoparticles, leading to a different power limitation efficiency between AuNPs and AuNP-S-FP.

We have seen in the previous chapter that differences in the optical limiting response of the two systems are due to the fast transmittance decrease in the first 50 ms. We have integrated the output intensities in 300 ms (i.e. fluence) at different input powers and compared the results for AuNPs and AuNP-S-FP.

Similar consideration can be done on gold nanoshells (AuNSs), chosen because of their plasmonic resonance tunable in all the visible and near infrared range. These systems allow a

limitation process at 647 nm irradiation wavelength and could favor an energy transfer more efficient than gold nanoparticles because of the stronger overlapping with the triplet state of fulleropyrrolidine.
The functionalization with FP-SH confirm also in this case the improvements in optical limiting properties, but to obtain threshold values comparable with AuNPs we have to increase the concentration, with a consequent reduction of the linear transmittance. This is because of the low absorption power of AuNSs for high scattering cross section, already verified in our group by photoacoustic measurements[110].

Nonlinear optical measurements show improvements in the OL effect in the functionalized gold nanostructures both in terms of a reduced nonlinear transmission and of a faster response that can be explained only partially by an energy transfer from the excited state of nanoparticles to the triplet state of fulleropyrrolidine. Also TPA mechanism could be considered as possible contributions to decrease output intensity: RSA several studies have shown the activation of TPA[188–191] with cw laser irradiation. A very recent work of Hirata et al. published on Nature Materials describe the activation of RSA[66] process under weak continuous incoherent light. They analyzed matrices doped with a transition-metal complex as a donor and an aromatic species as an acceptor. The efficient formation of long-lived room-temperature triplet excitons in the acceptor species through photosensitization by transition-metal complex donors allows an effective accumulation of the triplet state of the acceptor on irradiation of the films with weak light. These two effects should be considered for a complete description of the optical limiting mechanism, even if as side-processes.
The thermal lens model describes the main process involved in the limiting action: the thermo-optical process. We can see a faster decrease of transmittance for AuNP-S-FP than for AuNPs. The different response in the functionalized system may be ascribed mainly to: (i) a variation of the plasmon resonance wavelength induced by the increase of local temperature[6] affected by the presence of FP-SH molecules, which causes the difference in the n_2 values; (ii) the slightly different value of the thermo optical coefficient. The results obtained for AuNSs indicate an effective strategy for widening the spectral range of operation of optical limiting devices.

6.3 Different concentrations of gold nanostructures in polycarbonate matrix

We made an in depth study of the AuNPs film with different nanostructures concentration and characterize the self-diffraction beam pattern formation during the irradiation.

As we have seen previously the open and closed-aperture Z-scan measurements permit the determination of an effective nonlinear absorption coefficient and of the nonlinear refractive index, respectively. The values of β are given by different mechanisms: the nonlinear absorption of the AuNPs embedded in the matrix and the absorption variation due to the increase of temperature in the environment that causes changes in the refractive index that affect the plasmon resonance. This very last consideration has been examined by Doremus[192]: he has shown that on increasing the sample temperature the plasmon absorption band broadens and the resonance peak slightly red shifts. The different heating effects and refractive index changes may well explain the nonlinear absorption and its dependence on irradiation wavelength and power. As expected, the β values are consistently larger for more concentrated AuNPs sample. The hysteresis in the open-aperture configuration highlighted in the previous Chapter suggest some laser induced matrix modification when the irradiance reaches high values. The PC matrix does not show nonlinear behavior even at the highest energies used: the data indicate that there is no nonlinear absorption contribution nor laser damage. We must refer to the interaction between the nanostructures surface and the polymeric environment. In particular for gold nanoparticles in matrix the process involved are different: reverse saturable absorption, changes in absorption values due to increasing temperature and local melting of the polymer matrix. In previous studies conducted in our group, gold core-shell irradiated with femtosecond laser pulses showed saturable absorption and variation of nonlinear absorption coefficient for different input fluencies [193]. Clearly, the mechanisms underlying nonlinear absorption of cw radiation are quite different.

Our results are compared with those for gold nanoparticles in different solvents: Jia[136] and Nadjari[100] studied gold nanoparticles colloids in water and the obtained nonlinear refractive index values of around 10^{-7} W/cm^2, one order of magnitude less than ours (Table 5.5). The thermally induced nonlinear refractive index depends on dyes concentration, absorbance values and laser irradiation wavelengths, so n_2 can change more than one order of magnitude, as shown by differences in results obtained by Nadjari[100] and Majles Ara[40]. Furthermore, in the polymer matrix melting and irreversible changes may occur (*vide infra*).

Sarkhosh studied AuNPs stabilized with cyclohexanone[39] in castor oil[83], obtaining values of dn/dT comparable with our results. However, direct comparison should be considered with caution since the values obtained are dependent on many different factors such as the NP concentration and the thermal and thermo-optical properties of the medium.
As already mentioned, spatial self-phase modulation may generate diffraction patterns in nonlinear media[83–85]. To rule out the possibility that the optical nonlinearity may arise from the polymer matrix as such, a blank polymer without nanoparticles was measured under the same conditions. No diffraction pattern was seen in the pre-focal position even at high input energy.

CW measurements show that the nonlinear absorption depends mainly on a thermal effect. The induced spatial temperature gradient changes the refractive index across the sample that acts as a lens[39]. We have observed in the dynamic rings formation during a time interval of 300 ms for different irradiation powers. The nonlinear refractive process is activated by the temperature variation generated by increasing laser irradiances: gold nanoparticles release the absorbed energy as solvent heating. As we will explain later this rings formation could be useful for optimizing the geometrical configuration of the final protection device. A systematic study of the number and dimension of rings in a specific time interval could help for the further reduction of output energy: a starting point is represented by a theoretical description of the process[171].We have done another interesting consideration on the configuration of the optical system: we have seen different diffraction images formed if the sample is positioned in the pre- or post-focal position. In the first case we see concentric rings with a central bright spot while after the focus it is visible a dark spot in the middle. This result depends on the different response of a self-defocusing material when irradiated with a convergent (pre-focal position) or divergent (post-focal position) beam[171]. We can have a stronger reduction of the output energy only by changing the setup of the protection device fixing the active material in a post-focal position.
Clearly, to optimize the protection the choices of the position of the active material and of the sensor in the focusing system are critical.
Other works based on polymer films do not consider the temperature variation induced in the matrix by dyes absorption. This is a crucial point in the nonlinear response of the sample. Only Mathews[134] notice the damage of the matrix. The rings formation appear at higher temperatures than the polycarbonate glass temperature (160 °C), causing irreversible changes in the polymer microstructure that are the likely origin of the hysteresis observed on cycling the irradiance, as

confirmed by the irregular shape of the central spot of the diffraction pattern recorded for irradiance values above the nonlinear threshold.
However, this phenomenon does not hamper the use of polymer composite materials for protection devices since it is unlikely that cw beams hit the device consecutively in exactly the same position.
We have calculated the exposure limits for visible light defined by the ANSI Z-136.1[103] and the major limitation that still hampers a practical use of the studied polymer films is the slow dynamics for decreasing the transmittance down to the plateau value. For obtaining faster responses, one should improve the photophysics of the active species, the thermo-optical properties of the matrix, or both. Further considerations are discussed in Paragraph 6.7.

In polycarbonate films, as we have seen for the liquid sample, Z-scan measurements revealed a large thermally-induced negative refractive index n_2 in the range of 10^{-6} cm^2/W, and thermo-optical coefficients dn/dT of 10^{-4} K^{-1}. The optical limiting responses of these nanostructures are dominated by a nonlinear refraction mechanism and the dynamics of transmittance changes and diffraction pattern images, owing to self-phase modulation, were recorded in order to study the response of AuNPs doped thin films. A local damage of the polymer films was revealed and attributed to heating above the melting temperature caused by the transfer of the energy absorbed by the AuNPs to the matrix.
The AuNPs doped polymer films hold promise for application in disposable optical limiters for eye protection against damage induced by cw lasers. The nonlinear transmittance is remarkably reduced to low levels within a typical blinking time of 300 ms. However, to be suitable for practical application, improvements are still needed to obtain a faster response and an effective limitation also with higher linear transmittance. Such improvements can be accomplished by investigating different matrices with higher thermal conductivity and thermal expansion coefficient and higher thermal resistance. The results reported in this paragraph suggest a suitable procedure for a thorough characterization of materials for cw optical limiting applications with an appropriate emphasis placed on the response dynamics.

As we have said before one of the main requirements for a good optical limiting material is the wide broadband activity that we have achieved with nanorods, promising for their tunable longitudinal plasmon peak and their high absorption coefficient. A first analysis of AuNRs

solutions confirmed the nonlinear refraction behavior at different positions along the beam direction. Results are in agreement with the ones obtained for gold nanoparticles.

We tried to compare optical limiting measurements of AuNRs with different aspect ratio obtained by different syntheses and ageing of the solutions. We have revealed very different behaviors because of the reshaping process and the different scattering components, confirmed by the photoacoustic measurements.

We identify AuNRs as a promising choice for efficient optical limiting at 647 nm irradiation wavelength. Nevertheless, if we desire a broadband protection, we have to balance activity at 514 nm also: an excessively high aspect ratio can cause a diminishing in the intensity of the transversal peak. This problem could be solve joined AuNRs and AuNPs but stabilization of the mixed sample it is difficult. A solution could be the embedding of both structures in the polymer matrix after the functionalization and solvent redispersion (Paragraph 3.3.2). Preliminary studies on optical limiting properties of AuNRs in polycarbonate matrix are similar to the one obtained for AuNPs in PC and encourage additional in-depth analysis.

6.4 Gold nanoparticles in silk matrix

In order to try different embedding matrix for gold nanostructures, we conducted OL measurements at 514 nm on water-soluble silk fibroin to simplify the embedding of AuNPs. Thanks to its good biocompatible silk fibroin could be a useful matrix for different applications[41,51,142,194–196].

Optical limiting measurements of AuNPs in silk matrix reveal differences depending also on the deposition method, confirmed by TGA: different substrate contribute to the formation of distinct organization of silk fibers and a consequent different stability increasing temperature.

These results persuade us to think that a specific conformation of the fibers can produce a stronger nonlinear response.

High irradiances produce a modification of the matrix and the presence of a melting process is confirmed by microscope analysis. The matrix degradation is not a limit for the final aim of a protection device: as we have described in Chapter 1 it will be compromised only a single spot. In this case, the fibers structure induce an increase of the limiting threshold and an immediate matrix destruction. The matrix get thinner and cause an increase of output transmittance, in same cases higher than the linear one. We can conclude that polycarbonate remain the better performing matrix for optical limiting application.

However these studies could be useful for different application, for example for lasing where the matrix degradation has to be controlled and where it is indispensable a good optical quality of the film. In this direction, preliminary studies have been conducted by the group of Zamboni et al.[149] using our deposition techniques.
The very high stability of AuNPs in fibroin matrix could be used for sensing: in fact porous matrix can be easily obtain by the addition of organic solvents. First SERS studies conducted on Malachite Green, a common pesticide, in these matrices show the signal of the molecule but further improvement should be done on the matrix production parameters.

6.5 Comparison between AuNPs and AuNRs with photoacoustic technique

In order to discriminate absorption and scattering contribution of the nanostructures solutions, we have used photoacoustic measurements. First of all this analysis helps us to understand how nanoparticles increase the limiting process in respect with a classical absorptive medium as an organic or inorganic molecule. Results on AuNPs and $KMnO_4$ with the same extinction at 532 nm reveal a better OL behavior of the nanoparticles, although they present less absorption contribution. In particular the photoacoustic signal leads to a heat conversion percentage, calculated in 93.5% for AuNPs and 86.9% for AuNRs, in respect of the $KMnO_4$. This is a confirmation of the improvements given by the nanostructured system instead of simply absorbing molecules: not only absorption contributes at the density change and consequent the refractive index change.
We also compared results obtained for AuNPs and AuNRs. An interesting study of plasmonic nanostructures analyzed with photoacoustic measurements describe laser induced processes in solution that lead to bubble production to study the dynamics of bubble formation and decay[197]. A similar description can be given to justify the great refractive index variation in our systems. Several studies deal with gold nanoparticles reaction after high intensity irradiations, describing the different changes in the structures and their environment[43]. All these results confirm that NL optical effects are not due only to the absorption and thermal relaxation, but also to a local heating caused by a high plasmon resonance that amplify the phenomenon.

The comparison with photoacoustic measurements confirms previous observations, assigning a partial contribution to NL absorption and refraction, also revealed by z-scan measurements.

These systems can be also sensitive to the changes in extinction profiles due to the local increase of temperature: geometry, matrices and irradiation wavelengths can influence the absorption peak variation, leading to different effectiveness in power limiting. Recently Setoura et al.[92] have given a theoretical and experimental description of gold nanoparticles reshaping after irradiation. Significant variations in extinction profile have been observed at high input irradiance, of around 1 mW/μm^2, 10^3 times greater than ours. Nevertheless gold nanoparticles studied in their work have 150 nm diameters, an order of magnitude higher than ours, with a consequent greater scattering and lower absorption efficiency. A similar behavior can be expected for our systems but it would require a specific study.

Measurements of AuNPs and AuNRs with the one similar dimension and the presence (or absence) of aggregation show different percentage of absorption. The shift of the plasmon resonance peak can be different for the two nanostructures and give an additional parameter that has to be controlled.

Another important parameter that must be taken into account is the reshaping of the nanorods that can occur with the local increase of temperature[95]. It is obvious that dynamics depend on the time duration of the heating, so probably no strong changes should verify in 300 ms, but this fact must be taken into account.

Gonzàlez et al.[174] demonstrated that the photoacoustic signal is grater for smaller nanoparticles, because the absorption/scattering ratio is higher and this confirms our choice to use small nanoparticles (12-14 nm diameter). Our results on AuNPs with two different diameters confirm the decrease of the threshold for smaller AuNPs of previous studies.

This strengthened the idea that to extend the limiting action also in the red region it is more advisable the use of nanorods instead of aggregates of nanospheres that display an higher scattering cross-action, as well as a lower intensity and a broadened peak[175,176].

6.6 Comparison between AuNPs and AuNRs with theoretical model

The interaction between metal nanostructures and incoming light has been studied: a particular attention has been given to the theoretical analysis diffraction patterns generated by this interaction[171,182,198], as much as the refractive index variation with temperature[92,166,199]. An interesting study shows the difference between the images caused by a converging (or diverging) beam passing through a self-defocusing material: theoretical patterns are similar to those obtained with our nanostructures. Theoretical simulation of the interaction of a gold

nanoparticles embedded in polycarbonate matrix conducted by PhD Alabastri[177,178], student of prof. Zaccaria Group, allow us to have a complete description of the temperature and the refractive index variation for different input powers. The temperature variation during the 300 ms irradiation interval cause the rings position and thickness modification. Moreover the formation of another phase (bubbling) create an additional interface that further spread the beam. A few articles try to give a theoretical description of this phenomenon for different application fields, from chemical reactions to medical treatments[18,197,199,200].

This experiment also suggests that the nanoparticles do not directly interact with one another. The comparison with experiments does not perfectly match because the theoretical results refer to an equilibrium state while our measurements are collected in a dynamic range. It is clear that the global effect generating optical limiting is due to a collective contribution of different nanoparticles. Thermal measurements conducted by Richardson et al. on a droplet containing gold nanoparticles[97] determine the efficacy of converting absorbed energy into heat. They detected small "bumps" in temperature located around single optically stimulated NPs, but they revealed a sizable overall increase in the temperature of the droplet is observed due to a collective heating effect of many NPs within the excitation volume, $V_{beam}n_{NP} \sim 10^7$.

This result confirm the collective contribution of an ensemble of nanoparticles to the final optical limiting behavior.

6.7 Performance results of our system and perspectives

In this paragraph are summarized all the requirements that a protection device should have and the way we have chosen to improve the properties.

We said that a good protection device should be active in the widest visible range in order to protect the operator from unpredictable radiation wavelength. This wide operation range has been obtained studying different nanostructures: gold nanospheres provide high nonlinear absorbance for green radiations while core-shells show a better effectiveness in the red region. Gold nanorods present interesting intermediate properties between the two previous systems, with their transversal and longitudinal tunable resonances. In this way it could be possible to be protect from the most common laser pointer wavelengths in the green and red regions at 514-532-633-647 nm.

These structures are functionalizable with organic molecules and thus allow us to improve the system response rate. The thioled-fulleropyrrolidine reduces the response time of around 20%,

decreasing the total fluence that reaches the sensor in the first 300 ms, time required for the blinking of an eye. The starting idea of the energy transfer from the nanoparticles to the triplet state of the FP did not show the desired efficacy, but TPA processes combined with the plasmon peak shift due to the environment variation, induce a stronger limitation effect. A future perspective could be the functionalization of metal nanostructures with thermochromic molecules in order to convert the heat release at high irradiances in conformational changes and to increase the energy that can be absorbed[201–203]. These conformational changes correspond to a variation in the extinction spectra of the thermochromic molecules and can lead to an enhancement of the absorbed radiation.

One of the desirable property is the manufacturing of a solid-state device. Polycarbonate has high optical quality and good mechanical strength, and for these reasons it is usually the preferred substance for use in lenses for goggles. In order to combine our nanostructures with this polymer, we optimized and achieved an efficient solvent transfer of gold nanostructures from aqueous solution to organic solvents. Films have been obtained from homogeneous solution by casting process. Another important requirement is the high transmittance that has been tested comparing our films with the photopic and scotopic curves that describe the physiological response of the eye in light and dark condition respectively. We have reached desirable low optical limiting activation thresholds with linear transmittance films of around 50-60%, higher than 40% required by the ANSI[164].

For the protection against cw laser the Maximum Permissible Exposure (MPE) has been evaluated as 0.3 mJ (see the equation in paragraph 4.6.3). Our films in the actual configuration provide a protection of 2 orders of magnitude lower than the one required. This detail can be overcome with an appropriate geometrical configuration: we have demonstrate that the post focal position of the active material reduce the output irradiance by 20%. The presence of the iris of the eye can reduce the total amount of the output irradiance by more than 50%. We can further reduce the linear transmittance until the 40% threshold and decreasing the output irradiances of another 20%.

So it is possible to reduce the fluence that reaches the sensor to 7 mJ/cm^2, only one order of magnitude higher than the value required.

The presence of organic molecules with nonlinear properties reduce the final transmittance by another 12%: this should have been studied also in polymer matrix but these promising results

together with the possibility of thermochromic functionalization suggest an additional transmittance reduction.

High irradiances generate high local temperature that induced the matrix degradation. The most promising future perspective of this work is to develop a device in which the active material is sandwiched between two polymeric microlenses arrays, already manufactured and described both in articles[204–210] and in patents[211–213]: for various applications: in this case only a single spot will be damaged not compromising the rest of the device.

Chapter 7

7 CONCLUSIONS

In this work we have studied the optical limiting properties of different gold nanostructures in solution and polymer matrices in order to obtain a protection device against cw laser radiations. We started from the synthesis of gold nanospheres and then studied different shapes like nanoshells and nanorods to achieve tunable plasmon band in the visible and near infrared regions. These systems have been widely characterized: the TEM and DLS gave information on dimensions and morphology, while UV-Vis absorption, Z-scan and Optical Limiting measurements determined the linear and nonlinear optical properties.

In order to enhance linear and nonlinear optical properties of molecules in resonance conditions we have defined an efficient strategy to transfer nanostructures from water to organic solvent. This process also allow embedding the colloidal solution in polycarbonate matrix. We have chosen a thioled-fulleropyrrolidine to improve the temporal response of our systems though nonlinear processes like TPA and RSA, already known in literature. In our case a fast transfer of excited state population to a triplet state with strong excited state absorption could activate the RSA mechanism.

The fast inter-system crossing and the long lifetime of the triplet state can be exploited to capture part of the energy that would otherwise decay through a slow thermal mechanism and give a faster transmittance reduction compared with the simple thermo-optical process. We combined the thermal process with a faster one, to allow a stronger reduction of transmittance and a better limiting efficiency. We have proved the functionalized AuNPs to be effective for OL through a quite different mechanism that is activated in a much shorter time. This effect is a set of various mechanism: the change in the environment of the nanoparticles with a consequent resonance shift; the variation in the thermalizing process due to the presence of bonded molecules on the surface; TPA and RSA mechanism favoured by the energy transfer between nanoparticles and fulleropyrrolidine.

OL measurements have been conducted on gold nanoparticles embedded in polycarbonate with promising results that have been compared to the colloidal solutions. In order to study the matrix effect and to obtain easier embedding process we have also studied AuNPs in silk fibroin matrix. Silk fibroin in aqueous solution shows a high miscibility with AuNPs without functionalization process needed for the stabilization in organic solvent necessary for embedding in PC matrix. Preliminary studies discourage the use of this system for OL but different application could be considered. Furthermore, due to its biocompatibility and its gradual solubility, it can be used in different applications, for instance in the controlled release of drugs.

Finally we tried to compare thermal properties revealed by our systems through cw laser excitation to nonlinear optical properties classically expressed by pulsed laser excitation. OL related to photoacoustic measurements permitted us to discriminate between the absorption and scattering contributions and to identify the best system with the higher transmittance and the lower threshold desired. Moreover, preliminary studies based on simulations allowed us to describe the interaction between metal nanostructures and cw laser irradiation, to get the description of the refractive index variation. In detail, we have defined that the phenomenon is mainly due to heat transfer from the nanostructures to the environment, but with attention to details in the dye-matrix interaction it is possible to improve the performance. This kind of interaction has recently become a hot topic because of the different applications, in particular in medical field for cancer treatment and in solar energy conversion.

In conclusion we have obtained an optical limiting device with broadband activity through gold nanospheres, nanoshells and nanorods. For the realization of a solid-state device we have chosen polycarbonate matrix. The high linear transmittance has been reached thanks also to the homogeneity of the embedding and the fast temporal response through the functionalization of the system. Consideration on the geometrical configuration of the system help us to get an improvement of the final device.

BIBLIOGRAPHY

1. Feynmann, R. There's a plenty of room at the bottom. *Eng. Sci.* **23,** 22–36 (1960).

2. Gao, Y. *et al.* Size effect of optical limiting in gold nanoparticles. *Chem. Phys.* **336,** 99–102 (2007).

3. Gao, J. & Xu, M. Metal Nanopaticles of Various Shapes. 1–19

4. Larosa, C., Stura, E., Eggenhöffner, R. & Nicolini, C. Optimization of Optical Properties of Polycarbonate Film with Thiol Gold-Nanoparticles. *Materials (Basel).* **2,** 1193–1204 (2009).

5. Liu, X., Atwater, M., Wang, J. & Huo, Q. Extinction coefficient of gold nanoparticles with different sizes and different capping ligands. *Colloids Surf. B. Biointerfaces* **58,** 3–7 (2007).

6. Link, S. & El-Sayed, M. A. Size and Temperature Dependence of the Plasmon Absorption of Colloidal Gold Nanoparticles. *J. Phys. Chem. B* **103,** 4212–4217 (1999).

7. Link, S. & El-Sayed, M. a. Shape and size dependence of radiative, non-radiative and photothermal properties of gold nanocrystals. *Int. Rev. Phys. Chem.* **19,** 409–453 (2000).

8. Shahriari, E., Yunus, W. M. M. & Saion, E. Effect of particle size on nonlinear refractive index of Au nanoparticle in PVA solution. *Brazilian J. Phys.* **40,** 256–260 (2010).

9. Zhang, J. Z. & Noguez, C. Plasmonic Optical Properties and Applications of Metal Nanostructures. *Plasmonics* **3,** 127–150 (2008).

10. Link, S. & El-Sayed, M. a. Size and Temperature Dependence of the Plasmon Absorption of Colloidal Gold Nanoparticles. *J. Phys. Chem. B* **103,** 4212–4217 (1999).

11. Govorov, A. O. & Richardson, H. H. Generating heat with metal nanoparticles We describe recent studies on photothermal effects using colloidal. *Nano Today* **2,** 30–38 (2007).

12. Yoon, J. H. & Yoon, S. Photoisomerization of azobenzene derivatives confined in gold nanoparticle aggregates. *Phys. Chem. Chem. Phys.* **13,** 12900–5 (2011).

13. Thomas, K. G., Zajicek, J. & Kamat, P. V. Surface Binding Properties of Tetraoctylammonium Bromide-Capped Gold Nanoparticles. *Langmuir* **18,** 3722–3727 (2002).

14. Lukianova-Hleb, E. Y. & Lapotko, D. O. Influence of transient environmental photothermal effects on optical scattering by gold nanoparticles. *Nano Lett.* **9,** 2160–6 (2009).

15. Hashimoto, S., Werner, D. & Uwada, T. Studies on the interaction of pulsed lasers with plasmonic gold nanoparticles toward light manipulation, heat management, and nanofabrication. *J. Photochem. Photobiol. C Photochem. Rev.* **13,** 28–54 (2012).

16. Gaiduk, A., Ruijgrok, P. V, Yorulmaz, M. & Orrit, M. Making gold nanoparticles fluorescent for simultaneous absorption and fluorescence detection on the single particle level w. 149–153 (2011). doi:10.1039/c0cp01389g

17. Ani Joseph, S. *et al.* Photothermal Characterization of Nanogold Under Conditions of Resonant Excitation and Energy Transfer. *Plasmonics* **5,** 63–68 (2010).

18. Pustovalov, V. K., Smetannikov, a. S. & Zharov, V. P. Photothermal and accompanied phenomena of selective nanophotothermolysis with gold nanoparticles and laser pulses. *Laser Phys. Lett.* **5,** 775–792 (2008).

19. Jiménez-Pérez, J. L. *et al.* Thermal Characterization of Solutions Containing Gold Nanoparticles at Different pH Values. *Int. J. Thermophys.* **34,** 955–961 (2012).

20. Qu, S., Du, C., Song, Y., Wang, Y. & Gao, Y. Optical nonlinearities and optical limiting properties in gold nanoparticles protected by ligands. *Chem. Phys. Lett.* **356,** 403–408 (2002).

21. Ani Joseph, S. *et al.* Thermal diffusivity of rhodamine 6G incorporated in silver nanofluid measured using mode-matched thermal lens technique. *Opt. Commun.* **283,** 313–317 (2010).

22. Patel, H. E. *et al.* Thermal conductivities of naked and monolayer protected metal nanoparticle based nanofluids: Manifestation of anomalous enhancement and chemical effects. *Appl. Phys. Lett.* **83,** 2931 (2003).

23. Frare, M. C. *et al.* Fullerene functionalized gold nanoparticles for optical limiting of continuous wave laser. *PCCP* Submitted (2014).

24. Hartland, G. V. & Schatz, G. Virtual Issue: Plasmon Resonances - A Physical Chemistry Perspective. *J. Phys. Chem. C* **115,** 15121–15123 (2011).

25. Eustis, S. & el-Sayed, M. a. Why gold nanoparticles are more precious than pretty gold: noble metal surface plasmon resonance and its enhancement of the radiative and nonradiative properties of nanocrystals of different shapes. *Chem. Soc. Rev.* **35,** 209–17 (2006).

26. Ghosh, S. K. & Pal, T. Interparticle coupling effect on the surface plasmon resonance of gold nanoparticles: from theory to applications. *Chem. Rev.* **107,** 4797–862 (2007).

27. Kamat, P. V. Meeting the Clean Energy Demand: Nanostructure Architectures for Solar Energy Conversion. *J. Phys. Chem. C* **111,** 2834–2860 (2007).

28. Oelhafen, P. & Schüler, a. Nanostructured materials for solar energy conversion. *Sol. Energy* **79,** 110–121 (2005).

29. Pillai, S. & Green, M. a. Plasmonics for photovoltaic applications. *Sol. Energy Mater. Sol. Cells* **94,** 1481–1486 (2010).

30. Atwater, H. a & Polman, A. Plasmonics for improved photovoltaic devices. *Nat. Mater.* **9,** 205–13 (2010).

31. Matheu, P., Lim, S. H., Derkacs, D., McPheeters, C. & Yu, E. T. Metal and dielectric nanoparticle scattering for improved optical absorption in photovoltaic devices. *Appl. Phys. Lett.* **93,** 113108 (2008).

32. Hägglund, C. & Kasemo, B. Nanoparticle plasmonics for 2D-photovoltaics: mechanisms, optimization, and limits. *Opt. Express* **17,** 11944–57 (2009).

33. Chen, F.-C. *et al.* Plasmonic-enhanced polymer photovoltaic devices incorporating solution-processable metal nanoparticles. *Appl. Phys. Lett.* **95,** 013305 (2009).

34. Kuwauchi, Y., Yoshida, H., Akita, T., Haruta, M. & Takeda, S. Intrinsic catalytic structure of gold nanoparticles supported on TiO2. *Angew. Chem. Int. Ed. Engl.* **51,** 7729–33 (2012).

35. Stratakis, M. & Garcia, H. Catalysis by supported gold nanoparticles: beyond aerobic oxidative processes. *Chem. Rev.* **112,** 4469–506 (2012).

36. Tian, Y. & Tatsuma, T. Plasmon-induced photoelectrochemistry at metal nanoparticles supported on nanoporous TiO2. *Chem. Commun.* **16,** 1810–1 (2004).

37. Frare, M. C., Weber, V., Signorini, R. & Bozio, R. Gold nanoparticles in a polycarbonate matrix for optical limiting against a CW laser. *Laser Phys.* **24,** 105901 (2014).

38. Polavarapu, L., Venkatram, N., Ji, W. & Xu, Q.-H. Optical-limiting properties of oleylamine-capped gold nanoparticles for both femtosecond and nanosecond laser pulses. *ACS Appl. Mater. Interfaces* **1,** 2298–303 (2009).

39. Sarkhosh, L., Aleali, H., Karimzadeh, R. & Mansour, N. Large thermally induced nonlinear refraction of gold nanoparticles stabilized by cyclohexanone. *Phys. Status Solidi* **207,** 2303–2310 (2010).

40. Majles Ara, M. H. *et al.* Diffraction patterns and nonlinear optical properties of gold nanoparticles. *J. Quant. Spectrosc. Radiat. Transf.* **113,** 366–372 (2012).

41. Jia, L., Guo, L., Zhu, J. & Ma, Y. Stability and cytocompatibility of silk fibroin-capped gold nanoparticles. *Mater. Sci. Eng. C. Mater. Biol. Appl.* **43,** 231–6 (2014).

42. Boisselier, E. & Astruc, D. Gold nanoparticles in nanomedicine: preparations, imaging, diagnostics, therapies and toxicity. *Chem. Soc. Rev.* **38,** 1759–82 (2009).

43. Qin, Z. & Bischof, J. C. Thermophysical and biological responses of gold nanoparticle laser heating. *Chem. Soc. Rev.* **41,** 1191–217 (2012).

44. Zharov, V. P., Galitovsky, V. & Viegas, M. Photothermal detection of local thermal effects during selective nanophotothermolysis. *Appl. Phys. Lett.* **83,** 4897 (2003).

45. Chen, P. C., Mwakwari, S. C. & Oyelere, A. K. Gold nanoparticles: From nanomedicine to nanosensing. *Nanotechnol. Sci. Appl.* **1,** 45–65 (2008).

46. Homola, J., Yee, S. S. & Gauglitz, G. Surface plasmon resonance sensors: review. *Sensors Actuators B Chem.* **54,** 3–15 (1999).

47. Hong, S., Lee, S. & Yi, J. Sensitive and molecular size-selective detection of proteins using a chip-based and heteroliganded gold nanoisland by localized surface plasmon resonance spectroscopy. *Nanoscale Res. Lett.* **6,** 336 (2011).

48. Loo, C., Lowery, A., Halas, N., West, J. & Drezek, R. Immunotargeted nanoshells for integrated cancer imaging and therapy. *Nano Lett.* **5,** 709–11 (2005).

49. Huang, X., Neretina, S. & El-Sayed, M. a. Gold Nanorods: From Synthesis and Properties to Biological and Biomedical Applications. *Adv. Mater.* **21,** 4880–4910 (2009).

50. Hirsch, L. R. *et al.* Nanoshell-mediated near-infrared thermal therapy of tumors under magnetic resonance guidance. *Proc. Natl. Acad. Sci. U. S. A.* **100,** 13549–54 (2003).

51. Lin, Y. *et al.* Genetically Programmable Thermoresponsive Plasmonic Gold/Silk-Elastin Protein Core/Shell Nanoparticles. *Langmuir* **30,** 4406–4414 (2014).

52. Huang, X., El-Sayed, I. H., Qian, W. & El-Sayed, M. a. Cancer cell imaging and photothermal therapy in the near-infrared region by using gold nanorods. *J. Am. Chem. Soc.* **128,** 2115–20 (2006).

53. Chen, H., Shao, L., Li, Q. & Wang, J. Gold nanorods and their plasmonic properties. *Chem. Soc. Rev.* **42,** 2679–724 (2013).

54. Huang, X., Jain, P. K., El-Sayed, I. H. & El-Sayed, M. a. Plasmonic photothermal therapy (PPTT) using gold nanoparticles. *Lasers Med. Sci.* **23,** 217–28 (2008).

55. Dickerson, E. B. *et al.* Gold nanorod assisted near-infrared plasmonic photothermal therapy (PPTT) of squamous cell carcinoma in mice. *Cancer Lett.* **269,** 57–66 (2008).

56. Thierry, B., Ng, J., Krieg, T. & Griesser, H. J. A robust procedure for the functionalization of gold nanorods and noble metal nanoparticles. *Chem. Commun. (Camb).* **1,** 1724–6 (2009).

57. Chen, J. *et al.* Immuno gold nanocages with tailored optical properties for targeted photothermal destruction of cancer cells. *Nano Lett.* **7,** 1318–22 (2007).

58. Tong, L. *et al.* Gold Nanorods Mediate Tumor Cell Death by Compromising Membrane Integrity. *Adv. Mater.* **19,** 3136–3141 (2007).

59. Mie, G. Beiträge zur optik trüber medien speziell kolloidaler metalllösungen. *Ann. Phys.* **330,** 377–445 (1908).

60. Mie, G. A contribution to the optics of turbid media, especially colloidal metallic suspensions. *Ann. Phys.* **25,** (1908).

61. Shuang, Z., Peng, W., Peiji, W., Peiwang, Z. & Cheng, Y. Investigation of optical limiting of organic complex sample. *Synth. Met.* **121,** 1471–1472 (2001).

62. Rajashekar, B., Limbu, S., Aditya, K., Nageswara Rao, G. & Siva Sankara Sai, S. Azo doped polymer thin films for active and passive optical power limiting applications. *Photochem. Photobiol. Sci.* **12,** 1780–6 (2013).

63. Signorini, R. *et al.* Optical limiting and non linear optical properties of fullerene derivatives embedded in hybrid sol–gel glasses. *Carbon N. Y.* **38,** 1653–1662 (2000).

64. Ramakrishna, G., Varnavski, O., Kim, J., Lee, D. & Goodson, T. Quantum-sized gold clusters as efficient two-photon absorbers. *J. Am. Chem. Soc.* **130,** 5032–3 (2008).

65. Amendola, V., Mattei, G., Cusan, C., Prato, M. & Meneghetti, M. Fullerene non-linear excited state absorption induced by gold nanoparticles light harvesting. *Synth. Met.* **155,** 283–286 (2005).

66. Hirata, S., Totani, K., Yamashita, T., Adachi, C. & Vacha, M. Large reverse saturable absorption under weak continuous incoherent light. *Nat. Mater.* **13,** 938–46 (2014).

67. Gordon, J. P., Leite, R. C. C., Moore, R. S., Porto, S. P. S. & Whinnery, J. R. Long-Transient Effects in Lasers with Inserted Liquid Samples. *J. Appl. Phys.* **36,** 3 (1965).

68. Leite, R. C. C. THE THERMAL LENS EFFECT AS A POWER-LIMITING DEVICE. *Appl. Phys. Lett.* **10,** 100 (1967).

69. Chon, B. J. W. M., Bullen, C., Zijlstra, P. & Gu, M. Spectral Encoding on Gold Nanorods Doped in a Silica Sol – Gel Matrix and Its Application to High-Density Optical Data Storage **. *Adv. Drug Deliv. Rev.* **17,** 875–880 (2007).

70. Hogan, N. J. *et al.* Nanoparticles Heat through Light Localization. *Nano Lett.* **14,** 4640–4645 (2014).

71. Heber, A., Selmke, M. & Cichos, F. Metal nanoparticle based all-optical photothermal light modulator. *ACS Nano* **8,** 1893–8 (2014).

72. Fedoruk, M., Meixner, M., Carretero-palacios, S. & Lohmu, T. Nanolithography by Plasmonic Heating and Optical Manipulation of Gold Nanoparticles. *ACS Nano* **7,** 7648–7653 (2013).

73. Schmid, S., Wu, K., Larsen, P. E., Rindzevicius, T. & Boisen, A. Low-Power Photothermal Probing of Single Plasmonic Nanostructures with Nanomechanical String Resonators. *Nano Lett.* **14,** 2318–2321 (2014).

74. Herzog, J. B., Knight, M. W. & Natelson, D. Thermoplasmonics: Quantifying Plasmonic Heating in Single Nanowires. *Nano Lett.* **14,** 499–503 (2014).

75. Neal, D. P. O., Hirsch, L. R., Halas, N. J., Payne, J. D. & West, J. L. Photo-thermal tumor ablation in mice using near infrared-absorbing nanoparticles. *Cancer Lett.* **209,** 171–176 (2004).

76. Huang, X. & El-Sayed, M. a. Gold nanoparticles: Optical properties and implementations in cancer diagnosis and photothermal therapy. *J. Adv. Res.* **1,** 13–28 (2010).

77. Hollins, R. C. Materials for optical limiters. *Curr. Opin. Solid State Mater. Sci.* **4,** 189–196 (1999).

78. Calvete, M., Yang, G. Y. & Hanack, M. Porphyrins and phthalocyanines as materials for optical limiting. *Synth. Met.* **141,** 231–243 (2004).

79. Hongbing, Z., Wenzhe, C., Minquan, W. & Chunlin, Z. Optical limiting properties of peripherally modified palladium phthalocyanines doped silica gel glass. *Chem. Phys. Lett.* **389,** 119–123 (2004).

80. O'Flaherty, S. M. *et al.* Molecular Engineering of Peripherally And Axially Modified Phthalocyanines for Optical Limiting and Nonlinear Optics. *Adv. Mater.* **15,** 19–32 (2003).

81. Dini, D., Barthel, M. & Hanack, M. Phthalocyanines as Active Materials for Optical Limiting. *European J. Org. Chem.* **2001,** 3759–3769 (2001).

82. Riggs, J. E. & Sun, Y.-P. Optical Limiting Properties of [60]Fullerene and Methano[60]fullerene Derivative in Solution versus in Polymer Matrix: The Role of Bimolecular Processes and a Consistent Nonlinear Absorption Mechanism. *J. Phys. Chem. A* **103,** 485–495 (1999).

83. Aleali, H., Sarkhosh, L., Karimzadeh, R. & Mansour, N. Threshold-tunable optical limiteers of Au nanoparticles in castor oil. *J. Nonlinear Opt. Phys. Mater.* **21,** 1250024 (2012).

84. Nagaraja, K. K., Pramodini, S., Poornesh, P. & Nagaraja, H. S. Effect of annealing on the structural and nonlinear optical properties of ZnO thin films under cw regime. *J. Phys. D. Appl. Phys.* **46,** 055106 (2013).

85. Henari, F. Z. & Cassidy, S. Non-linear optical properties and all optical switching of Congo red in solution. *Opt. - Int. J. Light Electron Opt.* **123,** 711–714 (2012).

86. Majles Ara, M. H. *et al.* Optical characterization of Erioglaucine using z-scan technique, beam radius variations and diffraction pattern in far-field. *Curr. Appl. Phys.* **9,** 885–889 (2009).

87. Mansour, K., Soileau, M. J. & Stryland, E. W. Van. Nonlinear optical properties of carbon-black suspensions (ink). *J. Opt. Soc. Am. B* **9,** 1100 (1992).

88. Jain, P. K., Lee, K. S., El-Sayed, I. H. & El-Sayed, M. a. Calculated absorption and scattering properties of gold nanoparticles of different size, shape, and composition: applications in biological imaging and biomedicine. *J. Phys. Chem. B* **110,** 7238–48 (2006).

89. Shahriari, E. The effect of nanoparticle size on thermal diffusivity of gold nano-fluid measured using thermal lens technique. *J. Eur. Opt. Soc. rapid pubblication* **13026,** 1–4 (2013).

90. Mostafavi, M. *et al.* Optical Limitation induced by Gold Clusters . 1 . Size Effect. *J. Phys. Chem.* **104,** 6133–6137 (2000).

91. Evanoff, D. D. & Chumanov, G. Size-Controlled Synthesis of Nanoparticles. 2. Measurement of Extinction, Scattering, and Absorption Cross Sections. *J. Phys. Chem. B* **108,** 13957–13962 (2004).

92. Setoura, K., Werner, D. & Hashimoto, S. Optical Scattering Spectral Thermometry and Refractometry of a Single Gold Nanoparticle under CW Laser Excitation. *J. Phys. Chem. C* **116,** 15458–15466 (2012).

93. Olesiak-Banska, J., Gordel, M., Kolkowski, R., Matczyszyn, K. & Samoc, M. Third-Order Nonlinear Optical Properties of Colloidal Gold Nanorods. *J. Phys. Chem. C* **116,** 13731–13737 (2012).

94. Li, C., Qiu, C., Zhang, Y. & Li, D. Self-assembly of PEGylated gold nanorods and its optical limiting property. *Mater. Lett.* (2014). doi:10.1016/j.matlet.2014.11.012

95. Petrova, H. *et al.* On the temperature stability of gold nanorods: comparison between thermal and ultrafast laser-induced heating. *Phys. Chem. Chem. Phys.* **8,** 814–21 (2006).

96. Neupane, B., Zhao, L. & Wang, G. Up-conversion luminescence of gold nanospheres when excited at nonsurface plasmon resonance wavelength by a continuous wave laser. *Nano Lett.* **13,** 4087–92 (2013).

97. Richardson, H. H., Carlson, M. T., Tandler, P. J., Hernandez, P. & Govorov, A. O. Experimental and theoretical studies of light-to-heat conversion and collective heating effects in metal nanoparticle solutions. *Nano Lett.* **9,** 1139–46 (2009).

98. Dengler, S., Kübel, C., Schwenke, A., Ritt, G. & Eberle, B. Near- and off-resonant optical limiting properties of gold–silver alloy nanoparticles for intense nanosecond laser pulses. *J. Opt.* **14,** 075203 (2012).

99. Eslamifar, M. & Mansour, N. Optical Limiting Properties of Colloids Enhanced by Gold Nanoparticles Based on Thermal Nonlinear Refraction. *Int. J. Opt. Photonics* **6,** 49–56 (2012).

100. Nadjari, H., Hajiesmaeilbaigi, F. & Motamedi, a. Thermo optical response and optical limiting in Ag and Au nanocolloid prepared by laser ablation. *Laser Phys.* **20,** 859–864 (2010).

101. Dawson, J. *Optical limiting materials based on gold nanoparticles*. 1–12 (2014).

102. Nordwall, B. D. Laser advance spur Pentagon efforts to protect flight Crewmembers' Eyes. *Aviat. Week Sp. Technol.* 73 (1988).

103. Zhou, J., Ralston, J., Sedev, R. & Beattie, D. a. Functionalized gold nanoparticles: synthesis, structure and colloid stability. *J. Colloid Interface Sci.* **331,** 251–62 (2009).

104. Cao, G. *Nanostructures and nanomaterials: synthesis, properties and applications*. (2004). at <http://www.worldscientific.com/doi/pdf/10.1142/9781860945960_fmatter>

105. Jana, N. R., Gearheart, L. & Murphy, C. J. Seed-Mediated Growth Approach for Shape-Controlled Synthesis of Spheroidal and Rod-like Gold Nanoparticles Using a Surfactant Template. *Adv. Mater.* **13,** 1389–1393 (2001).

106. Nikoobakht, B. & El-sayed, M. A. Preparation and Growth Mechanism of Gold Nanorods (NRs) Using Seed-Mediated Growth Method. *Chem. Mater.* **15,** 1957–1962 (2003).

107. Israelachvili, J. *Intermolecular and Surface Forces*. (Elsevier, 2004). at <https://www.elsevier.com/books/intermolecular-and-surface-forces/israelachvili/978-0-12-391927-4>

108. Israelachvili, J. *Intermolecular and Surface Forces*. (1992).

109. Turkevich, J., Stevenson, P. C. & Hillier, J. A study of the nucleation and growth processes in the synthesis of colloidal gold. *Discuss. Faraday Soc.* **11,** 55–75 (1951).

110. Weber, V. PLASMONIC NANOSTRUCTURES FOR THE REALIZATION OF SENSORS BASED ON SURFACE ENHANCED RAMAN SPECTROSCOPY. (2013).

111. Amendola, V. & Meneghetti, M. Size Evaluation of Gold Nanoparticles by UV - vis Spectroscopy. *J. Phys. Chem.* **113,** 4277–4285 (2009).

112. Goris, B. *et al.* Atomic-scale determination of surface facets in gold nanorods. *Nat. Mater.* **11,** 930–5 (2012).

113. Perezjuste, J., Pastorizasantos, I., Lizmarzan, L. & Mulvaney, P. Gold nanorods: Synthesis, characterization and applications. *Coord. Chem. Rev.* **249,** 1870–1901 (2005).

114. Gans, R. On the shape of ultramicroscopic gold particles. *Ann. Phys.* **37,** 881–900 (1972).

115. Yu, Y.-Y., Chang, S.-S., Lee, C.-L. & Wang, C. R. C. Gold Nanorods: Electrochemical Synthesis and Optical Properties. *J. Phys. Chem. B* **101,** 6661–6664 (1997).

116. Placido, T. *et al.* Photochemical Synthesis of Water-Soluble Gold Nanorods: The Role of Silver in Assisting Anisotropic Growth. *Chem. Mater.* **21,** 4192–4202 (2009).

117. Pham, T., Jackson, J. B., Halas, N. J. & Lee, T. R. Preparation and Characterization of Gold Nanoshells Coated with Self-Assembled Monolayers. *Langmuir* **18,** 4915–4920 (2002).

118. Oldenburg, S. ., Averitt, R. ., Westcott, S. . & Halas, N. . Nanoengineering of optical resonances. *Chem. Phys. Lett.* **288,** 243–247 (1998).

119. Stöber, W., Fink, A. & Bohn, E. Controlled growth of monodisperse silica spheres in the micron size range. *J. Colloid Interface Sci.* **26,** 62–69 (1968).

120. Brinson, B. E. *et al.* Nanoshells Made Easy : Improving Au Layer Growth on Nanoparticle Surfaces. **120,** 14166–14171 (2008).

121. Sastry, M. Phase transfer protocols in nanoparticle synthesis. *Curr. Sci.* **85,** 1735–1745 (2003).

122. McMahon, J. M. & Emory, S. R. Phase transfer of large gold nanoparticles to organic solvents with increased stability. *Langmuir* **23,** 1414–8 (2007).

123. Hostetler, M. J., Templeton, A. C. & Murray, R. W. Dynamics of Place-Exchange Reactions on Monolayer-Protected Gold Cluster Molecules. *Langmuir* **15,** 3782–3789 (1999).

124. Della Gaspera, E. *et al.* CO optical sensing properties of nanocrystalline ZnO–Au films: Effect of doping with transition metal ions. *Sensors Actuators B Chem.* **161,** 675–683 (2012).

125. Dresselhaus, M. S., Dresselhaus, G. & Eklund, P. C. Raman Scattering in Fullerenes. *J. Raman Spectrosc.* **27,** 351–371 (1996).

126. Geng, M. *et al.* Functionalization of C60 with gold nanoparticles. *Carbon N. Y.* **48,** 3570–3574 (2010).

127. Walker, C. H., John, J. V. S. & Wisian-Neilson, P. Synthesis and Size Control of Gold Nanoparticles Stabilized by Poly (methylphenylphosphazene). *Am. Chem. Soc.* **123,** 3846–3847 (2001).

128. Wisian-Neilson, P. & Garcìa-Alonso, F. J. Coordination of Poly(methylpheny1phosphazene) and Poly(dimethylphosphazene). *Macromolecules* **26,** 7156–7160 (1993).

129. Delgado, J. L., Oswald, F., Cardinali, F., Langa, F. & Martìn, N. On the Thermal Stability of [60] Fullerene Cycloadducts : Retro-Cycloaddition Reaction of 2-Pyrazolino [4,5:1,2][60] fullerenes. *J. Org. Chem.* **73,** 3184–3188 (2008).

130. Martín, N. *et al.* Retro-Cycloaddition Reaction of Pyrrolidinofullerenes. *Angew. Chemie* **118,** 116–120 (2006).

131. Sudeep, P. K. *et al.* Fullerene-Functionalized Gold Nanoparticles. A Self-Assembled Photoactive Antenna-Metal Nanocore Assembly. *Nano Lett.* **2,** 29–35 (2002).

132. Hasell, T. *et al.* Silver Nanoparticle Impregnated Polycarbonate Substrates for Surface Enhanced Raman Spectroscopy. *Adv. Funct. Mater.* **18,** 1265–1271 (2008).

133. He, T., Wang, C., Pan, X. & Wang, Y. Nonlinear optical response of Au and Ag nanoparticles doped polyvinylpyrrolidone thin films. *Phys. Lett. A* **373,** 592–595 (2009).

134. Mathews, S. J., Kumar, S. C., Giribabu, L. & Rao, S. V. Nonlinear optical and optical limiting properties of phthalocyanines in solution and thin films of PMMA at 633 nm studied using a cw laser. *Mater. Lett.* **61,** 4426–4431 (2007).

135. Alexandrov, A. *et al.* UV-initiated growth of gold nanoparticles in PMMA matrix. *Appl. Surf. Sci.* **248,** 181–184 (2005).

136. Jia, T., He, T., Li, P., Mo, Y. & Cui, Y. A study of the thermal-induced nonlinearity of Au and Ag colloids prepared by the chemical reaction method. *Opt. Laser Technol.* **40,** 936–940 (2008).

137. Cited, R. & Alon, U. GOGGLES‘ LENSES. (1992).

138. Glass, L. & Ski, F. O. R. LOOKING GLASS FOR SKI GOGGLES. **1,** (2001).

139. He, J. & Kunitake, T. Preparation and Thermal Stability of Gold Nanoparticles in Silk-Templated Porous Filaments of Titania and. *Chem. Mater.* **10,** 2656–2661 (2004).

140. Huang, X., Jain, P. K., El-Sayed, I. H. & El-Sayed, M. a. Determination of the minimum temperature required for selective photothermal destruction of cancer cells with the use of immunotargeted gold nanoparticles. *Photochem. Photobiol.* **82,** 412–7 (2006).

141. Zhou, Y. *et al.* Preparation of a novel core–shell nanostructured gold colloid–silk fibroin bioconjugate by the protein. *Chem. Commun.* 2518–2519 (2001). doi:10.1039/b108013j

142. Gogurla, N. *et al.* Transparent and flexible resistive switching memory devices with a very high ON/OFF ratio using gold nanoparticles embedded in a silk protein matrix. *Nanotechnology* **24,** 345202 (2013).

143. Cohen-karni, T. *et al.* Nanocomposite Gold-Silk Nano fi bers. *Nano Lett.* **12,** 10–13 (2012).

144. Kojic, N. *et al.* Focal Infection Treatment using Laser-Mediated Heating of Injectable Silk Hydrogels with Gold Nanoparticles. *Adv. Funct. Mater.* **22,** 3793–3798 (2012).

145. Raether, H. *Surface Plasmons on Smooth and Rough Surfaces and on Gratings*. **111,** (Springer Berlin Heidelberg, 1988).

146. Smith, T. & Guild, J. The C.I.E. colorimetric standards and their use. *Trans. Opt. Soc.* **33,** 73–134 (1931).

147. Hwang, S.-W. *et al.* Materials for bioresorbable radio frequency electronics. *Adv. Mater.* **25,** 3526–31 (2013).

148. Altman, G. H. *et al.* Silk-based biomaterials. *Biomaterials* **24,** 401–416 (2003).

149. Sagnella, A. *et al.* Bio-doping of regenerated silk fibroin solution and films: a green route for biomanufacturing. *RSC Adv.* **4,** 33687 (2014).

150. Tretinnikov, O. N. & Tamada, Y. Influence of Casting Temperature on the Near-Surface Structure and Wettability of Cast Silk Fibroin Films. *Langmuir* **17,** 7406–7413 (2001).

151. Sheik-Bahae, M., Said, A. A., Wei, T.-H., Hagan, D. J. & Van Stryland, E. W. Sensitive measurement of optical nonlinearities using a single beam. *IEEE J. Quantum Electron.* **26,** 760–769 (1990).

152. Guo, S. *et al.* Second Z-scan in materials with nonlinear refraction and nonlinear absorption. *J. Opt. A Pure Appl. Opt.* **4,** 504–508 (2002).

153. Chapple, P. B., Staromlynska, J., Hermann, J. A., Mckay, T. J. & Mcduff, R. G. Single-Beam Z-Scan: Measurement Techniques and Analysis. *J. Nonlinear Opt. Phys. Mater.* **6,** 251–293 (1997).

154. Hermann, J. A. & Wilson, P. J. FACTORS AFFECTING OPTICAL LIMITING AND SCANNING WITH THIN NONLINEAR SAMPLES. *J. Nonlinear Opt. Phys. Mater.* **2,** 613–629 (1993).

155. Tian, J. G., Zhang, C., Zhang, G. & Li, J. Position dispersion and optical limiting resulting from thermally induced nonlinearities in Chinese tea liquid. *Appl. Opt.* **32,** 6628–32 (1993).

156. Ryasnyanskiy, I., Palpant, B., Debrus, S., Pal, U. & Stepanov, A. Third-order nonlinear-optical parameters of gold nanoparticles in different matrices. *J. Lumin.* **127,** 181–185 (2007).

157. Souza, R. F., Alencar, M. a. R. C., da Silva, E. C., Meneghetti, M. R. & Hickmann, J. M. Nonlinear optical properties of Au nanoparticles colloidal system: Local and nonlocal responses. *Appl. Phys. Lett.* **92,** 201902 (2008).

158. Ganeev, R. a., Baba, M., Ryasnyansky, a. I., Suzuki, M. & Kuroda, H. Characterization of optical and nonlinear optical properties of silver nanoparticles prepared by laser ablation in various liquids. *Opt. Commun.* **240,** 437–448 (2004).

159. Seo, J. T. *et al.* Optical nonlinearities of Au nanoparticles and Au/Ag coreshells. *Opt. Lett.* **34,** 307 (2009).

160. Elim, H. I., Yang, J., Lee, J.-Y., Mi, J. & Ji, W. Observation of saturable and reverse-saturable absorption at longitudinal surface plasmon resonance in gold nanorods. *Appl. Phys. Lett.* **88,** 083107 (2006).

161. Sindhu Sukumaran, V. & Ramalingam, a. Spectral and nonlinear studies of night blue dye. *Phys. Lett. A* **359,** 467–470 (2006).

162. Kumar, G. S., Milka, B. V., Muneera, C. I., Sathiyamoorthy, K. & Vijayan, C. Nonlinear refraction and optical limiting in solid films of amido black dye under CW laser illumination. *Opt. Mater. (Amst).* **30,** 311–313 (2007).

163. Rekha and A . Optical Nonlinear Proreties and Optical Limiting Effect of Metanil Yellow. *Sci. Appl. Publ. Sci.* **2,** 285–291 (2009).

164. American National Standard for Safe Use of Lasers ANSI Z136.1– 2000. www.laserinstitute.org.

165. Sathiyamoorthy, K., Vijayan, C. & Kothiyal, M. P. Low power optical limiting in ClAl-Phthalocyanine due to self defocusing and self phase modulation effects. *Opt. Mater. (Amst).* **31,** 79–86 (2008).

166. Cuppo, F. L. S., Neto, A. M. F., Gomez, S. L. & Palffy-Muhoray, P. Thermal-lens model compared with the Sheik-Bahae formalism in interpreting Z-scan experiments on lyotropic liquid crystals. *J. Opt. Soc. Am. B* **19,** 1342–1348 (2002).

167. Parker, J. G. Optical absorption in glass: investigation using an acoustic technique. *Appl. Opt.* **12,** 2974–7 (1973).

168. Rosencwaig, A. Theory of the photoacoustic effect with solids. *J. Appl. Phys.* **47,** 64 (1976).

169. Cuppo, F. L. S. & Neto, A. M. F. Laurate / Water Solutions at Amphiphilic Concentrations around the Critical Micellar Concentration : A Laser Gaussian Single Beam Experiment in Millisecond. *Langmuir* **18,** 9647–9653 (2002).

170. Pramodini, S., Poornesh, P. & Nagaraja, K. K. Thermally induced nonlinear optical response and optical power limiting of acid blue 40 dye. *Curr. Appl. Phys.* **13,** 1175–1182 (2013).

171. Deng, L., He, K., Zhou, T. & Li, C. Formation and evolution of far-field diffraction patterns of divergent and convergent Gaussian beams passing through self-focusing and self-defocusing media. *J. Opt. A Pure Appl. Opt.* **7,** 409–415 (2005).

172. Yu, B., Gu, Y. & Mao, Y. Nonlinear optical properties of PbS nanoparticles under CW laser illumination. *J. Nonlinear Opt. Phys. Mater.* **9,** 117–125 (2000).

173. Chen, H. & Diebold, G. Chemical Generation of Acoustic Waves: A Giant Photoacoustic Effect. *Science (80-.).* **270,** 963–966 (1995).

174. González, M. G., Liu, X., Niessner, R. & Haisch, C. Lead ion detection in turbid media by pulsed photoacoustic spectrometry based on dissolution of gold nanoparticles. *Sensors Actuators B Chem.* **150,** 770–773 (2010).

175. Feis, A., Gellini, C., Remigio, P. & Becucci, M. Photoacoustics Photoacoustic excitation profiles of gold nanoparticles. *Photoacoustics* **2,** 47–53 (2014).

176. Cho, E. C. *et al.* Measuring the Optical Absorption Cross Sections of Au - Ag Nanocages and Au Nanorods by Photoacoustic Imaging. *J. Phys. Chem. C* **113,** 9023–9028 (2009).

177. Alabastri, A. *et al.* Molding of Plasmonic Resonances in Metallic Nanostructures: Dependence of the Non-Linear Electric Permittivity on System Size and Temperature. *Materials (Basel).* **6,** 4879–4910 (2013).

178. Alabastri, A., De Angelis, F. & Proietti Zaccaria, R. Heating processes in plasmonic resonances: a non-linear temperature dependent permittivity model. in *SPIE Nanosci. + Eng.* (Cabrini, S., Lérondel, G., Schwartzberg, A. M. & Mokari, T.) 91610U (International Society for Optics and Photonics, 2014). doi:10.1117/12.2066155

179. Torquato, S., Lu, B. & Rubinstein, J. Nearest-Neighbor distribution function in many-body systems. *Phys. Rev. A* **41,** 2059–2075 (1990).

180. Evans, J. Simple forms for equations of rays in gradient-index lenses. *Am. J. Phys.* **58,** 773–778 (1990).

181. Santamato, E. & Shen, Y. R. Field-curvature effect on the diffraction ring pattern of a laser beam dressed by spatial self-phase modulation in a nematic film. *Opt. Lett.* **9,** 564–566 (1984).

182. Ramirez, E. V. G., Carrasco, M. L. A., Otero, M. M. M., Cerda, S. C. & Castillo, M. D. I. Far field intensity distributions due to spatial self phase modulation of a Gaussian beam by a thin nonlocal nonlinear media. *Opt. Express* **18,** 22067–79 (2010).

183. Qin, Z. & Bischof, J. C. Thermophysical and biological responses of gold nanoparticle laser heating. *Chem. Soc. Rev.* **41,** 1191 (2012).

184. Wang, J., Hernandez, Y., Lotya, M., Coleman, J. N. & Blau, W. J. Broadband Nonlinear Optical Response of Graphene Dispersions. *Adv. Mater.* **21,** 2430–2435 (2009).

185. Meneghetti, M. *et al.* Optical limiting of multilayer sol-gel structures containing fidlerenes. *Synth. Met.* **103,** 2474–2475 (1999).

186. Zhang, P. *et al.* The self-assembly of gold nanoparticles with C60 nanospheres: fabrication and optical liming effect. *Chem. Phys. Lett.* **382,** 599–604 (2003).

187. Palpant, B., Rashidi-Huyeh, M., Gallas, B., Chenot, S. & Fisson, S. Highly dispersive thermo-optical properties of gold nanoparticles. *Appl. Phys. Lett.* **90,** 223105 (2007).

188. Hanninen, P. E., Soini, E. & Hell, W. Continuous wave excitation two-photon fluorescence microscopy. *J. Microsc.* **176,** 222–225 (1994).

189. Liu, Y., Sonek, G. J., Berns, M. W., Konig, K. & Tromberg, B. J. Two-photon fluorescence excitation in continuous-wave infrared optical tweezers. *Opt. Lett.* **20,** 2246 (1995).

190. Xu, C. & Webb, W. W. Measurement of two-photon excitation cross sections of molecular fluorophores with data from 690 to 1050 nm. *J. Opt. Soc. Am. B* **13,** 481 (1996).

191. Niu, B., Pardy, P., Fortier, J., Ortega, M. & Eiles, T. Two-photon absorption laser assisted device alteration using continuous wave 1,340 nm laser. *J. Mater. Sci. Mater. Electron.* **22,** 1542–1552 (2011).

192. Doremus, R. H. Optical Properties of Small Gold Particles. *J. Chem. Phys.* **40,** 2389 (1964).

193. Ros, I., Schiavuta, P., Bello, V., Mattei, G. & Bozio, R. Femtosecond nonlinear absorption of gold nanoshells at surface plasmon resonance. *Phys. Chem. Chem. Phys.* **12,** 13692–8 (2010).

194. Tang, B., Sun, L., Kaur, J., Yu, Y. & Wang, X. In-situ synthesis of gold nanoparticles for multifunctionalization of silk fabrics. *Dye. Pigment.* **103,** 183–190 (2014).

195. Cohen-Karni, T. *et al.* Nanocomposite gold-silk nanofibers. *Nano Lett.* **12,** 5403–6 (2012).

196. Xia, Y. Fabrication and properties of conductive conjugated polymers/silk fibroin composite fibers. *Compos. Sci. Technol.* **68,** 1471–1479 (2008).

197. Frez, C. & Diebold, G. J. Laser generation of gas bubbles: Photoacoustic and photothermal effects recorded in transient grating experiments. *J. Chem. Phys.* **129,** 184506 (2008).

198. Nascimento, C. M. *et al.* Experimental demonstration of novel effects on the far-field diffraction patterns of a Gaussian beam in a Kerr medium. *J. Opt. A Pure Appl. Opt.* **8,** 947 (2006).

199. Wang, X. & Mujumdar, A. S. Heat transfer characteristics of nanofluids : a review. *Int. J. Therm. Sci.* **46,** 1–19 (2007).

200. Pitsillides, C. M., Joe, E. K., Wei, X., Anderson, R. R. & Lin, C. P. Selective cell targeting with light-absorbing microparticles and nanoparticles. *Biophys. J.* **84,** 4023–32 (2003).

201. Ribeiro, L. S. *et al.* Silica nanoparticles functionalized with a thermochromic dye for textile applications. *J. Mater. Sci.* **48,** 5085–5092 (2013).

202. Saeli, M., Piccirillo, C., Warwick, M. E. A. & Binions, R. Thermochromic Thin Films : Synthesis , Properties and Energy Consumption Modelling. 736–746 (2013).

203. Kamalisarvestani, M., Saidur, R., Mekhilef, S. & Javadi, F. S. Performance , materials and coating technologies of thermochromic thin fi lms on smart windows. *Renew. Sustain. Energy Rev.* **26,** 353–364 (2013).

204. Rodrigues Ribeiro, R. S. *et al.* Rapid fabrication of polymeric micro lenses for optical fiber trapping and beam shaping. in *SPIE Nanosci. + Eng.* (Dholakia, K. & Spalding, G. C.) 91642M (International Society for Optics and Photonics, 2014). doi:10.1117/12.2060374

205. Chang, C.-Y., Yang, S.-Y. & Chu, M.-H. Rapid fabrication of ultraviolet-cured polymer microlens arrays by soft roller stamping process. *Microelectron. Eng.* **84,** 355–361 (2007).

206. Wen, T.-T. & Hocheng, H. Innovative rapid replication of microlens arrays using electromagnetic force-assisted UV imprinting. *J. Micromechanics Microengineering* **19,** 025012 (2009).

207. Guo, R., Yuan, D. & Das, S. Large-area microlens arrays fabricated on flexible polycarbonate sheets via single-step laser interference ablation. *J. Micromechanics Microengineering* **21,** 015010 (2011).

208. Meunier, T., Villafranca, A. B., Bhardwaj, R. & Weck, A. Fabrication of microlens arrays in polycarbonate with nanojoule energy femtosecond laser pulses. *Opt. Lett.* **37,** 4266–8 (2012).

209. Xie, D., Zhang, H., Shu, X. & Xiao, J. Fabrication of polymer micro-lens array with pneumatically diaphragm-driven drop-on-demand inkjet technology. *Opt. Express* **20,** 15186–95 (2012).

210. Pavia, J. M., Wolf, M. & Charbon, E. Measurement and modeling of microlenses fabricated on single-photon avalanche diode arrays for fill factor recovery. *Opt. Express* **22,** 4202–13 (2014).

211. Suzuki, M., Uchida, T. & Matsuura, K. Microlens array sheet for a liquid crystal display, method for attaching the same and liquid crystal display equipped with the same. (1995). at <http://www.google.com/patents/EP0640850A2?cl=en>

212. Segawa, M., Sugiyama, M. & Nakatani, Y. Microlens array sheet and method of producing the same. (2011). at <http://www.google.co.in/patents/US7864450>

213. Peterson, C. & Koch, G. Polarized light emitting devices and methods. (2005). at <https://www.google.com/patents/US20050035361>

SCIENTIFIC CONTRIBUTIONS

Papers

1. Frare, M. C., Signorini, R., Weber, V. & Bozio, R. Gold nanoparticles as optical limiting materials against cw lasers. in *SPIE* (Zamboni, R., Kajzar, F., Szep, A. A., Burgess, D. & Owen, G.) **8901,** 890113 (2013).

2. Frare, M. C., Weber, V., Signorini, R. & Bozio, R. Gold nanoparticles in a polycarbonate matrix for optical limiting against a CW laser. *Laser Phys.* **24,** 1–11 (2014).

3. Frare, M. C., Weber, V., De Filippo, C. C., Signorini, R., Maggini, M. & Bozio, R., Improving optical limiting of cw lasers with fullerene functionalized gold nanoparticles. *SPIE Org. Photonics + Electron.* **9181,** 918116 (2014).

4. Frare, M. C., Weber, V., De Filippo, C. C., Signorini, R., Maggini, M. & Bozio, R., Fullerene functionalized gold nanoparticles for optical limiting of continuous wave laser. *PCCP* Submitted (2014).

Conferences

1. II Congresso nazionale di spettroscopie Raman ed effetti ottici non lineari
6-8 June 2012, CNR - Area della Ricerca di Bologna, Italy
Poster presentation titled: "*Optical limiting properties of Au nanoparticles in polycarbonate*"

2. SPIE Security & Defence
23 - 26 September 2013, Internationals Congress Center, Dresden, Germany
Oral presentation titled: "*Gold nanoparticles as optical limiting materials against CW lasers*"

3. SPIE Optics & Photonics
17-21 August 2014, Convention Center, San Diego, California, United States
Poster presentation titled: "*Improving optical limiting of cw lasers with fullerene functionalized gold nanoparticles*"

RINGRAZIAMENTI

Vorrei ringraziare il mio supervisore, il prof. Bozio, per avermi sempre appoggiato e incoraggiato nella ricerca e per tutto il tempo e la pazienza che mi ha dedicato in questi tre anni.

Ringrazio tutti i miei colleghi e amici che hanno condiviso con me questi anni di studio, esperimenti e discussioni scientifiche, ma soprattutto di risate, pranzi, pause caffè e aperitivi: Vere coinquilina e collega, ma prima di tutto amica, così come Nicola che vuole sempre avere ragione, Ilaria che senza di lei il laboratorio crolla, Luca e i pranzi in Forcellini, Alessia ormai donna in carriera, Vale per il suo carattere travolgente, Alessandro e la sua memoria, Lucio e la sua precisione, insieme ai più nuovi Andrea che è troppo bravo, Elena sempre sorridente ed Anna con la sua infinita gentilezza.

Ringrazio anche Raffaella che mi ha dato la possibilità di iniziare questo percorso in questo gruppo e Simone per la sua disponibilità ed i suoi consigli.

Ringrazio anche i colleghi del Lafsi per il supporto morale e per avermi sempre fatto sentire parte del gruppo. E grazie a Greshia, coinquilina e amica, per tutto l'affetto e le attenzioni che ha il potere di dare a tutti intorno a lei.

Vorrei ringraziare tanto i miei compagni di pallavolo, che mi hanno regalato lo svago dopo il lavoro ma anche grandi e profonde amicizie.

Voglio ringraziare tutti coloro che mi hanno spinto a fare il dottorato, ma anche coloro che mi avevano consigliato di non farlo, perché c'è sempre bisogno di chi ti dice che non devi fare qualcosa per spingerti a fare il contrario.

Ringrazio Davide per avermi appoggiato quando non volevo fare il dottorato e anche quando invece ho deciso di farlo, per avermi sempre ascoltato e consigliato, per la forza che mi dà nell'affrontare le nuove sfide e perché forse in fondo non è tutto bianco o nero.

Voglio ringraziare infinitamente la mia famiglia, per avermi insegnato che nella vita si può superare qualunque difficoltà e che è tutto più semplice con gli affetti accanto. La mia meravigliosa sorella per il coraggioso appoggio che mi dà sempre, perché non saprei fare nulla senza di lei e tutto quello che facciamo insieme viene sempre meglio, e perché la volontà di darle il buon esempio mi rende una persona migliore. Mia mamma e mio papà, per

il loro grande amore e il profondo sostengono in tutte le mie scelte, perché mi hanno permesso di raggiungere importanti risultati. E tutti i miei nonni, per avermi dato un grande esempio con le loro vite e per essere sempre stati fieri di me.